Summer 2012

Towards 4D MVCBCT for lung tumor treatment

Mingqing Chen
University of Iowa

TOWARDS 4D MVCBCT FOR LUNG TUMOR TREATMENT

by

Mingqing Chen

An Abstract

Of a thesis submitted in partial fulfillment
of the requirements for the Doctor of
Philosophy degree in Electrical and Computer Engineering
in the Graduate College of
The University of Iowa

July 2012

Thesis Supervisor: Assistant Professor R. Alfredo. C. Siochi

ABSTRACT

Currently in our clinic, a mega-voltage cone beam computed tomography (MVCBCT) scan is performed before each treatment for patient localization. For non-small cell lung cancer (NSCLC) patients, a strain gauge is used as an external surrogate to indicate tumor motion in both the planning stage and the treatment stage. However, it is likely that the amplitude of tumor motion varies between treatment fractions without a corresponding change in the surrogate signal. Motion amplitude larger than what was planned may underdose the tumor and overexpose normal tissues.

The overall objective of this project is to extend the capabilities of MVCBCT for respiratory motion management by taking advantage of 2D projection images. First, a new method was developed to detect ipsi-lateral hemi-diaphragm apex (IHDA) motion along superior-inferior (SI) direction in 3D. Then a respiratory correlated reconstruction method was implemented and verified. This method is able to create MVCBCT volume in the full exhale (FE) and the full inhale (FI) phases, respectively. The diaphragm to tumor motion ratio (DTMR) was derived by quantifying the absolute position of the tumor and IHDA in these two volumes. The DTMR and the extracted IHDA motion were further used to calibrate the strain gauge signal.

Second, an organ motion detection approach was developed, in which the detection is converted into an optimal interrelated surface detection problem. The framework was first applied to tumor motion extraction, which enables accurate detection for large tumors (with a diameter not smaller than 1.9cm). The framework was then applied to lung motion extraction and the extracted lung motion model was used to create a series of displacement vector fields for a motion compensated (MC) reconstruction. The accuracy of both tumor extraction and the MC approach was validated, which shows their clinical feasibility.

Last but not least, a novel enhancement framework was developed. The aim of this approach is to eliminate the overlapping tissues and organs in the CBCT projection images. Though scattering and noise is the major problem, the proposed method is able to achieve enhanced projection images with a higher contrast to noise ratio (CNR) without compromising detection accuracy on tumors and IHDA.

Abstract Approved: _____
Thesis Supervisor

_____
Title and Department

_____
Date

TOWARDS 4D MVCBCT FOR LUNG TUMOR TREATMENT

by

Mingqing Chen

A thesis submitted in partial fulfillment
of the requirements for the Doctor of
Philosophy degree in Electrical and Computer Engineering
in the Graduate College of
The University of Iowa

July 2012

Thesis Supervisor: Assistant Professor R. Alfredo C. Siochi

Graduate College
The University of Iowa
Iowa City, Iowa

CERTIFICATE OF APPROVAL

PH.D. THESIS

This is to certify that the Ph.D. thesis of

Mingqing Chen

has been approved by the Examining Committee
for the thesis requirement for the Doctor of Philosophy
degree in Electrical and Computer Engineering at the July 2012 graduation.

Thesis Committee: R. Alfredo C. Siochi, Thesis Supervisor

Milan Sonka

Joseph M. Reinhardt

Xiaodong Wu

Reinhard R. Beichel

ACKNOWLEDGMENTS

First of all, I would like to thank my advisor, Dr. Alfredo Siochi, for all the patience, guidance, encouragement, and support throughout the last five years. His profound knowledge, great insight and excellent mentorship have had remarkable influence on my study, and will continue inspiring me in my future career. I can still remember the enthusiastic welcome he gave me the first time we met at the department's reception desk. During the five years, there has been countless times he stayed very late after his clinical duty to discuss the project with me or to help me modify the paper to be submitted. Every time I feel like I've lost of the direction of my research, he always reminds me of the "big picture" and makes me feel the significance of my work. In all, I feel honored to have the opportunity working under his instruction.

I would also like to express my gratitude to Dr. Yefeng Zheng, my manager in Siemens Corporate Research during my internship. He inspired me by sharing many innovative ideas for this thesis, including 2D-to-3D shape recovery from projection images and the background subtraction technique. We cooperated consistently during the last two years of my Ph.D. study, after we got to know each other. He was not only a mentor but a friend.

I would also like to recognize Dr. Qi Song, for many valuable discussions about the graph search framework and other various topics related to image processing. We also cooperated on several projects. I would also like to express my appreciation Dr. Kunlin Cao, for her help and colabration in the image registration method to derive prior motion models. I would also like to acknowledge the support and the help I received from my fellow lab mates and friends, including Shanhui Sun, Dr. Yunfei Huang, Dr. Kai Ding, Junjie Bai, Dr. Xin Dou, Yunlong Liu and Dr. Ziyue Xu.

In addition, I would like to thank those faculty members: Dr. Milan Sonka, Dr. Xiaodong Wu, Dr. Joseph Reinhardt, Dr. Reinhard Beichel, Dr. John Bayouth and Dr. Erwei Bai, in particular my committee members. During my Ph.D. study I have been to those professors' classes. The knowledge I gained through both their classes and the course projects were invaluable in completing my research.

Last but not least, I would like to take this opportunity to thank my parents for their enduring love and continuing support during all these years.

ABSTRACT

Currently in our clinic, a mega-voltage cone beam computed tomography (MVCBCT) scan is performed before each treatment for patient localization. For non-small cell lung cancer (NSCLC) patients, a strain gauge is used as an external surrogate to indicate tumor motion in both the planning stage and the treatment stage. However, it is likely that the amplitude of tumor motion varies between treatment fractions without a corresponding change in the surrogate signal. Motion amplitude larger than what was planned may underdose the tumor and overexpose normal tissues.

The overall objective of this project is to extend the capabilities of MVCBCT for respiratory motion management by taking advantage of 2D projection images. First, a new method was developed to detect ipsi-lateral hemi-diaphragm apex (IHDA) motion along superior-inferior (SI) direction in 3D. Then a respiratory correlated reconstruction method was implemented and verified. This method is able to create MVCBCT volume in the full exhale (FE) and the full inhale (FI) phases, respectively. The diaphragm to tumor motion ratio (DTMR) was derived by quantifying the absolute position of the tumor and IHDA in these two volumes. The DTMR and the extracted IHDA motion were further used to calibrate the strain gauge signal.

Second, an organ motion detection approach was developed, in which the detection is converted into an optimal interrelated surface detection problem. The framework was first applied to tumor motion extraction, which enables accurate detection for large tumors (with a diameter not smaller than 1.9cm). The framework was then applied to lung motion extraction and the extracted lung motion model was used to create a series of displacement vector fields for a motion compensated (MC) reconstruction. The accuracy of both tumor extraction and the MC approach was validated, which shows their clinical feasibility.

Last but not least, a novel enhancement framework was developed. The aim of this approach is to eliminate the overlapping tissues and organs in the CBCT projection images. Though scattering and noise is the major problem, the proposed method is able to achieve enhanced projection images with a higher contrast to noise ratio (CNR) without compromising detection accuracy on tumors and IHDA.

TABLE OF CONTENTS

LIST OF TABLES

LIST OF FIGURES

CHAPTER 1

BACKGROUND AND MOTIVATION

1.1 Project introduction

Radiation therapy to the lung tumor has been a primary treatment option for lung cancer for four decades, often in conjunction with chemotherapy when a patient is medically unfit for surgery or when the tumor is inoperable (Vora et al., 2000). Generally, the development of radiotherapy aims to improve the accuracy and effect to the targeted tumor cells while reducing the radiation to the surrounding healthy tissues, since radiation may damage DNA of both healthy and malignant cells. Respiratory motion is one of the major challenges that may degrade the effectiveness of modern conformal radiation therapy (CRT) or intensity modulated radiation therapy (IMRT).

Overall, the purpose of my Ph.D. work is to explore and validate several novel methods that use mega-voltage cone beam CT (MVCBCT) projection images to make lung cancer radiotherapy more reliable. The MVCBCT is a daily localization device that takes advantage of the treatment beam and an electronic portal imaging device (EPID) (Section 1.3 provides the details). In the current clinical procedure, it creates a 3D volumetric image which is reconstructed from a series of 2D rotational projection images. This 3D volume is used to align with the treatment plan and localize the patient on the treatment table. However, when the MVCBCT is used for imaging non-small cell lung cancer (NSCLC) patient, this 3D volume alone does not provide information related to intra-fractional motion, e.g. respiratory motion. On the other hand, the projection images of MVCBCT provide high temporal resolution where one could observe the respiratory motion through the 2D image sequence (Figure 1-1). Based on this characteristic, several novel methods are developed, including:

(1) Detect the motion amplitude of the ipsi-lateral hemi-diaphragm apex (IHDA) in projection images, which is used as an internal surrogate to tumor motion amplitude;

(2) (3D+t) tumor motion model extraction from MVCBCT projection images;

(3) Respiratory correlated (RC) reconstruction;

(4) Motion compensated (MC) reconstruction by using a prior motion model of the lung;

(5) An enhancement framework that aims to remove the overlapping confounding tissues and organs in the MVCBCT projection images.

The motivations of each method are introduced as follows. First, the aim of IHDA detection is to calibrate the strain gauge signal during treatment delivery. Currently in our clinic, the strain gauge is used as an external surrogate to tumor motion during both treatment planning and the delivery. There are two major sources of inaccuracies of using the strain gauge: phase difference and inter-fractional variation of tumor motion. This variation could bring additional toxicity to surrounding tissues and reduce the actual dose the tumor may receive. On the other hand, the internal anatomical structures, such as the diaphragm or the trachea, have better correlation and less phase difference with the tumor, especially for tumors in the lower lobe. The use of the internal surrogate could not only provide phase information, but also provide absolute position. Moreover, the diaphragm has better contrast than the trachea in the 2D projection images, which makes it very suitable to be used as an internal surrogate. In chapter 2, the framework of IHDA detection in projection images is presented. The IHDA motion amplitude along the 3D superior-inferior (SI) direction is computed, which provides a respiratory signal with absolute positioning. This signal is further used as initial input for other approaches, including (3D+t) motion extraction, RC reconstruction, MC reconstruction and background subtraction.

Second, a novel approach of extracting (3D+t) tumor motion model is developed and introduced in Chapter 3. Generally, accurate organ segmentation in 2D projection images is limited by the low contrast and overlapping confounding tissues. To mitigate the influence of those confounding boundaries to the segmentation, the segmented 3D tumor shape of each phase is determined from multiple projection images that are sorted to this phase. Moreover, the tumor segmentation is converted into a multiple interrelated surface detection problem based on a graph search framework, which finds the globally optimal solution by solving a maximum flow problem. Constraints on motion and the tumor surface are further incorporated in the framework, which makes the segmentation more robust. The segmentation framework achieves promising results for large tumors. Small tumors are not always visible in the projection images. The accuracy of direct tumor segmentation becomes a problem.

The implementation and validation of the RC reconstruction approach is introduced in Chapter 4. RC reconstruction involves sorting the projection images into several subsets (phase bins) based on the respiratory signal. Each projection image subset is then used to reconstruct a 3D volumetric image. Tumor motion estimation based on RC reconstruction can be suitable for various tumor sizes. The RC reconstruction creates a bimodal MVCBCT, which contains a 3D volume in full exhale (FE) and full inhale (FI) phase respectively. To calibrate the strain gauge, a linear relationship is assumed between diaphragm and tumor motion amplitude between the two phases. The diaphragm to tumor motion ratio (DTMR) is used to measure this linear relationship, which has a mathematical representation as:

$$DTMR = \frac{IHDA_{FI} - IHDA_{FE}}{Tumor_{FI} - Tumor_{FE}} \tag{1-1}$$

The DTMR is further used to divide the IHDA motion amplitude, which is extracted from 2D projection images. The result after the division is the estimated tumor motion amplitude, which will be used to calibrate the strain gauge.

Chapter 5 introduces the motion compensated (MC) reconstruction based on a prior motion model of the lung. Generally, respiratory motion causes motion artifacts in the full reconstructed volume (reconstructed from all the projection images), degrading the accuracy of target localization. RC reconstruction is limited by the view-aliasing artifact caused by an insufficient number of projection images. On the other hand, MC reconstruction is free of the view-aliasing artifacts, since it uses all the projection images. Moreover, it incorporates a prior motion model into the de-convolution process during the back-projection, which makes it also free of motion blur. Usually the motion model is represented by a time sequence of displacement vector fields (DVF). We have studied the feasibility of using a prior model generated from a lung motion model, which is derived by using the method introduced in Chapter 2. We have validated both correlated reconstruction and MC reconstruction based on image quality and clinically significant parameters, such as motion and volume quantification accuracy.

Finally, an enhancement framework of MVCBCT is introduced in Chapter 6. In the MVCBCT 2D projection images, the organ of interest (OOI), such as the diaphragm or the lung, is always superimposed with other anatomical structures and often has low contrast. From this perspective, it would also be promising if one could make the OOI clearer and without overlapping confounding objects through an image enhancement procedure. The enhancement is achieved by forward projection of non-interest organs and tissues of the 3D volume. A study based on image quality and organ localization accuracy shows the feasibility of this approach.

Chapter 7 gives a brief conclusion of this thesis and presents the future directions.

In this introduction chapter, a comprehensive review of management of respiratory motion in radiotherapy is followed, including the problems brought by

respiratory motion, and current image guided radiotherapy (IGRT) techniques applied to account for those problems. Then the description of the mega-voltage cone beam CT (MVCBCT) system is given. MVCBCT is currently equipped in our clinic for daily localization, which is the platform where all the new approaches presented in this thesis were developed and validated.

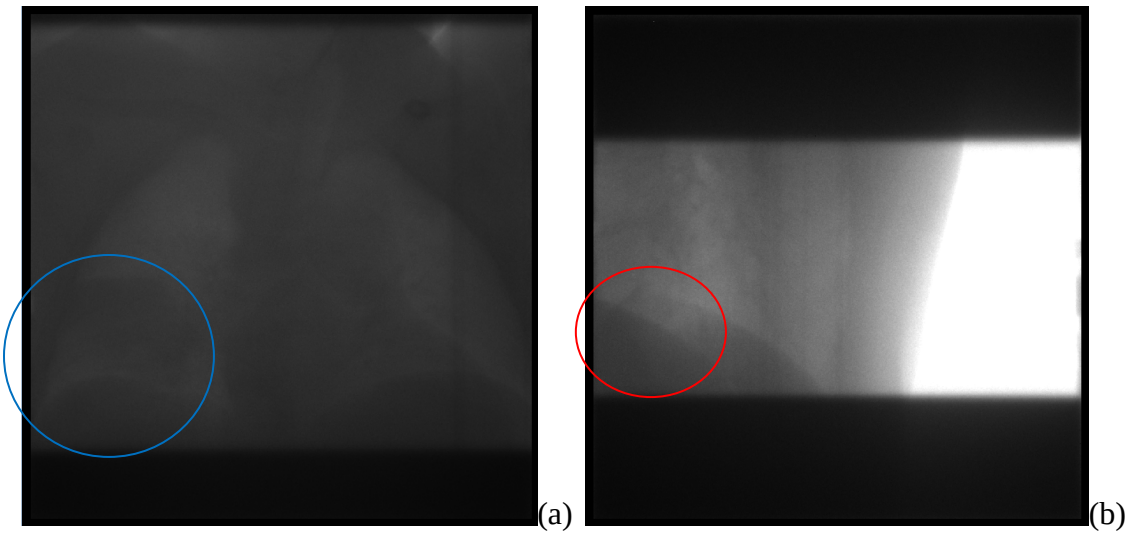

Figure 1-1: Examples of projection image of Mega-voltage cone beam CT: (a) The tumor is visible in the right lower lobe of the lung (blue ellipse). The hemi-diaphragm at the bottom of each lung is visible; (b) a lateral view shows the two hemi-diaphragms overlap with each other, making it difficult to identify diaphragm boundary in the overlapping area (red ellipse).

Figure 1-1 gives one example of an MVCBCT projection image, where part of the tumor boundary has weak contrast. The diameter of the tumor in this patient is about 5 cm, which is very large compared to all the other patient image data that we have derived. For some patients the tumor boundary is not readily identifiable in the projection image even by a human expert.

1.2 Background of respiratory motion management in radiation therapy

Cancer is a worldwide challenge to health. In a world cancer report conducted by the World Health Organization in 2008, cancer was anticipated to overtake heart disease to become the leading cause of death worldwide in 2010 (Boyle & Leven, 2009). The cases of cancer will double by 2020 and will nearly triple by 2030. Among various cancer-related causes of death, cancer in lung and bronchus is estimated to be the leading type in the United States, composing 29% and 26% for male and female respectively (Jemal, Siegel, Xu, & Ward, 2010). The possible treatment of lung cancer includes surgery, chemotherapy and radiation therapy. Recent advances in medicine and engineering have changed the curative effect overtime. According to a recent survey, the five year survival rate among 200 patients diagnosed with stage I non small cell lung cancer (NSCLC), which accounts for 75% to 80% of all lung cancer cases, could improve from 10% to 36% using the modern three-dimensional (3D) conformal radiation therapy (CRT) (Belderbos, Heemsbergen, De Jaeger, Baas, & Lebesque, 2006). However, the worldwide survival rate of lung cancer is still low, with only 14% in 2008.

1.2.1 Mechanics of Respiration

Respiration is the major function of lungs to exchange gas between blood and air. One cycle of breathing can be generally divided into inhale and exhale phases. During the inhale phase, respiratory muscles, such as the diaphragm and intercostal muscles that connect adjacent ribs, contract and descend, pulling the ribs superiorly and anteriorly, thus increasing the volume of the thoracic cavity. The air outside is pushed into the cavity by the transpulmonary pressure. During the exhale phase the respiratory muscles relax

and the lung recoils to its deflated volume. Since the mechanism of the inhale phase requires active participation of respiratory muscles, which is different from the exhale phase, the time frames for inhale and exhale are typically different. The motion trajectory of a specific location in the lung such as that of the tumor varies from inhale to exhale.

The breathing pattern can vary in magnitude, period and regularity. Figure 1-2 compares the position of the ipsi-lateral hemi-diaphragm apex (IHDA) as a function of time of two patients extracted from fluoroscopic images of mega-voltage cone beam computed tomography (MVCBCT), where distinct differences could be observed (details of IHDA motion detection can be seen in chapter 2). The IHDA position along the superior-inferior (SI) direction here serves as the respiratory signal, which is considered as a surrogate of tumor motion. On one hand, respiration is an involuntary action. One can be unconscious about his or her breathing. During unconscious respiration, the periodic cycle is regulated through chemoreceptors by the levels of CO_2, O_2 and pH in the arterial blood. Thus the frequency of respiration is varied during different times. On the other hand, individuals are able to control the magnitude and frequency of respiration within a certain limit. This enables clinicians to use audiovisual feedback to coach the patient during respiration, which has been demonstrated to have a better respiratory regularity (Neicu, Berbeco, Wolfgang, & Jiang, 2006).

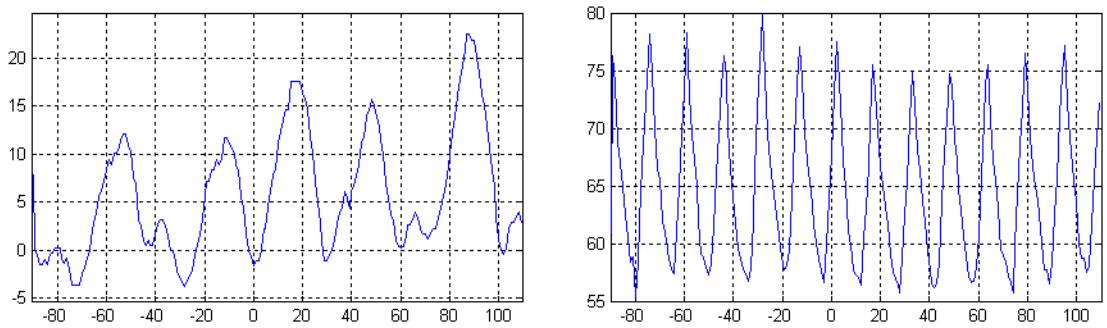

Figure 1-2: Variation of respiratory patterns from two different patients. The horizontal axis is the rotation angle of the Mega-voltage cone beam CT from -90º to 110º. The vertical axis is the superior-inferior position of the ipsi-lateral hemi diaphragm apex in mm, which is a good surrogate of tumor motion and represents the respiratory traces.

1.2.2 Problems of respiration in radiotherapy

Respiratory motion, along with other types of motion such as cardiac, gastrointestinal or skeletal muscular motion, composes the intrafraction motion during radiotherapy. During the entire course of radiotherapy, intrafraction motion limits the accuracy of image acquisition, treatment planning and delivery of radiation. Respiratory motion affects organs and all tumor sites in the thorax and abdomen. Typically lung tumors move from 5 to 10 mm during free breathing. The amplitude could reach to 4.5 cm in some cases (Stevens et al., 2001). For image acquisition, respiratory motion generates artifacts for all imaging modalities, including computed tomography (CT), and positron emission tomography (PET). During a CT scan, different parts of the object move in and out of the CT slice window. Conventional CT reconstruction algorithms that do not account for motion assume that the imaged anatomy is invariant during image acquisition. The motion brings artifacts such as distortion of the target volume and incorrect positional and volumetric information. Figure 1-3 compares the imaging effect of two computed tomography (CT) scans with and without incorporation of respiratory

motion information. Figure 1-3a shows one slice of a 4D CT volume, which is reconstructed from retrospectively-sorted projection images. Figure 1-3b shows one slice of an MVCBCT volume, which is reconstructed from projection images containing all the phases. It can be seen that the boundaries of the tumor and diaphragm are hard to identify in the MVCBCT image.

During treatment planning, to account for the uncertainties in the geographic positions such as intrafraction motion (due to respiration), interfraction motion and setup error, large margins should be added to the clinical tumor volume (CTV) to create a planning target volume (PTV) (using the International Commission on Radiation Units and Measurements (ICRU) report 62 nomenclature (Prescribing, 1993) (DeLaney, 2009). However, large margins limit the dose that can be prescribed. It may also increase the likelihood of treatment-related complications. Apart from respiratory motion, there are also other factors that clinicians should consider when designing the CTV-PTV margin, such as tumor growth and shrinkage, inter or intra-observer variations in GTV delineation, daily variation of respiratory motion, systematic error such as CT artifacts, and patient setup error.

During radiotherapy, the existence of respiratory motion causes a blurring of dose distribution to the anatomy. Using a static beam, the actual dose distribution would become a convolution between the anticipated dose and the probability distribution function of total motion displacements that occur when the beam is on (Lujan, Larsen, Balter, & Ten Haken, 1999). The lung motion limits the accuracy of radiation delivered to the tumor volume. It is reported that the under-dose could reach 30% by using conventional radiation therapy techniques (Ross, Hussey, Pennington, Stanford, & Fred Doornbos, 1990).

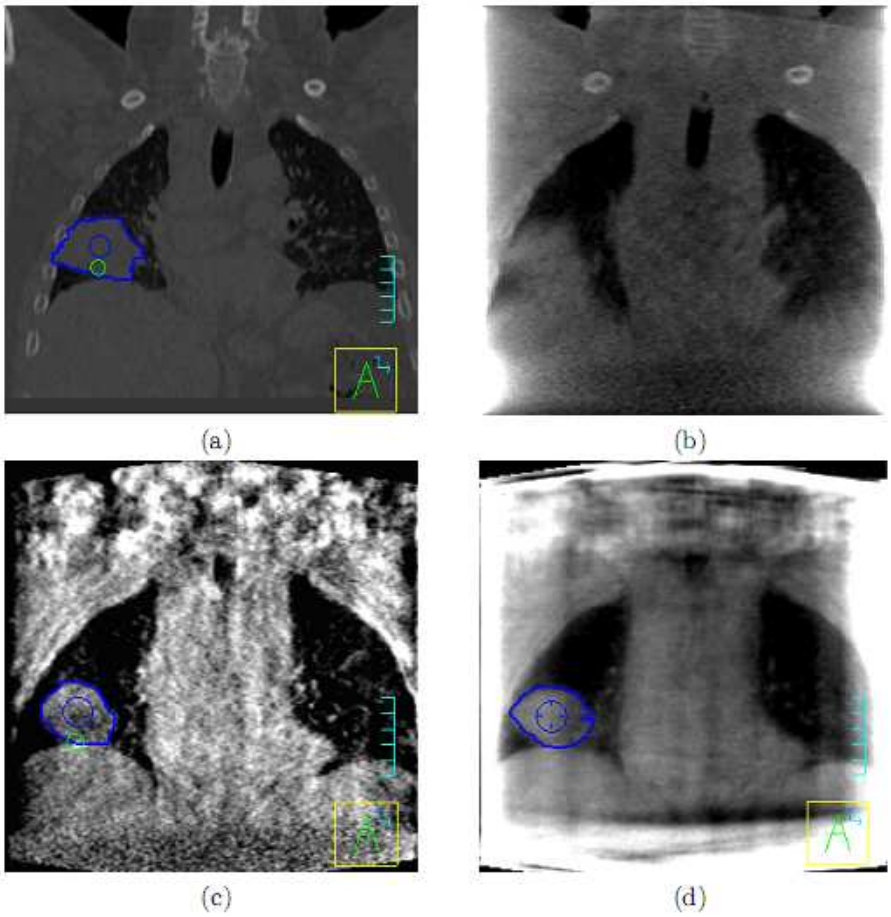

Figure 1-3: Image reconstruction example slice in coronal view: (a) FE phase of planning CT; (b) MVCBCT reconstructed from all the projections; (c) FE phase of RC MVCBCT reconstructed by FDK algorithm; (d) FE phase of RC MVCBCT reconstructed by ART algorithm (tumor contour is displayed in blue)

1.2.3 Respiratory Motion Management

Currently the common approaches of accounting for respiratory motion during treatment can be generally divided into three categories: breath holding, respiratory synchronization and respiratory gating. In this section we will focus on the respiratory gating technique that is currently implemented in our clinic.

Different from the real time tracking system, the gating system turns on the treatment beam only when the tumor moves within a predefined range of positions in the respiratory gating system. Since the dose is not continuously delivered, respiratory gating takes a longer time than real-time tracking. The position and allowed range of the "gate" is usually determined during the planning and localization stage by monitoring the respiratory motion. Usually the gating position is selected where the tumor motion is estimated to be minimal (full exhale) or the lung volume is maximal (full inhale) compared with the rest of the respiratory cycle. Vedam et al (Vedam, Keall, Kini, & Mohan, 2001) reported that the point of full exhale provides the most stable portion of the respiratory cycle, but factors such as increased fraction of lung tissue exposed to radiation, and less separation of lung and critical tissues during the full exhale phase should also be considered. More generally, the gating window is always a trade-off between the duty cycle and the amount of residual motion, where a larger gating window increases the duty cycle and reduces overall treatment time, but increases the tumor motion within the gate. The gating could be either based on motion amplitude or phase. For amplitude-based gating, the gate is a pre-set interval of the relative positions of the tumor. Phase-based gating usually requires an algorithm to compute the relative phase for each sampling time point based on the cyclic nature of the signal. The gate is a window between a start and end phase within each cycle.

The methods to identify tumor position are similar to real time tracking. Currently either external surrogates or internal fiducial markers are used in gating systems. The internal marker faces the problem of pneumothorax (Topal & Ediz, 2003). For external surrogates, there are several commercial respiratory gating systems available, including the Varian Real-time Position Management^{TM} (RPM) system (Varian Medical Systems, Palo Alto, CA), BrainLab (Heimstetten, Germany) ExacTrac Gating/Novalis Gating system and Siemens Medical systems (Concord, CA) linear accelerator gating interface with an Anzai Belt (Anzai medical CO., Tokyo, Japan). The Varian RPM uses an infrared

tracking camera and a reflective plastic box that is placed on the patient's anterior abdominal surface. The ExacTrac system also uses infrared external markers, but it also has X-ray imaging capabilities to determine internal anatomy position. Our clinic uses the Anzai AZ-733V system, which relies on a strain gauge to record the pressure change caused by expansion of a belt strapped around the patient's abdomen.

The planning stage for respiratory gated treatments requires gated CT or 4D CT scans. Both methods can improve the accuracy of target definition and increase sparing of critical structures (D'Souza et al., 2007). For 4D CT, The image acquisition is synchronized with the respiratory signal acquisition. Images are acquired at each couch position for many respiratory phases. Then the phase information is used to sort the raw CT data (projection image) into various phases. Then all the reconstructed images of a particular respiratory phase can be concatenated to form a complete 3D volume. Mean tumor position, tumor range of motion and relation of tumor trajectory to other organs can be derived (Underberg et al., 2004). Currently our clinic is equipped with 4D CT for treatment planning. Different imaging parameters, such as the number of slices and the number of phases, can be applied to the system. For a typical 4D image containing 8 phases and 91 slices, the 4D CT scan can be obtained within a few minutes. Gated CT, on the other hand, is equivalent to a subset of a 4D CT scan. The imaging acquisition is initiated by a trigger that is controlled by the respiratory signal. The gating parameters such as displacement or phase based gating, selection of full exhale or inhale and the window size for gating (duty cycle) are determined prior to the scan.

During the treatment, the correlation between tumor motion and the respiratory trace of the surrogate will be used to gate the beam. It is very likely that the time-dependent tumor motion does not accurately correspond to the respiratory surrogate. Some studies show that the correlation between tumor motion and external surrogate motion cannot be generalized and depends on individual patients (Bruce, 1996; Hoisak, Sixel, Tirona, Cheung, & Pignol, 2004). Other studies show that the tumor residual

motion can be large when the abdominal surface surrogate is used as the resp(Hoisak et al., 2004)iratory signal (Berbeco, Mostafavi, Sharp, & Jiang, 2005; Berbeco, Nishioka, Shirato, & Jiang, 2006) and about 30% of the time the radiation beam will miss the target (H. Wu et al., 2008). It is reported that a -0.65 to 0.3 s phase delay exists between the tumor motion and its abdominal surrogate, while the phase difference between the tumor motion and signal of respiratory volume of lung is -0.3 to 0.5 s. Correlation coefficients vary greatly from 0.39 to 0.99 for both abdominal surrogates and respiratory volume, while respiratory volume has better correlation and reproducibility from day to day (Hoisak et al., 2004). Figure 1-4 illustrates the potential phase difference for an external surrogate. In this figure one can observe the phase delay between the IHDA and the strain gauge signal. Thus the tumor will shift from its desired position during treatment, under-dose the tumor and overdose the surrounding tissues. It is recommended that if a consistent phase delay larger than 0.5 s is observed, the delay should be considered when setting the gate interval (Berbeco, Nishioka et al., 2005).

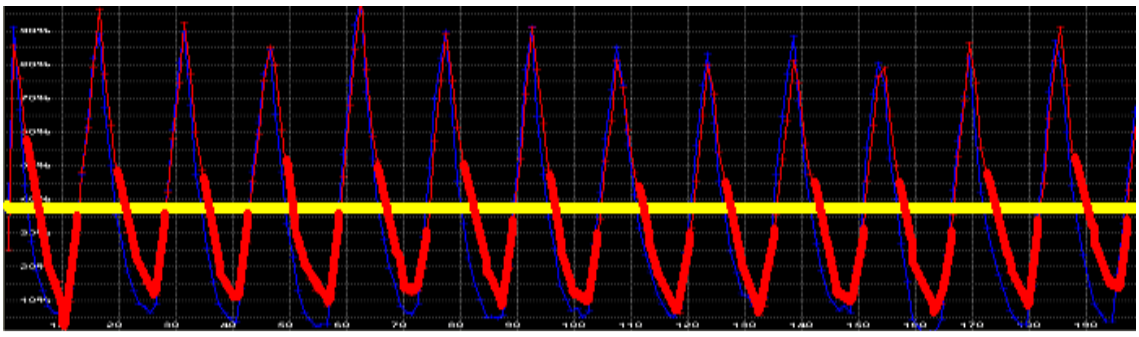

Figure 1-4: The correlation between IHDA position (red curve) and Anzai strain gauge signal (blue curve). Time delays between these two signals can be observed. The horizontal yellow line is a hypothetical amplitude-based gating threshold. If this threshold is applied to the strain gauge signal, the position of the IHDA in real beam-on time is shown in the thick red curve, which will simultaneously cause an overdose to the surrounding tissues during exhale.

Another major problem of using external surrogates is the intra-fractional variation of tumor motion. The tumor motion is likely to change over the course of treatment, which makes the correlation with an abdominal surrogate different from that which was recorded with the planning CT scan. Generally, variation in the respiratory phase can be observed by the signal derived from the external surrogate. However, variation in the range of motion can occur without being detected by the strain gauge. In our clinic, since the therapist calibrates the Anzai gating system to make the full exhale and full inhale phase correspond to 0% and 100% respectively before synchronization, a simple scale to the amplitude of the tumor motion will not change the corresponding strain gauge signal. Figure 1-5: illustrates a typical example, where an increase to the motion amplitude requires a shorter gating window. Applying the original gating window will overdose the surrounding tissues and underdose the tumor.

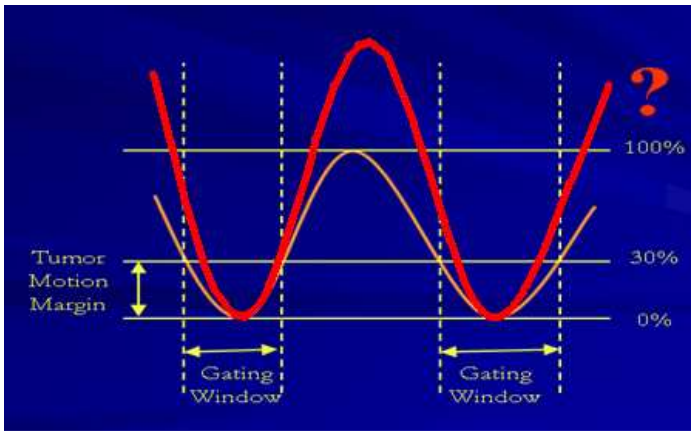

Figure 1-5: A simple illustration showing the problem of correlation using abdominal surrogate: A gating threshold is set as 30% amplitude based on tumor motion during planning (pink curve), and the corresponding gating windows in two cycles are illustrated. On treatment day the amplitude of tumor motion increases to a certain amount (red curve). Applying the gating window the tumor will be outside the desired treatment location during a portion of the duty cycle.

1.3 MVCBCT as a daily localization tool

1.3.1 The requirement for localization

As the advances of modern radiotherapy techniques such as 3D CRT and IMRT provide more and more conformal and accurate dose delivery, there is a concern related to whether the information acquired during the planning CT (such as tumor size, shape, correlation of respiration, etc.) is still accurate and reliable enough to represent the patient during treatment. A procedure, called "localization" (or setup, or patient alignment in some literature) is needed to verify the anatomical and positional information immediately before the treatment and provide more accurate reproducible patient setup. Conventionally portal images have been used to confirm the patient position based on bony anatomy or implanted markers, but this is limited by the time required to process the radiographic film and the extra dose to the patient. The highly sensitive and automated on-board electronic portal imaging device (EPID), such as the amorphous silicon flat panel, is a recent development that breaks through these limits. However, the 2D projection nature of an EPID limits its capability for 3D visualization and verification. Thus there is growing interest in the development of 3D imaging of the patient on the treatment table.

There are several systems that have been developed for this purpose. Generally the beam source of the system could be either based on kilo-voltage (KV) X-rays when used in diagnostic CT or fluoroscopy or mega-voltage (MV) X-rays which are generated from a linear accelerator during treatment. We can categorize the imaging system in a treatment room into 4 groups: (1) A CT-on-rail system, which enables the diagnostic CT scanners to move on a rail installed in the treatment room (Ma & Paskalev, 2006). (2) The kilo-voltage cone beam CT (KVCBCT) system. For most occasions it uses an additional KV X-ray source and EPID attached to the treatment gantry to derive cone

beam images (Oelfke et al., 2006). There is also an implementation of the KVCBCT system on a mobile C-arm (Sorensen, Chow, Kriminski, Medin, & Solberg, 2006). (3) The MV CT system, which either uses the existing treatment machine with an attached arc of detectors (Evans, Gildersleve, Rawlings, & Swindell, 1993), or a helical tomotherapy system that uses an MV fan beam source and a CT ring (Mackie et al., 2003). (4) The MVCBCT system uses the existing treatment machine with an EPID for imaging (Morin et al., 2006; Pouliot et al., 2005).

Our clinic is currently equipped with the Siemens MVision^{TM} MVCBCT (Siemens oncology care systems, Concord, CA) which utilizes an amorphous silicon electronic portal imaging device (Ford, Chang, Mueller, Sidhu, Todor, Mageras, Yorke, Ling, & Amols, 2002a). The device and the illustration of its main components can be seen in Figure 1-6.

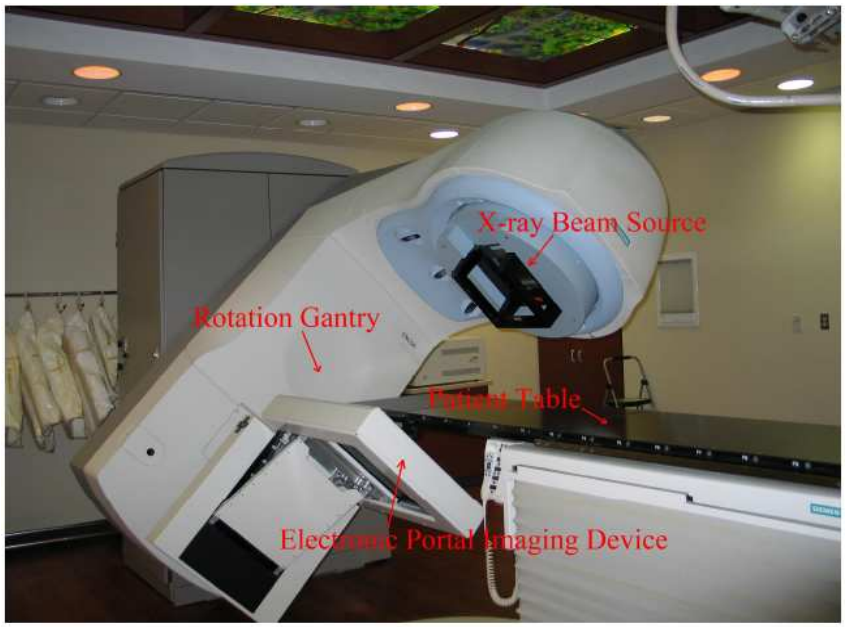

Figure 1-6: Siemens Mvision MVCBCT in the department of radiation oncology, the University of Iowa. The main components are illustrated in the picture.

1.3.2 An overview of MVCBCT

MVCBCT has several protocols on the range of rotation angle for imaging. For example, a clockwise rotation of 200 degrees from -90° to 110°, which is the default protocol (Figure 1-7), or 360 degrees from -180° to 179°. For these two protocols one projection image is generated per degree. The EPID has a 1024×1024 2D detector array, with each element sized in 0.4×0.4 mm^2. The source to axis distance (SAD) is 100cm, while the source to imager distance (SID) is 145cm. The imaging volume at the isocenter is about 27.4×27.4×27.4 cm^3, which is large enough to encompass the size of at least one lung. The shape of the imaging field of view (FOV), is a cylinder with two small cones capping the opposite ends of the rotation axis, due to the cone beam geometry.

Figure 1-7: The gantry of MVCBCT rotates from -90° to 110 in the default protocol.

Although MVCBCT provides a less expensive and more convenient way for patient localization, it should be noted that the imaging quality of MVCBCT is somewhat degraded compared to that of the planning CT, due to the utilization of MeV photons for diagnostic imaging. It is a departure from the general preference for kilo-electron volt (KeV) photons. It is reported that the imaging quality in terms of contrast-to-noise ratio

and spatial resolution of MVCBCT acquired using the 6MV treatment beam is inferior to KVCBCT, even when the dose for MVCBCT is three times that of KVCBCT (Stutzel, Oelfke, & Nill, 2008). The difference of attenuation coefficients between tissues in the KeV range is greater than that of the MeV range as a result of predominant photon interactions with the human body being different. In the MeV range, the primary mechanism of photon interaction is Compton scattering, where the cross section for Compton scattering is quite similar for bone, muscle, and soft tissues. Conversely, photoelectric effect composes the majority of photon interaction in the KeV range, whose cross section for bone is very different than it is for soft tissues, producing a high subject contrast. The exposure setting for MVCBCT ranges from 2 to 15 MUs. Figure 1-1 is an example of one projection image of MVCBCT for a 5MU protocol, which can be considered as one frame of an MV fluoroscopic sequence taken while the gantry rotates. The lung, the tumor located in the lower lobe, and the diaphragm are visible, but the boundaries of the tumor in some parts are not discernible.

A recent development of MVCBCT imaging is to use carbon rather than tungsten as the electron target and to remove the flattening filter for generation of Bremsstrahlung X-rays. This is because low atomic number electron targets like carbon generate more KeV-range photons than high atomic number targets like tungsten, resulting in better imaging quality. The removal of the flattening filter also increases the proportion of KeV-range photons. This method is implemented by the University of California San Francisco and Siemens Oncology Systems (Faddegon, Wu, Pouliot, Gangadharan, & Bani-Hashemi, 2008), which also developed MVCBCT. They replaced the 18-21 MeV electron scattering foil in the target slide with a 4.2 MeV carbon electron target with no flattening filter, which is called the “imaging beam line” (IBL), compared to the traditional “treatment beam line” (TBL). Unlike conventional CT, MVCBCT requires constant geometrical calibration of 3D to 2D projection, since the relative position of the linac X-ray source and the EPID imager may shift over time due to the sagging of

mechanical supports. A special calibration phantom containing 108 tungsten beads is used, while the position in both 3D and 2D projections of those beads can be measured and used to compute the projection matrix. The details of the calibration method can be found in (Pouliot et al., 2005).

The use of MVCBCT brings an additional procedure and dose to the clinical workflow of radiotherapy for lung cancer. In our clinic, the MVCBCT imaging is well integrated into the entire treatment planning process. The workflow begins with a 4D planning CT. After the raw data is reconstructed into multiple 3D volumetric images according to the phase information provided by a synchronized strain gauge, the 4D images are imported into the Pinnacle commercial treatment planning system (Philips, Bothell, WA) that enables one to define the treatment field size, gating window, treatment isocenter, anatomical structures, and beam arrangements to deliver a dose distribution. Using a conventional fractionation, a typical course of radiotherapy for lung cancers involves 30 to 35 daily treatments (6 to 7 weeks, 5 days a week). Hypo-fractionation, on the other hand, aims to increase the biologic dose that increases the daily dose and uses fewer fractions (3 to 5 fractions). Prior to treatment, the patient is imaged with MVCBCT. Immediately after the reconstruction, the 3D volumetric image is registered to the planning KVCT using the COHERENCE^{TM} Adaptive Targeting registration software to determine the patient shifts. The registration is based on maximization of mutual information (Ford et al., 2002). Currently the 3D MVCBCT image is reconstructed from all the projection images. For scans in the thoracic area, this 3D image contains information of all the respiratory phases, which causes the motion blur (Figure 1-3b). A combination of images of 4D phases are used to compare with the motion blurred 3D volume. Further manual adjustment based on the bony anatomy or organ contours is made. Usually the table shift can be made to align the treatment image with the planning CT within 3 minutes after the beginning of the acquisition of MVCBCT. The image acquisition takes about one minute, using the 200 degree standard

protocol. Since a typical respiratory cycle takes about 5 to 10 seconds, there would be about 5 to 12 cycles during a single scan. The reconstruction utilizes a modified Feldkamp, Davis, Kress (FDK) algorithm (Feldkamp, Davis, & Kress, 1984). It begins immediately after the acquisition of the first projection image, and utilizes it for backprojection. For each projection image the backprojection process is quicker than the imaging acquisition, so when all the projection images are acquired the 3D volumetric image can also be derived.

It is reported that 3D MVCBCT provides more accurate patient localization than 2D portal images (Morin et al., 2006). Apart from daily localization, MVCBCT can also be used to monitor patient anatomical changes, calculate dose (Morin et al., 2007), and reduce image artifacts for patients with dense metal objects (such as hip replacements). The details of these applications can be found in (Morin et al., 2006).

1.3.3 Patient data

Over the 5 years of my Ph.D. research, projection images of 96 MVCBCT localization scans from 19 patients have been collected, including a variety of tumor sizes, shapes, locations, imaging regions, etc. The number of MVCBCT scans for each patient ranges from 1 to 24. In the following chapters, there is inconsistency of the number of patient images that are tested among different approaches, and only part of patient images are used for each approach. The limited data set is due to the retrospectively gathered data that does not always have the characteristics that we would need for the analysis. The required characteristics for each method will be further explained in the corresponding chapters. There is no subjective preference of using images belonging to any specific patient.

CHAPTER 2

AUTOMATIC IHDA DETECTION

The diaphragm is a good internal surrogate to tumor motion. However, the practice of using the diaphragm should be adequately validated. A study based on 32 fluoroscopic images from 10 lung cancer patients (Cervino, Chao, Sandhu, & Jiang, 2009) shows promising result that the average correlation factor between the two motions is 0.94 and 0.98, using two regression models respectively. However, a weak correlation can still exist. In some patients with emphysema, unexpected movements of the diaphragm were observed (Iwasawa et al., 2000). So for each patient, one should verify whether the diaphragm can be used as a surrogate during planning and daily localization. Once a strong correlation between the diaphragm and the tumor is verified, we could use the projection images of the MVCBCT scan to (1) quantify the (Ipsilateral Hemi-diaphragm Apex) IHDA motion, (2) verify the diaphragm-tumor motion relationship by phase correlated reconstruction of full exhale and full inhale images and (3) calibrate the strain gauge signal used for gating.

Accurate detection of the diaphragm is the prerequisite step for the adaptive gating system. The respiratory trace of the diaphragm is not only used to calibrate strain gauge signals, but also to establish the phase correspondence of the projection images in various approaches described in later chapters, including organ motion segmentation (chapter 3), correlated reconstruction(chapter 4), motion compensated reconstruction (chapter 5) and projection image enhancement (chapter 6). Although the diaphragm generally has good contrast in most projection images (Figure 1-1a), the accurate detection of the diaphragm in all the projection images of MVCBCT is a challenging task due to the weak boundary in the presence of overlapping confounding organs or tissues (Figure 1-1b). Previous methods that successfully detect or track the diaphragm through

an X-ray image sequence include augmented active shape model (ASM) (Fujita, Chandrasekhar, Singh, & Finucane, 2006) and Hough transforms based on circles (Condurache, Aach, Eck, Bredno, & Stehle, 2005). There are more studies proposed to track the respiratory motion of tumors in fluoroscopic images, including ASM (Q. Xu, Hamilton, Schowengerdt, & Jiang, 2007), template matching (Cui et al., 2007) and optical flow (Q. Xu et al., 2008). However, it should be noted that MVCBCT projection images are very different from the fluoroscopic video. The contrast of MVCBCT projection images is much lower. The projection angle of the beam is fixed for fluoroscopic video, while for MVCBCT systems the gantry rotates during image acquisition. Some methods suitable for fluoroscopic images, such as using the average image intensities within a region of interest to estimate the respiratory phase (Berbeco et al., 2005), may not be suitable to MVCBCT projection images. Besides, the frame per second (FPS) rate for MVCBCT projections is only about 3, which is much less than that of a fluoroscopic video. All those features make the diaphragm detection in MVCBCT images more difficult. Moreover, for the purpose of online calibration of the strain gauge to tumor motion before daily treatment, the time spent on diaphragm detection should be within a clinical limit, which is recommended to be one minute at most.

In this chapter, an automatic IHDA detection framework is presented. Generally, it is composed of three sequential parts: (1) Confine the IHDA motion in projection images within a narrow region of interest (ROI) based on user initialization; (2) automatic detection of diaphragm boundary and IHDA position; (3) derive the 3D IHDA motion trajectory from the 2D image coordinates. In the following paragraphs, section 2.1 introduces how to determine the region of interest of the IHDA within each projection image based on manual initialization in four frames. Sections 2.2 and 2.3 introduce two IHDA detection approaches, which are both based on converting the image space into a Hough space by using a double-parabola model. The pros and cons of these two methods are discussed. Section 2.4 introduces a fully automatic IHDA detection framework based

on pre-segmentation of the diaphragm in 3D reconstructed volumes. Comparison of the fully automatic approach against the semi-automatic approach is made based on the detection accuracy.

2.1 Manual initialization of IHDA ROI

It can be seen from Figure 1-1 that the diaphragm only takes up a small portion of the area of the projection image. It would be convenient if an ROI can be determined prior to the diaphragm detection, thus the process of image analysis and diaphragm detection can be confined in this area. To create this ROI, we have developed a robust approach based on an interpolated ray tracing algorithm. The method was firstdeveloped and validated by Dr. Siochi before my arrival to the University of Iowa. One could refer to his paper as (Siochi, 2009) for details.

Generally, this method computes the 3D position of the IHDA from corresponding 2D positions in two projection angles (Figure 2-1). The IHDA motion is assumed to be confined in a rectangular box (shown as green), where the location of FE and FI phase forms two diagonal vertices of the rectangular box (the blue curve). Thus we can derive the range of IHDA motion based on 3D FE and FI positions. These two positions are further re-projected onto each projection plane, generating a 2D bounding rectangle. Thus a region of interest (ROI) is derived for image processing and IHDA detection. Once the IHDA is detected in each 2D projection image, it is backprojected to 3D coordinates to derive the motion trajectory. The 3D position is an approximation between FE and FI points based on linear interpolation along the longitudinal coordinate (v coordinate in image plane and z for room coordinate, perpendicular to the paper in Figure 2-1). The error of this interpolation is within a sub-millimeter.

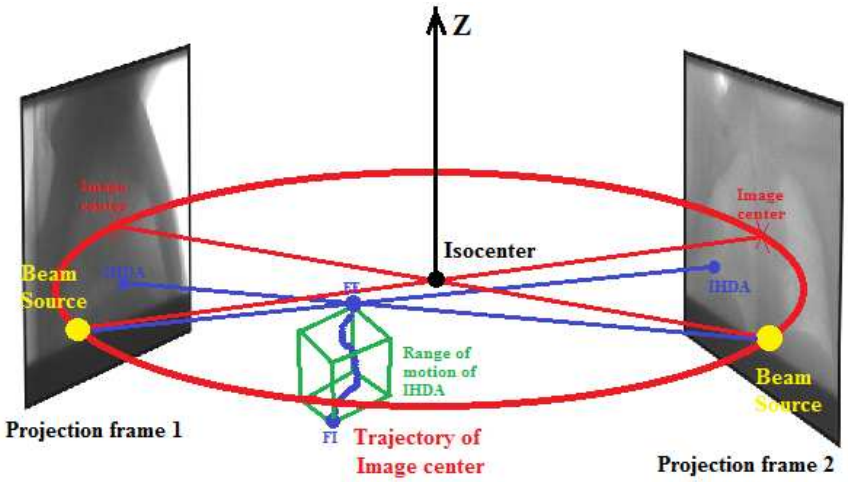

Figure 2-1: A 3D illustration of cone beam geometry of 3D to 2D projection. The large red circle is the trajectory of image center. Two projection images are acquired in different viewing angles. The red line represents the ray that projects the isocenter onto the image center (Strictly speaking, there would be some small deviation due to the variation of system geometry. But the projected position of isocenter would be very close to the image center). The blue line represents the perspective projection of the IHDA in two corresponding 2D positions. Note that the beam source is not necessarily on the same trajectory with the image center.

There are several advantages of the interpolated ray tracing method. First, the two projection images used to determine the 3D IHDA position can be from arbitrary viewing angles, though best accuracy is achieved when they are more or less 90° apart. This gives the user more freedom to initialize 2D IHDA positions. Second, it is very likely that the two initialization points do not correspond to the same 3D locations. This could be due to the variation of the amplitude of respiration in each phase or manual initialization error. The interpolated ray tracing algorithm allows the two projection rays to be non- coplanar (i.e. not strictly intersect in 3D), since the computation of the intersection of the two rays is not directly solved in 3D geometry. Instead, the intersection point is computed in a 2D axial plane after orthogonal projection (Figure 2-2). Based on the relationship of similar triangles, the *z* direction (Cranio-Caudal direction) can be computed as

$$z_d = \frac{l_p}{l_d} z_p \tag{2-2}$$

where l represents the distance of a specific point in 3D location to the beam source. The subscript d and p represents the 3D position of the original IHDA and its projection respectively.

The interpolated ray tracing method was validated in Dr. Siochi's experiment, achieving a sub-millimeter error based on a phantom with predefined motion.

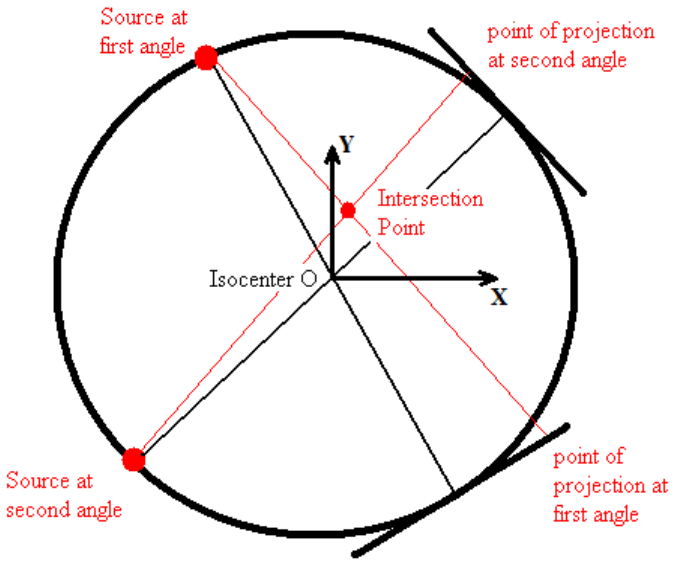

Figure 2-2: Computation of 2D coordinates of intersection point using interpolated ray tracing algorithm. The two rays of perspective projection from two angles more or less 90 degrees apart are projected onto the axial plane. The x and y coordinates of the intersection point is determined by the two rays. The z coordinate is interpolated from the projected point in the detector.

2.2 Double-parabola model

In Dr. Siochi's paper (Siochi, 2009), an efficient algorithm was proposed to detect the boundary of a tungsten pin of an imaging phantom in 2D projection images based on histogram thresholding. This algorithm works successfully for a tungsten pin, but the accuracy is not guaranteed when it comes to patient imaging, since there is more irregularity and noise presented (Figure 1-1). During the first two years of my Ph.D. research, we have developed two automatic diaphragm detection approaches for step (2). Both methods are based on a Hough transform based on a double-parabola shape template. The first approach is based on the global optimization of a dynamic Hough transform (DHT), while the second one is a tracking approach by finding a probability density function (PDF). The mathematical representation of the model is:

$$y = y(x) = \begin{cases} a_1(x - x_0)^2 + y_0, \; for \; x < x_0 \\ a_2(x - x_0)^2 + y_0, \; for \; x \geq x_0 \end{cases} \tag{2-3}$$

where the four parameters are (x_0, y_0, a_1, a_2). (x_0, y_0) represents the position of the parabola vertex (which also represents the IHDA) and a_1 and a_2 are four times the focal length of each parabola segment. The double-parabola model is shown to be superior to some other templates. Simple shapes, such as a single parabola or arcs of an ellipse, also resemble a hemi-diaphragm. However, we chose a double-parabola model because the hemi-diaphragm is asymmetrical in some lateral views (Figure 1-1). We have generated a training set of diaphragm ROI from the MVCBCT projection images and have manually drawn the contour of the diaphragm. Then the contours are fitted with a single parabola, ellipse arc and double parabola based on the least square fitting. The root-mean-square error between the contour and the fitting model are 0.98, 0.81, and 0.24mm for single parabola, ellipse arc and double parabola, respectively.

Given the shape template with the parameter set (x_0, y_0, a_1, a_2) at frame t within the ROI, the Hough value measures how well the double-parabola template matches the image by adding the cost values at pixels along the shape contour,

$$H(x_0, y_0, a_1, a_2, t) = \sum_{(x,y)\in shape} g(x,y) = \sum_{x=x_0-\Delta x}^{x_0+\Delta x} c(x, y, a_1, a_2, x_0, y_0),$$

(2-4)

Thus, the 2D image sequence is transformed into a five-dimensional (5D) Hough parameter space

$$I(x, y, t) \rightarrow H(x_0, y_0, a_1, a_2, t),$$

(2-5)

Function $c(x,y,a_1,a_2,x_0,y_0)$ is the cost value determined by both the projection image and the parameters of the parabola model. It is computed as

$$c(x, y, a_1, a_2, x_0, y_0) = \begin{cases} N_x(x,a_1,x_0)\cdot\dfrac{\partial I(x,y)}{\partial x} + N_y(x,a_1,x_0)\cdot\dfrac{\partial I(x,y)}{\partial y}, & for\ x < x_0 \\ N_x(x,a_2,x_0)\cdot\dfrac{\partial I(x,y)}{\partial x} + N_y(x,a_2,x_0)\cdot\dfrac{\partial I(x,y)}{\partial y}, & for\ x \geq x_0 \end{cases}$$

(2-6)

where the function $N(x,a,x_0)$ is the normal direction of the parabola contour as a function of the horizontal direction x, and a and x_0 (the normal direction is not influenced by y_0). N_x and N_y represents the component of the normal vector in x and y directions, respectively. $I(x,y)$ represents the intensity of pixel (x,y) of the projection image. The cost function in equation (2-6) is actually a dot product between two 2D vectors: the normal direction of the parabola and the image gradient at (x,y). In this way, a high cost value will be given if one pixel has high gradient amplitude and similar gradient direction with the normal direction of the parabola. Figure 2-3 illustrates the difference between the two vectors in one projection image:

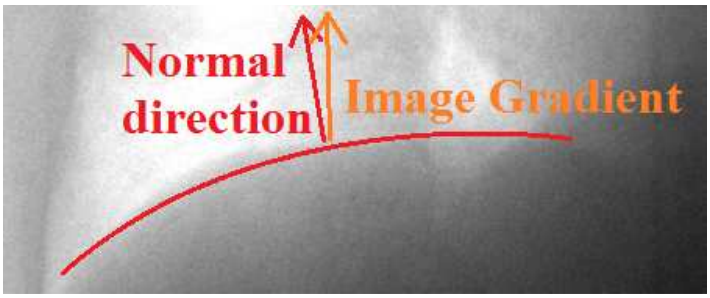

Figure 2-3: An illustration showing the normal direction of a parabola curve and the image gradient at the corresponding point location

The normal direction of the parabola function can be computed as

$$N_x(x,a,x_0)=\frac{2a(x-x_0)}{\sqrt{4a^2(x-x_0)^2+1}},\ N_y(x,a,x_0)=\frac{1}{\sqrt{4a^2(x-x_0)^2+1}} \tag{2-7}$$

Analyzing the 5D Hough space requires a lot of time and memory. To speed up the detection process, the Hough accumulator array is reduced to three dimensions from the original five dimensions.Within each frame *t*, for each (x_0, y_0) cell we select the maximal value among all the combinations of (a_1, a_2), and use a separate array to record the corresponding (a_1, a_2). The mathematical representation is as follows:

$$H(x_0,y_0,t)=\max_{a1,a2} H(x_0,y_0,a_1,a_2,t), \tag{2-8}$$

An illustration of converting the image space to Hough accumulation space is shown in Figure 2-4.

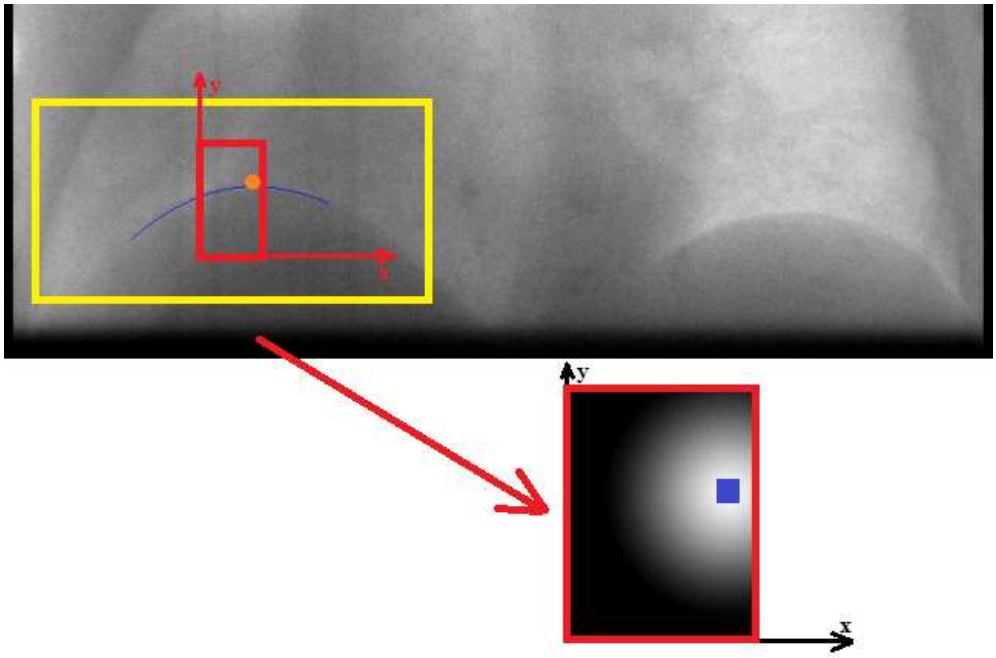

Figure 2-4: A simple illustration of one cell (blue rectangle) in Hough space (below) corresponds with the double parabolic shape (blue contour) in image space (top). The red rectangle in both image space and Hough space represents the range of motion of IHDA determined by interpolated ray tracing algorithm. The yellow rectangle in image space represents the area used for gradient computation and Hough accumulation.

2.3 Dynamic Hough transform (DHT)

DHT, originally proposed by Lappas et al. (Lappas, Carter, & Damper, 2002; Lappas, Damper, & Carter, 2006) for an application of Pingpong ball detection in a video, is a natural extension of the traditional Hough transform (Ballard, 1981) to object motion detection in a time sequence of images. Instead of searching for the Hough peak in one single image, DHT aims to detect a trajectory of the object in motion. It transforms each image frame into the Hough space and uses a sequence of Hough peaks to represent the trajectory. Its direct predecessor is velocity Hough transform (VHT), where constant motion speed is assumed (Nash, Carter, & Nixon, 1997). For DHT, both the change in

motion amplitude and direction is allowed. And it uses a dynamic programming algorithm to find the optimal motion trajectory based on an energy function.

Previous work of diaphragm detection using Hough based approach include Condurache et al. (Condurache et al., 2005), where standard Hough transform of circle model was employed to detect diaphragm in cardiac X-ray projection images, followed by refinement of active contour model (ACM). There are two major advantages of our method: (1) the DHT framework enables to establish inter-frame constraint and global optimization; (2) we have used a double parabolic model, which is a better representation of diaphragm shape than other analytical models, such as circle (Condurache, Aach, Eck, Bredno, & Stehle, 2005), ellipse, and single rotational parabola. The model is composed of two parabolic segments, which shares the same symmetrical axis and vertices.

For each projection image indexed *t*, we look for a vertex $(x_0(t), y_0(t)$ with the corresponding maximizing a_1 and a_2 values and form a trajectory through accumulation space by maximizing an energy function. Similar to Lappas' original work (Lappas et al., 2002; Lappas et al., 2006), the energy function is optimized that takes account of Hough value and penalties of change in motion and direction. The difference lies in the curvature of the diaphragm, which makes the diaphragm shape able to deform through the image sequence. An additional component is added to the energy function to incorporate the penalties of shape deformation. The overall energy function is as follows:

$$E_{traj} = w_1 E_{hough} - w_2 E_{motion} - w_3 E_{direction} - w_4 E_{deformation}$$

(2-9)

The Hough energy is the summation of the Hough values of all the points on this trajectory in accumulation space:

$$E_{hough} = \sum_{t=1}^{200} H(x_0(t), y_0(t), t),$$

(2-10)

The motion energy is a penalty that discourages speed differences in diaphragm motion:

$$E_{motion} = \sum_{t=2}^{200} (w_{vx}(v_x(t) - v_x(t-1))^2 + w_{vy}(v_y(t) - v_y(t-1))^2),$$

(2-11)

Here, v_x and v_y are the speeds in horizontal and longitudinal directions in image space, respectively, where $v_x(t)=x_0(t)-x_0(t-1)$ and $v_y(t)=y_0(t)-y_0(t-1)$. w_{vx} and w_{vy} are the corresponding weights on the speed changes. For simplicity, the speed is the displacement between two successive frames, since the time between frames is approximately constant. The direction energy is a penalty for changes in the velocity direction,

$$E_{direction} = \sum_{t=2}^{200} (\arctan(\frac{v_y(t)}{v_x(t)}) - \arctan(\frac{v_y(t-1)}{v_x(t-1)}))^2,$$

(2-12)

The deformation energy is different from that of Lappas, which penalizes changes in rotation and scale for rigid shape templates. We use the focal length parameter a_1 and a_2 to account for deformation of the two parabola segments

$$E_{deformation} = \sum_{t=2}^{200} [(a_1(t) - a_1(t-1))^2 + (a_2(t) - a_2(t-1))^2],$$

(2-13)

Equations (2-11), (2-12) and (2-13) are soft constraints that suppress but do not prohibit large changes. In order to prevent some obvious irregular changes in motion and Hough value, we also apply hard constraints that forbid changes above a certain threshold: (a) The IHDA displacement should not exceed Δx_0 and Δy_0 between adjacent views and (b) the Hough value of the current view should be a factor α times greater than that of the previous view:

$$\max(E_{traj}) \; subject \; to \begin{cases} H(t) > \alpha H(t-1) \\ |x_0(t) - x_0(t-1)| \le \Delta x_0 \\ |y_0(t) - y_0(t-1)| \le \Delta y_0 \end{cases} \tag{2-14}$$

Equation (2-14) is a constraint optimization problem. The energy term E_{traj} is a function of the IHDA location of Hough peaks in all the views. Because the energy terms in equation (2-9) can be grouped into 198 sets of three related frames, we followed the "dynamic programming" procedure in Lappas' work (Lappas et al., 2002) to solve the optimization problem.

2.4 Tracking based on probability density function (PDF)

To successfully detect the IHDA, the IHDA through projection images should correspond to the Hough cell with the largest Hough value. However, this assumption fails in a few cases when the confounding objects have stronger Hough accumulation values than the diaphragm. The contra-lateral hemi-diaphragm, which is the part of the diaphragm under the other lung and has almost identical shape features, is the major source that misleads the detection. Generally this problem occurs in the lateral views (250~290° and 70~110° for standard protocol) where the two hemi-diaphragms are projected very close to each other (Figure 1-1b) and the ROI is unable to exclude the confounding one. Figure 2-5 shows one example of Hough parameter space.

To correct the confounding problem in DHT, the detection method should incorporate other features of Hough space, rather than the intensity of Hough value alone (the first term in equation (2-9). In Figure 2-5, it can be observed that the correct IHDA trajectory is generally a continuous curve, with each point a local maxima (peak) in Hough space. And the value of those Hough peaks change gradually among adjacent

frames. Intuitively we could add another penalty or constraint in DHT framework based on the difference of Hough accumulation value between two peaks in adjacent frames. However, it is hard to find one such value that can be applied to all the images.

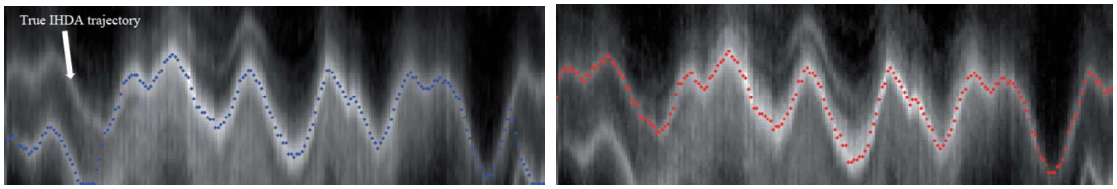

Figure 2-5: The Hough accumulator array displayed as maximal intensity projection on 2D (SI direction and time) overlaid with detected IHDA trajectory. **Left**: The detected IHDA position is attracted to contra-lateral hemi-diaphragm using DHT approach. **Right**: The detected IHDA position based on probabilistic tracking in Hough space.

To address this issue, a tracking-based approach is developed, which also takes advantage of using Hough space and double parabola model. However, instead of simultaneously detecting all the peaks based on global optimization, a tracking scheme based on searching for Hough peaks with maximal probability density function (PDF) is applied. The tracking starts from four user initialized frames and spreads to neighboring frames. It is more clinical useful, since only a few neighboring frames need to be corrected when the user wants to modify the detection result in some frames.

The Hough Transform and probability have a very strong relationship. Early in 1991, Stephens (Stephens, 1991) defined a mathematically “correct form” of the Hough transform from a probabilistic perspective, which takes the log of the probability density function of the image output parameters based on a Bayesian framework. Kiryati et al. proposed a probabilistic Hough transform, which only selects a subset of edge points for the voting stage to compute the Hough accumulator array (Kiryati, Eldar, & Bruckstein, 1991). Xu et al. (L. Xu, Oja, & Kultanen, 1990) proposed a randomized Hough transform

approach, which used a many-to-one mapping from image space to parameter space. The presented method is originated from Hills et al.'s work (Hills, Pridmore, & Mills, 2003), where they tracked a set of combined features in a video by estimating a joint PDF in Hough space. Mills et al. (Mills, Pridmore, & Hills, 2003) further combines Hough transform with extended Kalman filter.

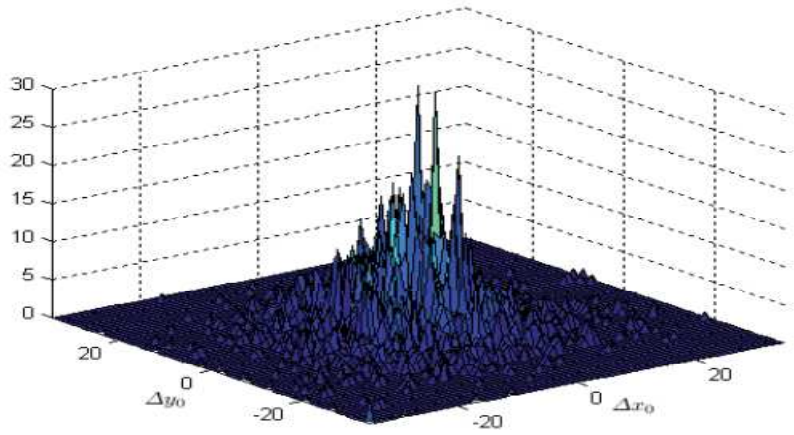

Figure 2-6: Distribution of IHDA motion in time sequence of projection images from 21 MVCBCT fractions. The distribution of motion is represented by Δx_0 and Δy_0.

The main assumption of our approach is that the Hough peaks of IHDA in adjacent frames have very similar parameters, including the position x_0, y_0, curvature of parabola a_1, a_2, and the Hough value. Given a set of Hough parameters (x_0, y_0, a_1, a_2) at frame t, which we denote as $(x_0^t, y_0^t, a_1^t, a_2^t)$, the PDF of parameters in the next frame $(t+1)$ is assumed to be normally distributed, with the mean equal to the parameter set in frame t, which has the mathematical representation:

$$f(p^{t+1} \mid p^t) = k_p e^{-\frac{(p^{t+1}-p^t)^2}{2\sigma^2}} \quad (2\text{-}15)$$

In this equation *p* represents any pattern measurement, including Hough parameter x_0, y_0, a_1, a_2, and the Hough value. The parameters *k* and σ are the normalization parameter and deviation of Gaussian distribution respectively. So once all the Hough peaks in the frame *(t+1)* are detected, the probability of each peak can be estimated using the joint probability of all the parameters. The Hough peak with maximal PDF is selected as the next IHDA position. The assumption of normal distribution is validated using the experimental result from MVCBCT projection image sequences.

The tracking approach starts from the four manual initialized frames. For a given frame *t* with the detected IHDA position *(x(t),y(t)* shape parameter $a_1(x(t),y(t),t)$ and $a_2(x(t),y(t),t)$, the algorithm tries to find the IHDA position in the next frame *(t+1)* or *(t-1)* and subsequently repeats this process. All the Hough peaks are selected prior to the tracking process, which are local maxima of *H(x,y,t+1)*. For each Hough peak, a PDF is evaluated to give the likelihood of moving from a previous point location to this one, represented by:

$$f(x^{t+1}, y^{t+1}, a_1^{t+1}, a_2^{t+1}) = f_x(x^{t+1} \mid x^t) f_y(y^{t+1} \mid y^t)$$
$$f_a(a_1^{t+1} \mid a_1^t) f_a(a_2^{t+1} \mid a_2^t) f_{cor}(x^{t+1}, y^{t+1} \mid x^t, y^t)$$

(2-16)

where we use the superscript "x^t" rather than "*x(t)*" to represent the function of time. The PDF is multiplied by five components where each of the first four components measures the conditional probability of one model parameter (x,y,a_1,a_2). For example, $f_x(x^{t+1}|x^t)$ represents the probability of moving from position x^t in frame *t* to x^{t+1} in frame *t+1*. George et. al. found that the PDF for diaphragm motion can be considered an approximately normal distribution(George et al., 2005). In this study we further assume that both the IHDA motion and the curvature of a_1 and a_2 are normally distributed. The first four components are normally distributed, where the mean equals the value of the model parameter in *t*. The fifth component f_{cor} measures the probability based on the

normalized cross correlation between two regions. It is determined by the neighborhood of (x^{t+1},y^{t+1}) and (x^t,y^t) in the Hough accumulation array $H(x,y,t)$. The closer the correlation is getting to one, the higher the probability value. The conditional probabilities of the five components have the mathematical representation as follows:

$$f_x({x_0}^{t+1} \mid {x_0}^t) = k_x e^{-\frac{({x_0}^{t+1}-{x_0}^t)^2}{2{\sigma_x}^2}}, \quad f_y({y_0}^{t+1} \mid {y_0}^t) = k_y e^{-\frac{({y_0}^{t+1}-{y_0}^t)^2}{2{\sigma_y}^2}}, \quad f_a(a^{t+1} \mid a^t) = k_a e^{-\frac{(a^{t+1}-a^t)^2}{2{\sigma_a}^2}}$$

$$f_{cor} = k_{cor} e^{-\frac{(NCC({x_0}^{t+1},{y_0}^{t+1},{x_0}^t,{y_0}^t)-1)^2}{2{\sigma_{cor}}^2}}$$

(2-17)

The function f_a is used for both component a_1 and a_2. The Gaussian window σ is derived from a statistical analysis of the manual IHDA identification results on 40 MVCBCT scans from 6 patients. Figure 2-6 shows the distribution of IHDA displacements of x_0 and y_0, which is similar to a 2D Gaussian distribution.

For both DHT and PDF based tracking approach, the IHDA position in 2D projections are converted to the 3D coordinate system based on the interpolated ray tracing method (Siochi, 2009).

2.5 Towards fully automatic procedure: Automatic ROI detection

The interpolated ray tracing algorithm used to determine ROIs in the projection images requires the manual initialization of point locations in two projection images at full exhale (FE) and full inhale (FI) respectively. However, the process of human initialization on four projection images requires special training to the clinicians to make them understand the principles and get familiar with the software. Moreover, manual initialization could be time consuming, especially for those images with low contrast of

diaphragm and confounding tissues. Instead, the determination of ROIs could be made fully automatic. In this section we introduce a new approach that can automate this process.

2.5.1 General framework

Figure 2-7 illustrates the main steps of this method, with the intermediate results shown in Figure 2-8.

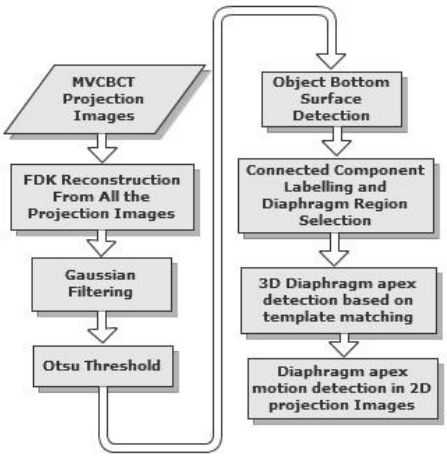

Figure 2-7: Flowchart of the fully automatic IHDA detection framework

First a 3D volume is reconstructed from all the projection images. Though this volume contains motion artifacts (see Figure 2-8a), it does not influence the robustness of a rough estimation of the IHDA position. The reconstructed volume is first pre-processed by a Gaussian smoothing filter, which reduces the noise and makes the voxel intensity more homogeneous inside the lung (Figure 2-8b). Then both lungs are segmented based on Otsu's method, which automatically performs image thresholding (Otsu, 1975). An

optimal threshold is exhaustively searched that minimizes the intra-class variance in the image histogram (Figure 2-8c). Based on the segmented lung mask, a subset of voxels, called “bottom surface” is detected, which is located in the most inferior position of the mask. Not all of the “bottom surface” voxels are on the diaphragm surface: the superior surface of the tumor and the small part of lung wall as seen in Figure 2-8d are not a part of the diaphragm surface. A morphological analysis is performed to eliminate all the “bottom surfaces” that are not a part of the diaphragm surface. The corrected diaphragm surface is shown in Figure 2-8e and Figure 2-8f.

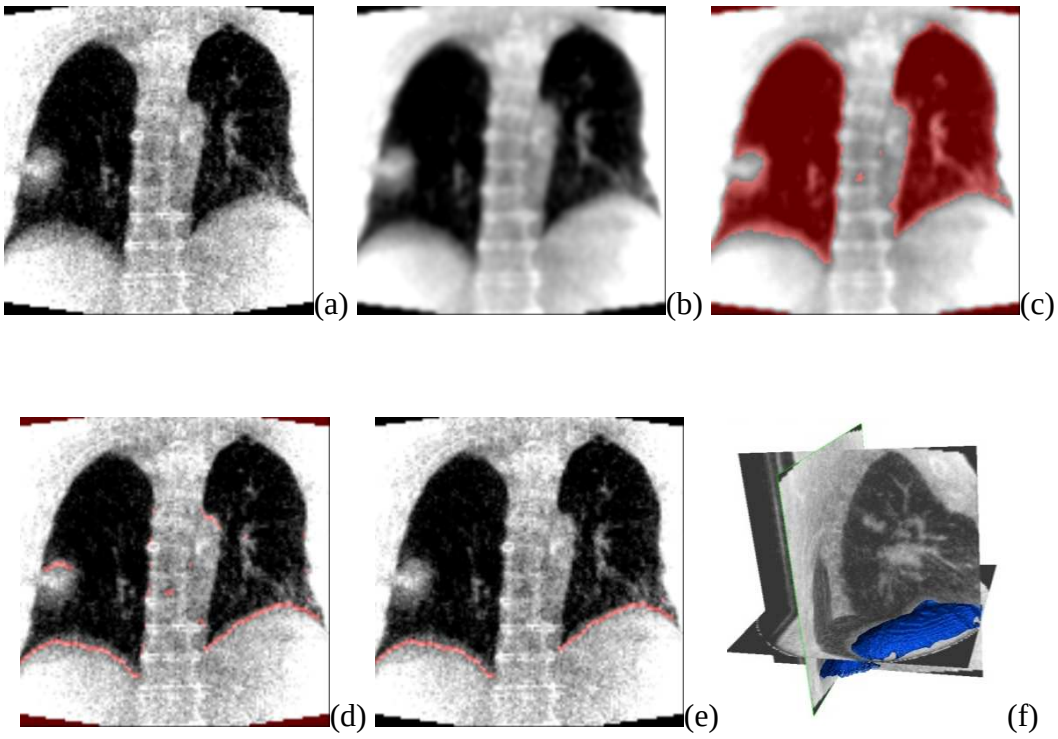

Figure 2-8: Intermediate result of the proposed method: (a) A coronal slice of reconstructed MVCBCT volume; (b) The coronal slice after Gaussian filtering; (c) Result of Otsu thresholding (red binary mask); (d) Bottom surface of the Otsu segmentation (pink contour); (e) Diaphragm surface detection; (f) Diaphragm surface overlaid on 3D visualization of MVCBCT volume

The rough 3D position of IHDA is selected from the voxels of the diaphragm surface. The number of hemi-diaphragms presented in the 3D volume can be analyzed from the binary mask of the diaphragm surface (two for Figure 2-8e, but one in cases where only one lung is entirely visible in the FOV of the volume). A template matching approach is employed to find the location of the most suitable voxel of one hemi-diaphragm surface to serve as the rough IHDA position. This 3D position is then projected onto each 2D projection image. A margin is added to the projected location to generate an ROI, which is the working area for 2D motion detection approach.

2.5.2 Diaphragm surface detection via morphological analysis

In order to locate the diaphragm surface from a binary image of the lung mask using morphological analysis, we begin by assigning a binary value to each voxel in a binary image voxel (x,y,z). Voxels in the lung region are assigned an intensity value of $I(x,y,z)=1$, while voxels outside of the lung region are assigned a value of $I(x,y,z)=0$. To generate the bottom surface illustrated in Figure 2-8d, a condition check is performed to each voxel in the volume. A voxel is only considered to be bottom surface if both $I(x,y,z)=1$ and $I(x,y+1,z)=0$. The superior-inferior (SI) direction of the volume is defined by y and the inferior direction is defined by $y+$.

The bottom surface detection generates a new binary image $B(x,y,z)$, where a voxel is defined by $B(x,y,z)=1$ if it belongs to the bottom surface. An algorithm is implemented to uniquely label the connected components of the bottom surface (Cormen, 2001). To separate the bottom surfaces from the diaphragm surface, we applied stringent criteria to each connected component:

(1) The size of the connected component should be larger than a threshold $T_{size1;}$

(2) For each component, there is no other component with a size larger than threshold T_{size2} located inferiorly to it. For two connected components A and B, that B is inferior to A is defined as follows: there exists two voxels $a(x_a,y_a,z_a)$ and $b(x_b,y_b,z_b)$, $a \in A$ and $b \in B$ that $x_a=x_b$, $z_a=z_b$, $y_a<y_b$.

The size of each bottom surface is computed simultaneously with the connected component labeling algorithm. The second separation criterion is performed after the labeling process. If the first criterion is satisfied for each component, the algorithm will then search for the voxels located inferiorly to it.

2.5.3 IHDA position estimation via template matching

Once the diaphragm surface binary image is derived, template matching is performed to find the IHDA position for each hemi-diaphragm. A parabolic surface model is applied to represent the shape template of the diaphragm surface, with a function of:

$$y = y(x,z) = a_1(x-x_0)^2 + a_2(z-z_0)^2 + y_0 \tag{2-18}$$

where there is a corresponding y value in the SI direction to represent the height of the diaphragm surface for each combination of x and z in the lateral and anterior-posterior direction. The parameters x_0, y_0 and z_0 describe the IHDA position, which is the most superior point on the diaphragm surface. a_1 and a_2 describe the curvature of the parabolic surface in x and z directions. To find the IHDA, an exhaustive search is performed for all the possible combinations of these parameters to determine a parabolic surface: x_0, y_0, z_0, a_1 and a_2. Although an exhaustive search in five-dimensional space is very time-consuming, this does not adversely affect our application because the allowed range of those parameters is restricted. The range, x_0, y_0, z_0 is selected from the small

number of 3D volume voxels on the diaphragm surface as seen in Figure 2-8e. The flatness of the diaphragm surface near the IHDA position makes the a_1 and a_2 value very small. The exhaustive search aims to find the optimal solution, which has the largest energy function:

$$E(x_0, y_0, z_0, a_1, a_2) = \sum_{x=x_0-\Delta x}^{x_0+\Delta x} \sum_{z=z_0-\Delta z}^{z_0+\Delta z} c(x, y(x, z, a_1, a_2, y_0), z) \tag{2-19}$$

where Δx and Δz defines the size of the parabolic surface. Function $c(x,y,z)$ is the cost image computed from the original 3D volume. For each voxel, the intensity of $c(x,y,z)$ represents the likelihood of becoming a part of the diaphragm surface. Currently we set the cost value equal to the gradient in a SI direction. Although the parabolic function representation is only an approximation of the diaphragm surface, it is an effective way to estimate the rough 3D IHDA position.

2.5.4 Derive 3D IHDA position from 2D projection space

Once the IHDA ROI is determined, one can use the DHT or PDF based tracking approach to detect the IHDA within the defined ROIs. One difference of using PDF based tracking approach from manual initialization is the starting frame. For manual initialization, the tracking could be started from the 4 initialized frames. For automatic approach, For PDF-based tracking, the IHDA position is determined on two projection images t_1 and t_2 by automatically selecting the maximal accumulation value in the Hough space ($H(x,y,t_1)$, $H(x,y,t_2)$. For a standard MVCBCT protocol, t_1 and t_2 is chosen at frames near 60 and 120 respectively, where there is no overlapping between the two hemi-diaphragms at those angles.

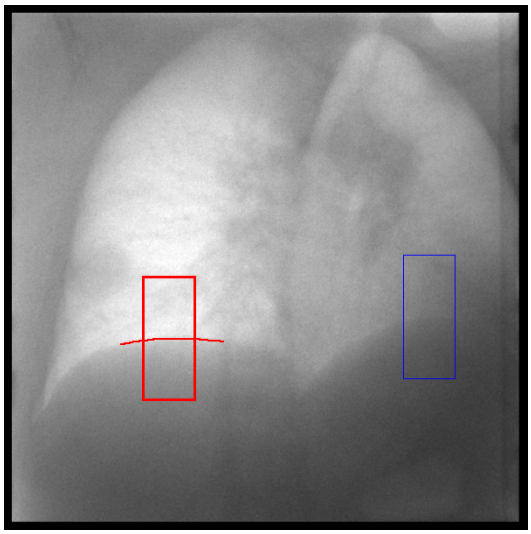

Figure 2-9: An example of IHDA motion detection: The estimated 3D position for each IHDA is projected onto 2D projection image to create ROIs (red and blue rectangle). The double-parabola model is fitted on the hemi-diaphragm (red contour).

Figure 2-9 shows one example of automatic ROI detection and diaphragm detection. Once the 2D positions of the IHDA in all the projection images are determined, the corresponding 3D positions need to be estimated, since the surrogate of the tumor motion is in the 3D IHDA position. Figure 2-10 illustrates the cone beam geometry of this perspective projection. In this figure P_o is the estimated IHDA position, which is derived using the methods presented in sections 2.2 through 2.4. Assume that an angle is projected onto the 2D EPID, parallel to the SI direction (y axis). If we denote the 2D projected location as P_o^{2d}, then the real IHDA position is located nearby to P_o^{2d} and is denoted by P^{2d}, where P is the real 3D IHDA position when this projection image is acquired.

We are interested in knowing the SI direction of P (y in this figure), since it is more clinically significant than the other two directions. Bear in mind that it is impossible to accurately derive the 3D location for P, since it could be located on any point along the ray between the X-ray source S and the detected 2D IHDA P^{2d}. However, since most of

the IHDA motion occurs in the SI direction, the 3D position of P can be estimated by a close point P'. It is the intersection point of the ray $S\text{-}P^{2d}$ and a plane that contains P_o and parallel to the projection image plane.

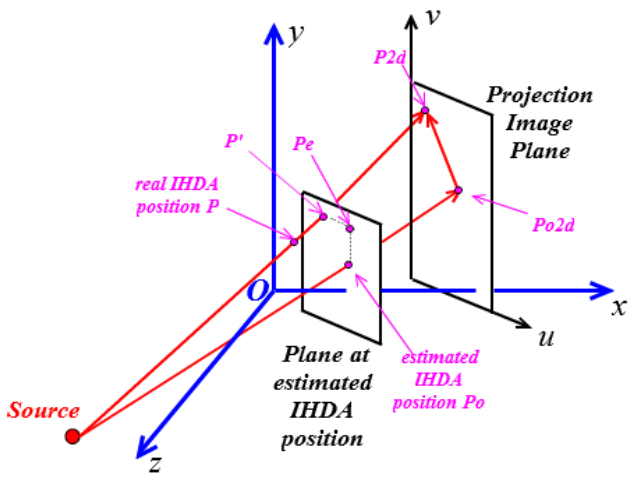

Figure 2-10: An illustration of estimating 3D IHDA position from 2D.

Let's denote $\boldsymbol{P}$ as the 4×3 projection matrix. The perspective projection of a 3D point onto the 2D detector can be represented as $\boldsymbol{P}\cdot P=P^{2d}$. The equation can be further expanded as:

$$P^{2d}u=\frac{P_{11}P_x+P_{12}P_y+P_{13}P_z+P_{14}}{P_{31},Px+P_{32}Py+P_{33}P_z+P_{34}},\ P^{2d}v=\frac{P_{21}P_x+P_{22}P_y+P_{23}P_z+P_{24}}{P_{31},Px+P_{32}Py+P_{33}P_z+P_{34}} \tag{2-20}$$

where u and v are the horizontal and vertical coordinates of the 2D projection plane, respectively. P_{ij} represents the element of the ith row and the jth column of the projection matrix. P_x, P_y, P_z is the 3D coordinate of point P. To derive the estimated SI direction of P'_y, we will consider point P_e, which is located on the same plane as P_o and

P'. It has the same *x* and *z* coordinate as P_o, and same *y* coordinate as *P'*. Based on the relationship of similar triangles, P_e^{2d} (the 2D projection of P_e) would have the same *u* with P_o^{2d} and the same *v* with P^{2d}. Thus P_ey can be derived from the following equations:

$$P^{2d}v = \frac{P_{21}P_{ox} + P_{22}P_{ey} + P_{23}P_{oz} + P_{24}}{P_{31},P_{ox} + P_{32}P_{ey} + P_{33}P_{oz} + P_{34}} \tag{2-21}$$

where only P_ey is unknown. We then use P_{ey} to estimate P_y, which provides close approximation to our goal. It is a very close approximation to P_y. Consider that half of the EPID height h_d is about 20 cm, and SAD equals to 145 cm. The maximal angle between the ray $S\text{-}P^{2d}$ and *x*-*z* plane would be $sin^{-1}(h_d/SAD)$. Typically the lateral motion of the IHDA m_l is less than 0.5 cm (*x* and *z* component of vector P_o-*P*). Thus the largest possible error of the IHDA in the SI direction would be $m_l \cdot h_d/SAD$, which is around 0.07 cm. Compared to a typical motion range of 2 cm, the error is relatively small. Moreover, the diaphragm is usually very close to the iso-center of the cone beam CT during the localization scan, which makes the angle between $S\text{-}P^{2d}$ ray and *x*-*z* plane close to zero. A typical estimation error for the 3D IHDA position would be much smaller.

2.6 Experiments and validation

2.6.1 Results of semi-automatic approach

Figure 2-11 shows the root mean square error (RMS) of 200 projection images for 19 MVCBCT scans of 6 patients. Since the study is taken on the second year of my Ph.D., only MVCBCT scans of 7 patients were derived at that time. Among the 7 patients, the diaphragm of one patient moves out of the imaging region of 2D EPID detector

occasionally, which makes it impossible for IHDA detection. For the other 6 patients, 3~4 scans were selected for each to make the result well balanced among different patients. Overall PDF-based tracking yields better results than DHT. DHT has a significantly large error for image "WB1" and slightly larger error than PDF-based tracking approach in most of the images, due to the confounding contra-lateral hemi-diaphragm in the lateral frames. The overall detection accuracy for probabilistic tracking is *1.228±0.220mm*, compared with DHT *1.341±0.640mm*.

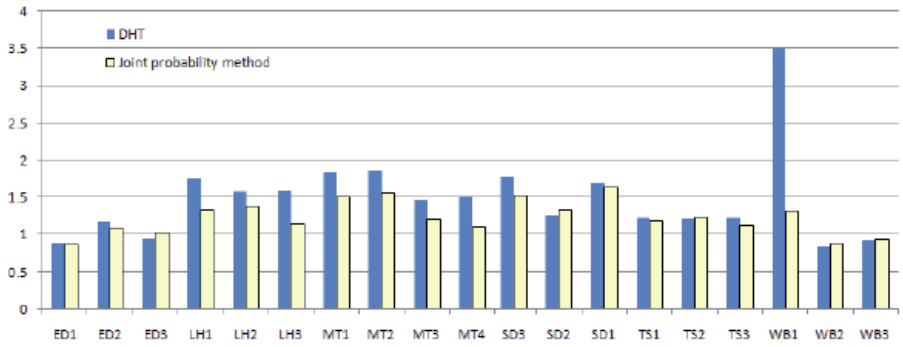

Figure 2-11: Comparison between DHT and probabilistic Hough tracking approach on RMS error (in mm) in 19 MVCBCT scans.

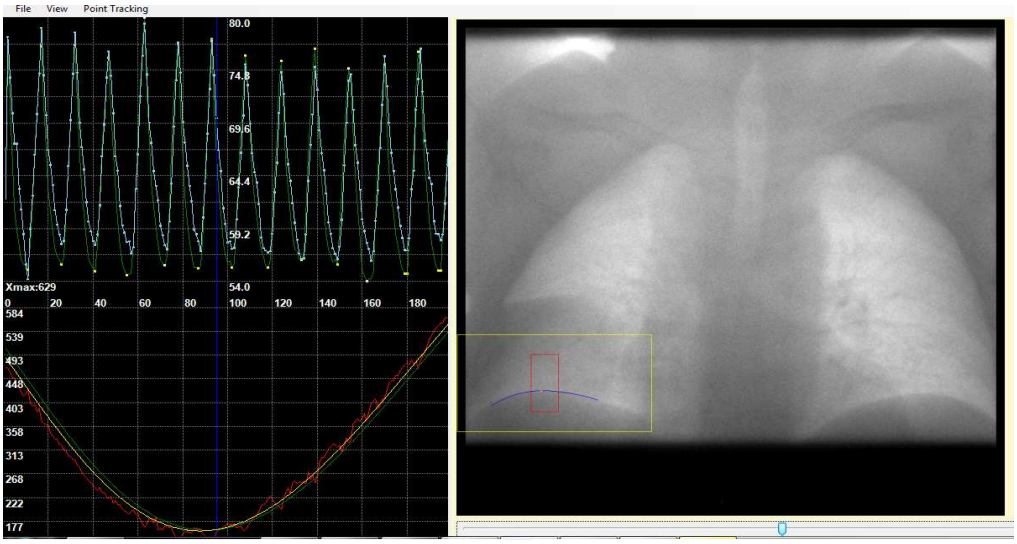

Figure 2-12: A screen layout of the main interface of Just Enough DICOM. The top-left and bottom-left area shows the trajectory of IHDA position in superior-inferior direction and lateral direction respectively. The right area shows the MVCBCT projection image.

2.6.2 Results of fully automatic approach

The fully automatic method was tested 15 patients, all of whom satisfied the need of having images whose diaphragm was within the bottom border of the projection image (Figure 2-13a, b). 4 out of 19 patients were not suitable IHDA detection. Cumulatively 35 MVCBCT localization scans were evaluated. The principle of determining the number of images used for experiment for each patient is as follows: 7 images are selected for each patient. If the number of images available for one patient is less than 7, then use all the images available.

The automatic 3D IHDA localization worked well for 14 of the 15 patients, where the 2D IHDA position was within the ROI created from the projected 3D position. The method worked poorly on one patient, who had a very large tumor attached to the

diaphragm, thereby obstructing it. The missing strong diaphragm gradient caused the detected IHDA position to shift laterally (Figure 2-13c, d).

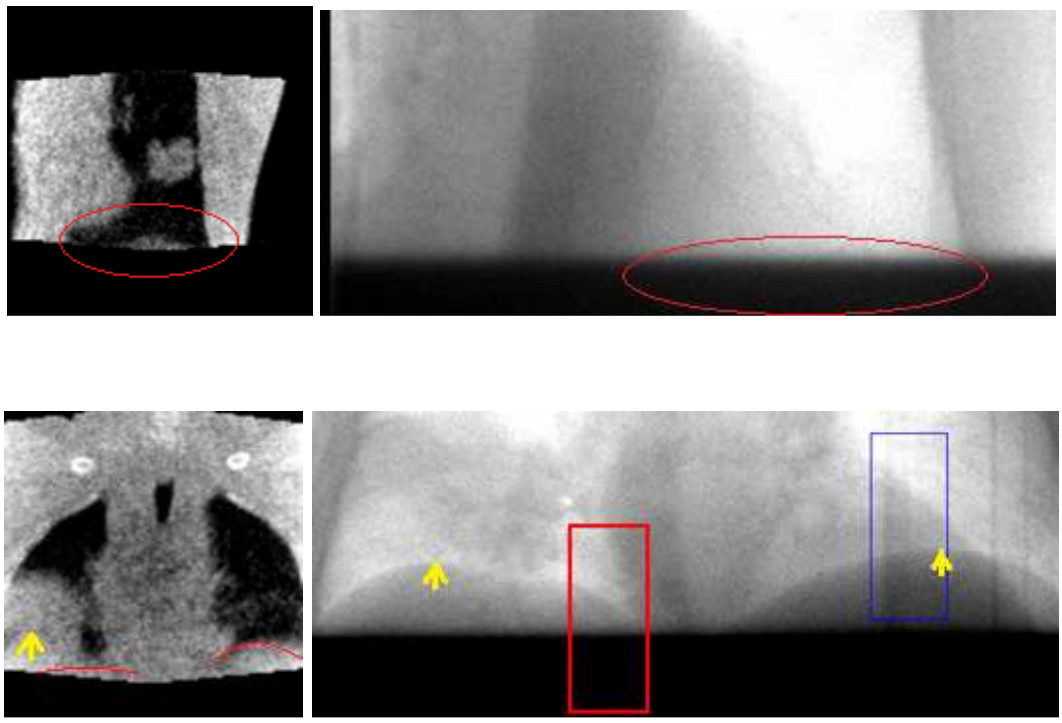

Figure 2-13:Patient data that unsuitable for automatic IHDA detection. (a) A coronal slice of 3D volume and (b) one projection image of one patient whose diaphragm is not visible in the projection image (indicated by the red ellipse). (c) A coronal slice of 3D volume and (d) one projection image of a patient who has a very large tumor attached to the diaphragm of the right lung (appears on the left in both images). No IHDA is found in the first patient. For the second patient the IHDA position (indicated by red ROI and contour) is far from the desired position (yellow arrow). The other detected IHDA is acceptable

To evaluate the detection accuracy the detected IHDA position is compared to those identified manually by a clinician. The error is quantified based on estimated 3D positions in a SI direction, using the method described in section 2.6. Average and standard deviation errors over 200 frames are quantified. The results of the 35 daily

localization scans are shown in Figure 2-14. The IHDA positions were manually identified by two clinicians in three scans (g1, h1, n1) to test the inter-expert variance:

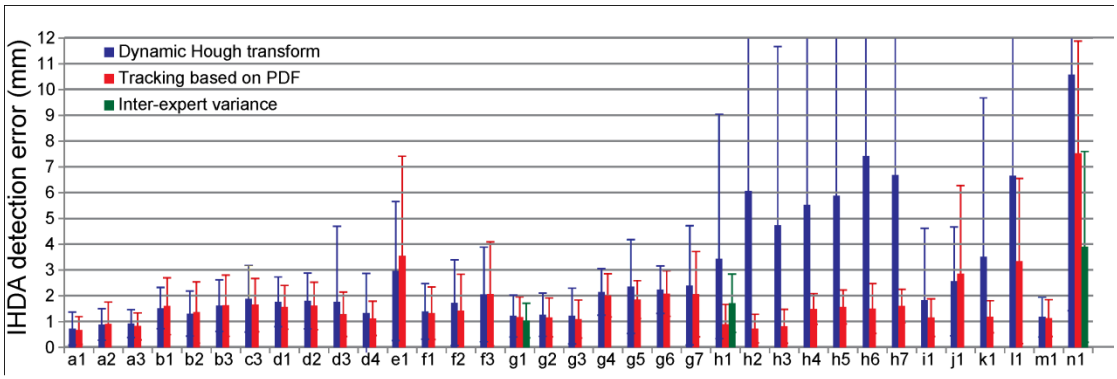

Figure 2-14: The detection accuracy (in *mm*) of 3D IHDA position in SI direction. The average and standard deviation error of 200 projection images are displayed.

The overall average and standard deviations for the 35 scans is 2.933±4.189 *mm* and 1.714±1.544 *mm* for the DHT and tracking based approach, respectively (compared with 19 scans of semi-automatic approach with 1.341±0.640*mm* and 1.228±0.220*mm* for DHT and PDF tracking, respectively). The inter-expert variance is 1.046±0.674 *mm*, 1.715±1.132 *mm* and 3.903±3.700 *mm* for the three scans. Some of the correct IHDA detection examples are shown in Figure 2-15.

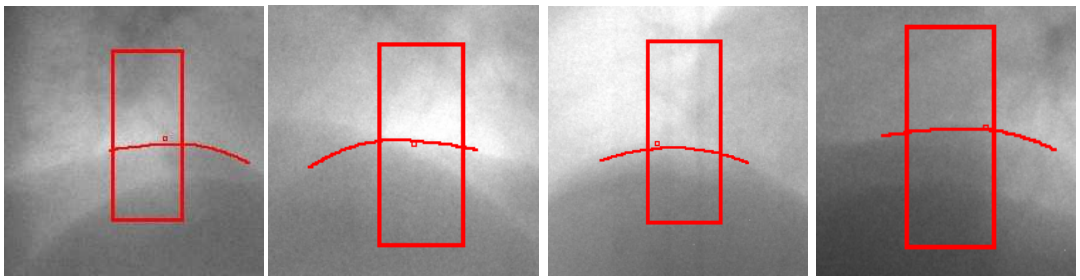

Figure 2-15: Examples of correct IHDA detection. Red rectangle: ROI; Red contour: detected parabola model of diaphragm; Small red point: Expert defined IHDA position

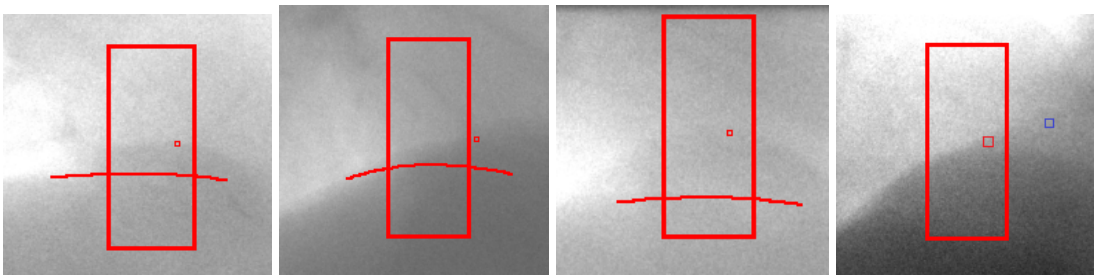

Figure 2-16: Examples of problematic cases: (a, b, c): the detected diaphragm (red contour) is actually the contra-lateral hemi-diaphragm, where the red dot shows the right IHDA position; (d) the variance between two expert identified points (red and blue dots).

2.6.3 IHDA detection error analysis

Generally, the difference in IHDA identification between two sources (either manual identification or automatic detection) can either be due to the smooth transition of the diaphragm boundary or a different interpretation of the IHDA position. The first type of error (type-I) is generally small (within 3 *mm*) and clinically acceptable, since usually a setup error of 5 *mm* is added to the gross tumor volume (GTV) to create a clinical target volume (CTV) for treatment delivery. All the inter-expert variances of g1 and h1 belong to this type. The inter-expert variance from these two patients can be used as reference

for type-I errors, where an automatic detection can be considered as "good" when it is close to this range. The second type of error (type-II), however, needs to be corrected, since at least one of the two sources is not the real IHDA. Instead, it could be an overlapped confounding boundary. For all the scans it is quite common that in some projection angles the contra-lateral hemi-diaphragm (CLHD) is also located in the ROI of the desired hemi-diaphragm and overlaps it. CLHD also creates a strong Hough peak in the Hough accumulation space, confounding the algorithm to make the right choice. Generally, PDF tracking is more robust than DHT in keeping on the right hemi-diaphragm boundary. DHT fails to detect the correct boundary when CLHD has a stronger corresponding Hough accumulation value, which makes the DHT find the globally maximal solution. Based on our observations, the existence of the type-II error, such as those influenced by the CLHD, would make the sum of the average and standard deviation of quantification error larger than 3 *mm.* For the inter-expert variance in n1, there is strong disagreement between the two observers in some frames, illustrated in Figure 2-16d. This is caused by two boundaries that belong to the same lung. The detected diaphragm curve is closer to the red point but not shown here for better visualization purpose.

The performance of the automatic approach on different scans of the same patient does not change much. If accuracy is achieved for one scan, similar accuracy can be expected on other scans of the same patient and vice versa. In Figure 2-14, both patient *g* and *h* have seven scans. The standard deviation of the average IHDA error using the tracking-based approach is 0.466 and 0.395 *mm*, while the standard deviation of all the patients is 0.667 *mm*. One can observe from the 7 scans of patient *h* that the DHT error is significantly larger than the tracking-based approach. For this patient, the detected IHDA by DHT is often attracted by the CLHD when the CLHD moves within the ROI. Figure 2-17a, and b illustrate the detected IHDA trajectory overlaid on a maximal intensity projection (MIP) image of the Hough accumulation array. This MIP image is derived by

projecting the original 3D array $H(x, y, t)$ along x direction to create a new array $H_{MIP}(y, t)$, i.e.

$$H_{MIP}(y,t) = \max_x H(x,y,t) \tag{2-22}$$

The horizontal coordinates of this image are the index of projection images ranging from 1 to 200. The horizontal axis is the vertical direction of the projection plane. It can be seen that the difference of the two detected trajectories are in the first few frames, where the CLHD is located inferior to the correct IHDA and even has a stronger Hough accumulation value.

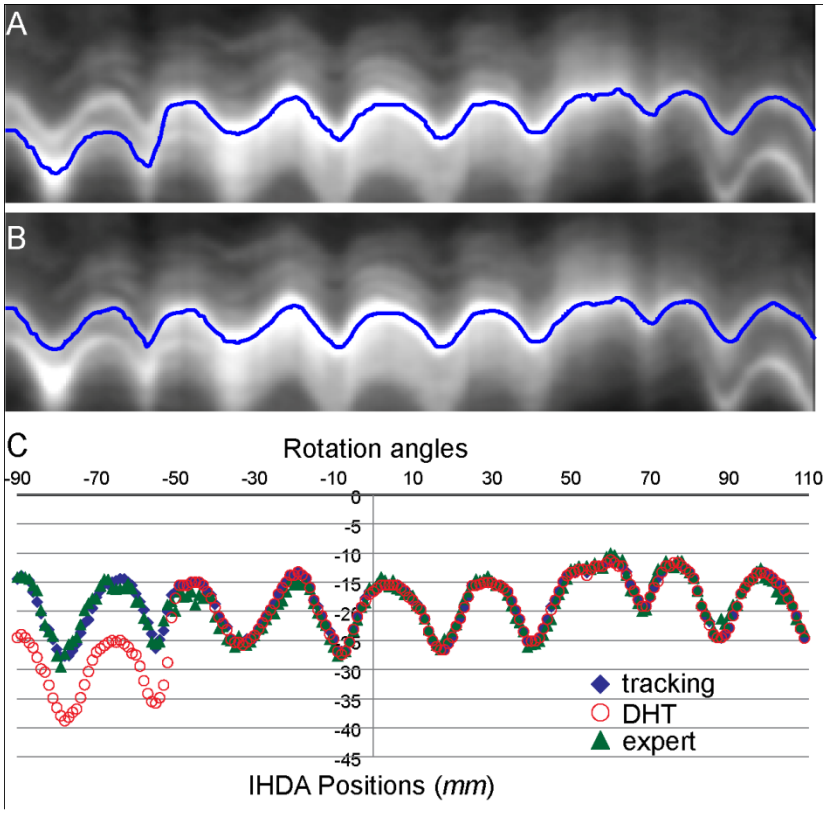

Figure 2-17: The detected contour IHDA position using (a) DHT and (b) tracking-based approach is overlaid on the maximal intensity projection of Hough accumulation array. The 3D IHDA position along SI direction is shown in (c).

Based on our observation, the influence of the CLHD is the major source of error in IHDA detection. Generally the tracking-based approach better avoids erroneous CLHD identification than DHT. However, it is not entirely accurate as can be seen in the scans presented in Figure 2-14. Three different examples of misdetection onto CLHD are shown in Figure 2-16.

Here we will discuss how much accuracy is clinically acceptable for IHDA detection. The amplitude of respiratory motion of IHDA, *D*, will be used to calibrate the strain gauge signal *S* based on the relationship *S=F(D)*, where function *F* is determined by quadratic fitting between the correlation of the two signals. Thus the accuracy of IHDA detection would influence the accuracy of dose distribution on the tumor. The preliminary studies of Siochi et al (Siochi, 2007; Siochi, Kim, & Bhatia, 2008)based on three patients have indicated that a motion of 3mm in excess of planned motion did not have a significant change (<1%) in their tumor control probability (TCP). However, two patients who consistently had 5mm or more motion in excess of planned motion had a drop of 10%. The relationship between diaphragm and tumor motion can be represented by *D=G(T)*, where *D* and *T* is the motion of IHDA and tumor respectively and *G* is assumed to be a linear function. The DTMR is the scale factor in *G*, which plays vital part in determining the accuracy of the gating threshold. We could expand $T=G^{-1}(D)$ into *T=D/k*, where *k* is the DTMR. The error of tumor could further be represented as:

$$\Delta T = \Delta D / k + \Delta k \cdot \frac{D}{k^2} \tag{2-23}$$

Here *ΔT*, *ΔD*, *Δk* can be considered as three random variables with expectation equaling to zero. It can be further assumed that they are normally distributed, with average value equaling to zero and the standard deviation corresponding to the average quantification error of tumor motion amplitude, IHDA motion amplitude and DTMR,

respectively. Based on the rule of addition of two Gaussian functions, the standard deviation of ΔT can be further represented as:

$$\mathrm{var}_{\Delta T} = \sqrt{\mathrm{var}^2{}_{\Delta D}/k^2 + \mathrm{var}^2{}_{\Delta k} \cdot \frac{D^2}{k^4}} \tag{2-24}$$

where *var* represents the standard deviation of each variable indicated by the subscript. Assume that the typical value for k (DTMR) is 1.2. Take 30*mm* as typical diaphragm motion amplitude into the equation. Δk is more or less than 10%, where the details are shown in Chapter 4. For ΔD, take the average error of the fully automatic ROI determination followed by PDF-based tracking, which is 1.714*mm*. This setting of parameters leads to an average error of tumor motion as 2.43*mm*, which satisfies the 3*mm* criterion. Generally, the fully automatic approach provides a worse condition, since the accuracy for semi-automatic approach is even better. Between the two components of ΔD and Δk, Δk has larger contribution to the error. Furthermore, there are some reasons that enable the clinicians further loose the accuracy requirement. First, the manual correction could further reduce ΔD to the order of 1*mm*. Second, the problematic detection has higher probability to be selected as outliers during RANSAC fitting (Chapter 4). Last, a margin will be added to create a planning target volume before treatment delivery, which further reduces for the uncertainties of the tumor motion range. In sum, the semi-automatic framework and the fully-automatic framework based on PDF-tracking approach achieve clinically acceptable accuracy.

2.6.4 Implementation issues

Currently the semi-automatic approach is implemented on "UIHC 4D Verification". It was developed in Microsoft Visual Basic 2010. The major functions used for strain gauge calibration were also implemented in this software, which is currently under clinical trial. The functions include: (1) Manual initialization of IHDA locations on 2 FE frames and 2 FI frames; (2) ROI determination via interpolated ray tracing algorithm; (3) IHDA detection via DHT or PDF-based tracking; (4) RC reconstruction; (5) interactive tumor segmentation via graph cuts; (6) DTMR computation and strain gauge calibration based on random sample consensus (RANSAC). The function (4) to (6) will be further introduced in Chapter 4. Due to the existence of the error, the clinical software should allow manual correction and guidance to the algorithm for the problematic detection. A graphical user interface (GUI) is developed that enables clinicians to manually adjust the IHDA detection. Typically type-II error occurs in several consecutive frames of projection images, this is illustrated in Figure 2-16. Based on this feature, it is suitable to apply the tracking-based approach again, since the IHDA positions in consecutive type-II error frames can be corrected once the clinician has made the adjustment in one frame. In this way the manual correction will not only affect the modified frame, but also affect several neighboring frames. The PDF-based searching starts again using the manually corrected frame as the initial one. The neighboring frames will be searched through and the new detection result will replace the result of the first round. From a wider perspective, though automatic approaches are employed aiming to automate manual identification of IHDA, the software ends up with incorporating the manual correction because the automation sometimes does not do as well. The overall performance in terms of both the accuracy and the running time, however, is significantly improved from using either manual identification or automated process alone. One may

further consider the automatic detection and the manual correction as iterative steps, where this iterative nature is able to take advantage from both sides.

The semi-automatic framework based on "UIHC 4D Verification" was tested on an Intel$^{@}$ Core^{TM} II 2.40 GHZ CPU, 3G RAM desktop computer. The running time of the two Hough-based approaches can generally be divided into four major steps: pre-filtering of the ROI images, Hough transform, Hough peak detection and IHDA motion trajectory detection. Generally, the major bulk of time is in image filtering and the Hough transform. Each of these steps takes about 10~15s. The Hough peak detection and trajectory detection either based on dynamic programming or PDF tracking is relatively quick, which only requires 2~3 seconds in all. The time for manual correction is even quicker, since the Hough array and Hough peak is kept in memory and the correction only requires re-computation of IHDA trajectory in several neighboring frames.

The fully automatic framework is tested on an Intel® Core ™ i7-2620M CPU @2.70GHz laptop with 4GB RAM. The 3D volumetric image reconstruction takes about 8.3 *s*, where all the 200 projection images are reconstructed into a 3D volume containing 128×128×128 voxels, with a voxel spacing of 2 mm. This resolution is sufficient for robust automatic IHDA detection, which takes 4.9 *s* to generate 2D ROIs for each projection image. Compared with our former semi-automatic approach, it takes 30 to 60 *s* for a clinician to manually identify the IHDA position in 4 projection images, depending on his/her familiarity with the software and the visibility of the image. The Hough transform for 200 ROIs takes 6.9 *s*. Once the Hough accumulation array is available, either DHT or tracking-based approach takes less than 0.5 *s* for IHDA detection. The overall computation time is about 20 *s*. The time frame is acceptable for clinical implementation. For comparison, careful manual identification of 200 projection images requires 10 to 20 minutes.

CHAPTER 3
RESPIRATORY MOTION MODEL EXTRACTION DIRECTLY FROM MVCBCT PROJECTION IMAGES

In the last chapter, a framework for detecting IHDA from MVCBCT projection images is presented. A further potential step is to use these projection images to directly monitor or detect intra-fractional motion of other organs, such as the tumor or the lung, since the projection images provide high temporal resolution (about 0.3s). Different approaches have been proposed, including (1) monitoring tumor change by projecting a volume of interest for visualization (Reitz, Gayou, Parda, & Miften, 2008); (2) extracting the 2D/3D position of a projected implanted marker (T. Li et al., 2006) or diaphragm edge (as presented in last chapter); (3) registering from 3D image space to projection space for inter-phase motion compensated reconstruction (T. Li, Koong, & Xing, 2007). Direct tumor tracking or detection in 2D images is mainly focused on fluoroscopy (Shimizu et al., 2001). However, few studies have addressed direct tumor detection in MVCBCT projection images, which suffer from relatively poor contrast due to the energy range of the imaging photons and the interfering anatomies.

In this study, we present a novel method based on an optimal graph search framework to extract 3D respiratory motion models from multiple respiratory phases in 2D projection images. The optimal graph search method, first proposed by Li et al. (K. Li, Wu, Chen, & Sonka, 2006; X. Wu & Chen, 2002) has gained much attention in the field of medical image segmentation in the past few years. The advantage of optimal detection of multiple surfaces has made it widely useful in various image segmentation tasks, such as multiple intra-retinal layer segmentation in optical coherence tomography (OCT) images (Garvin et al., 2008), simultaneous bladder and prostate surface segmentation in

CT images (Song, Wu, Liu, Sonka, & Garvin, 2010), and multiple surface delineation of knee-joint bone and cartilage in MR images (Yin, Zhang, & Sonka, 2008).

The graph search framework was originally designed for multiple-surface segmentation in 3D images. My innovation in this work is to make this graph-based globally optimal method suitable for 3D organ segmentation from 2D image series. An innovative design of graph construction and nodes weight assignment is developed to fulfill this goal, which will be presented in details in upcoming sections. Two major advantages make the proposed method robust in the low-contrast MVCVBCT projection images: (1) The 3D tumor surface segmentation is based on all the 2D projection images that belong to the corresponding respiratory phases. The detection inaccuracies induced by low contrast and interference in one projection image can be reduced. (2) Compared with other 2D-to-3D object shape recovery methods, such as free form deformation (Lotjonen, Magnin, Nenonen, & Katila, 1999), B-spline surface model (Moriyama et al., 2002) and triangulated mesh pulling (Chen et al., 2011), our approach incorporates the maximal allowed motion displacement of the tumor as an inter-surface constraint in the surface detection process and obtains a global optimal solution.

3.1 The motion extraction framework

3.1.1 Overview of the approach

The main steps of the proposed approach are illustrated in Figure 3-1 with the intermediate results for tumor segmentation shown in Figure 3-2. In preparation for the algorithm, the projection images are sorted into several respiratory sorting bins according to the 3D anatomical positions of the ipsi-lateral hemi-diaphragm apex (IHDA), which is automatically extracted from projection images based on the framework introduced in the last chapter. The algorithm starts with an initial 3D static mesh model, which reflects the

approximate topological structure information of the targeted tumor surface. The initial tumor mesh is projected onto each 2D projection image. The new location of mesh points for all the respiratory bins are determined simultaneously using a multi-surface optimal graph search method, which requires computation of the silhouette outline for each projected mesh at first.

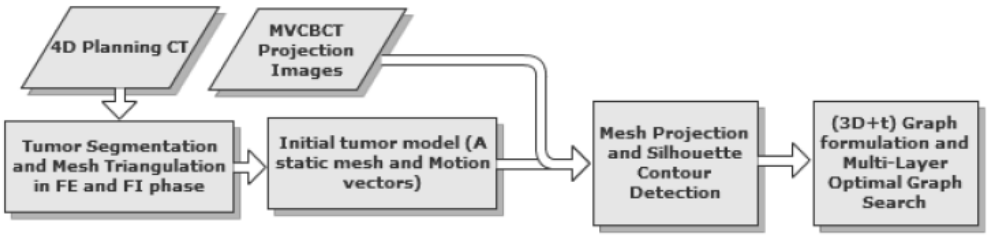

Figure 3-1: Flowchart of the motion extraction approach

3.1.2 Model initialization

The initial static model is the average of the meshes for the full exhale (FE) and full inhale (FI) phases of the 4D CT. For each mesh point, a range of motion is determined using the equation $P_m + \alpha(P_{fe} - P_m)$ and $P_m + \alpha(P_{fi} - P_m)$, where P_{fe} and P_{fi} are the corresponding positions in FE and FI phase, respectively. P_m is the mean position. α is used to control the allowed range, which is typically set between 1.5 and 2.0. The generation of the initial mesh is performed offline during the planning stage and can be completed within 2 minutes.

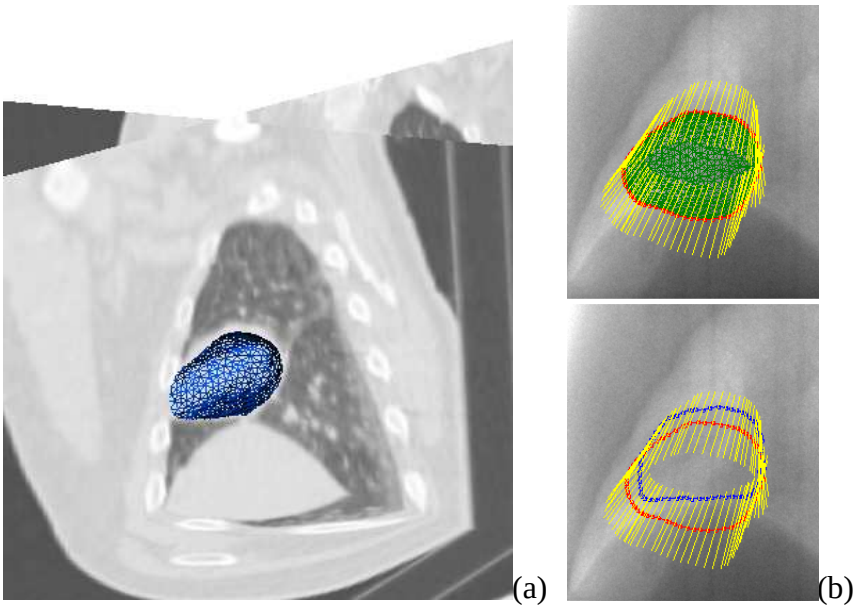

(a) (b)

Figure 3-2: Intermediate steps of the tumor motion extraction approach. (a) Full exhale phase of 4D diagnostic CT volume overlaid with tumor mesh (blue); (b) projected initial static mesh (green), its silhouette contour (red), motion direction (yellow) and the silhouette contour after the graph search computation (blue).

3.1.3 Silhouette contour extraction

The initial static mesh, along with pre-defined motion vectors, is projected onto each 2D projection image. In order to move the mesh towards tumor boundary locations in the projection image, the silhouette outline is extracted from each projected mesh by using an efficient algorithm (Chen et al., 2011), which includes three major steps: (1) select candidate mesh edges (which are potentially silhouette edges) based on local topology of the graph; (2) split intersected candidate edges; (3) follow edges clockwise on the split candidate edges to extract the silhouette outline. The efficiency comes primarily from the first step, where the majority of edges are excluded after the topological analysis. An example of the detected silhouette outline is shown in Figure 3-2.

3.1.4 Multiple surface detection via optimal graph search

A key innovation of the proposed method is converting the segmentation of objects with quasi-periodic motion in 2D rotational cone beam projection images into a 3D multiple interrelated surface detection problem, which can be solved by a graph search framework (K. Li et al., 2006; X. Wu & Chen, 2002). The details are presented as follows. A 4D (3D+t) directed graph $G=(V, E)$ is constructed based on the initial tumor mesh, where V and E are the set for vertices and edges, respectively. The graph contains $N\times M\times T$ nodes, where N and T are the number of points of the static tumor mesh and the number of respiratory bins, respectively. M is the number of sampled points along the pre-defined motion vector. Each combination of $[n,m,t]$ is one unique spatial and temporal location, that represents the mth sampled point in the column defined by mesh point n in phase t. The segmented tumor surfaces are defined by the function $\mathcal{N}:(n,t)\rightarrow \mathcal{N}(n,t)$, where $n\in \mathbf{n}=\{0,\ldots,N-1\}$, $t\in \mathbf{t}=\{0,\ldots,T-1\}$, and $\mathcal{N}(n,t)\in \mathbf{m}=\{0,\ldots,M-1\}$. A cost value is computed for each node $[n,m,t]$, denoted by $c(n,m,t)$, using the following equation:

$$c(n,m,t)=\sum_{p=0}^{P-1}\delta(p,t)\zeta(n,p)w(n,m,p) \tag{3-1}$$

where P and p is the total number and the index of projection images, respectively. The function $\delta(p,t)=1$ when the pth projection image belongs to the tth bin, otherwise it equals zero. The function $\zeta(n,p)=1$ when the nth point in the pth projection image is included in the silhouette contour, otherwise it equals zero. $w(n,m,p)$ is the cost function of the mth sample point in the nth column in the pth projection image, which is defined as:

$$w(n,m,p)=-\overrightarrow{P_p}(\mathbf{normal}(n))\cdot \mathbf{grad}(\overrightarrow{P_p}(\mathbf{P}(n,m)))$$

(3-2)

where $\overrightarrow{P_p}$ is the 3D-to-2D projection operation of a vector or point in the *p*th projection image. ***P****(n,m)* is the location of the *m*th sample point along the pre-defined motion vector of the *n*th mesh point. The operation ***normal***(n) gives the normal direction of the *n*th point of the static mesh, while the operation ***grad*** computes the image gradient of a given 2D location.

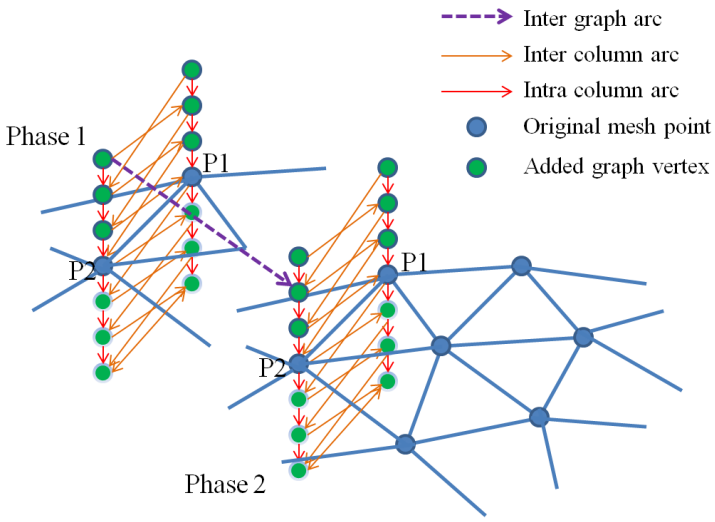

Figure 3-3: A simple illustration of the 4D graph construction

The reason for using the negative dot product between these two vectors is that along the tumor boundary in 2D projection images, the projected normal direction is opposite to the image gradient. Equation (3-1) and (3-2) show that the cost for each node in the 4D graph is determined from all the 2D projection images that belong to the corresponding respiratory bin. Three different types of arcs are added to the graph: (1) **Intra-column arcs** are used to define the graph topology, which connect adjacent nodes that belong to the same column. The arc goes from each node *[n,m,t] (m>0)* to the node below *[n,m-1,t]*. (2) **Inter-column arcs** are used to connect adjacent columns in the same

respiratory bin. The arc goes from each node *[n,m,t] ($m>\delta_m$)* to *[adj(n),m- δ_m,t]*, where *adj(n)* represents adjacent mesh points of *n*. δ_m is the shape smoothness constraint, which is the maximal allowed difference in *m* between adjacent columns of one tumor surface. (3) **Inter-phase arcs** are used to connect the same columns in different respiratory bins. The arc goes from each node *[n,m,t] ($m> \delta_t$)* to *[n,m- δ_t, t±1]* . δ_t is the inter-phase constraint, which is the maximal allowed difference in *m* between adjacent bins of the same column. We define that *[n,m,0]=[n,m,T]* to form a closed loop of respiratory bins.

Figure 3-3 illustrates the main idea for graph construction, where a simple case of *T=2,M=7,* $\delta_m = \delta_t = 1$ is shown. For visualization purposes, only two columns are shown for each bin. And only one inter-phase arc is drawn. The optimal solution can be computed by solving a maximal flow problem in the constructed graph (K. Li et al., 2006).

3.2 Application to the tumor motion extraction

The graph search framework was experimented on both tumor and lung segmentation. In this section the experiment and validation on tumor segmentation is presented. The application to lung motion extraction will be presented in combination to motion-compensated reconstruction in Chapter 5.

Generally, deriving the ground truth of patient tumor shape by using daily localization MVCBCT is very difficult. The standard reconstruction method of MVCBCT uses all the projection images. The tumor is blurred in the 3D volume. Though 4D CT is able to provide clear boundary of tumor volume in multiple phases of 3D volumetric images, the tumor shape, size and motion pattern is likely to change through the course of radiotherapy. To validate the accuracy of the segmentation framework, we have designed and made an imaging phantom. It has a pre-determined size, shape and

motion pattern, which can serve as ground truth. The segmentation result can then be compared with the ground truth.

3.2.1 Phantom design

The imaging phantom consists of two symmetrical blocks of basswood, with a density of about 0.4 g/cc to mimic lung tissue. Each block has six different sized hollow hemispheres measuring 3.81, 3.18, 2.54, 1.91, 0.95, and 0.48*cm* in diameter, respectively. These hollow hemispheres were filled with paraffin wax, with a density of about 0.93 g/cc to mimic lung tumors. The two halves were carefully aligned to form a rectangular box embedded with six spherical pieces of paraffin wax. Figure 3-4 shows a picture of the phantom, a coronal slice of a diagnostic CT and a MVCBCT projection image, respectively. It can be seen that all the six spherical inserts have clear boundaries in the diagnostic CT slice, while it is hard to observe the two smallest inserts in the MVCBCT projection images.

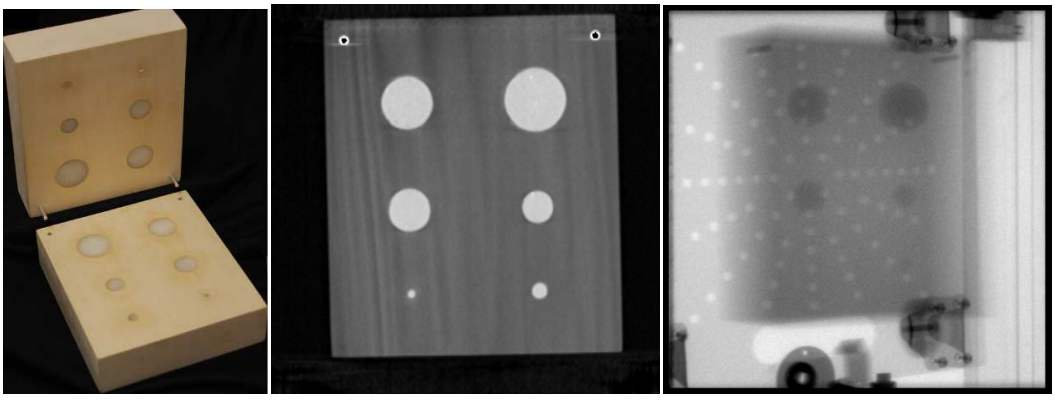

Figure 3-4: A picture of Left: the imaging phantom; Middle: a coronal slice of one phase of the 4D diagnostic CT; Right: one projection image of MVCBCT with a dose of 10MU

The imaging phantom is placed on a cart attached to the Quasar respiratory motion (QRM) phantom (Modus Medical Devices, INC, London, ON, Canada) to simulate respiratory motion. The QRM phantom is programmed to move only in the superior-inferior (SI) direction, with its position, as a function of time *t*, defined as

$$z(t) = z_0 + A_0 \cos^4(\pi(t + t_0)/\tau) \tag{3-3}$$

where the motion amplitude A_0 is 30 mm, and the period τ is 4s to represent typical breathing. z_0 and t_0 are the DC component of the motion and the starting phase of the phantom motion, which varies among different experiments. The phantom tests were done on two scans, with a dose of 5MU and 10MU, respectively. The imaging phantom experiment was not only used in the tumor segmentation verification introduced in this chapter, but also used for validation of correlated reconstruction presented in Chapter 4 and validation for projection image enhancement technique introduced in chapter 6.

3.2.2 Validation result

The graph-based segmentation framework was also tested on 12 scans from three patients. Among all the 19 patients, the selected three patients have relatively large tumors in the lower lobe of the lung, which can be identified directly by human eye in the projection images. In this way the tumor segmentation can be compared with manual contour in the projection images. 3 images were selected for each of the previous two patients. 6 images were selected for the third patient, since an additional 4D CT was taken in the middle of the course of radiotherapy for this patient, which can be used to create the prior geometric tumor model for more following MVCBCT scans. All the patient scans used an imaging dose of 10MU.

Figure 3-5 shows the detection result of the largest spherical insert of the phantom (top) and a real patient whose tumor is right above the diaphragm (bottom). The top-right corner shows the detected 3D mesh in the corresponding respiratory bin. The evaluation is based on 2D contours in projection space. For the phantom images, the detected contour of the inserts is compared with the contour computed from the predefined size and the motion, which is considered ground truth. It can be seen that the insert can be detected robustly in the presence of the interfering superimposed objects, such as interfering spheres (Figure 3-5-1), the QRM motion phantom (Figure 3-5-2) and the holes of the plastic support (small white circles in Figure 3-5-3 and Figure 3-5-4).

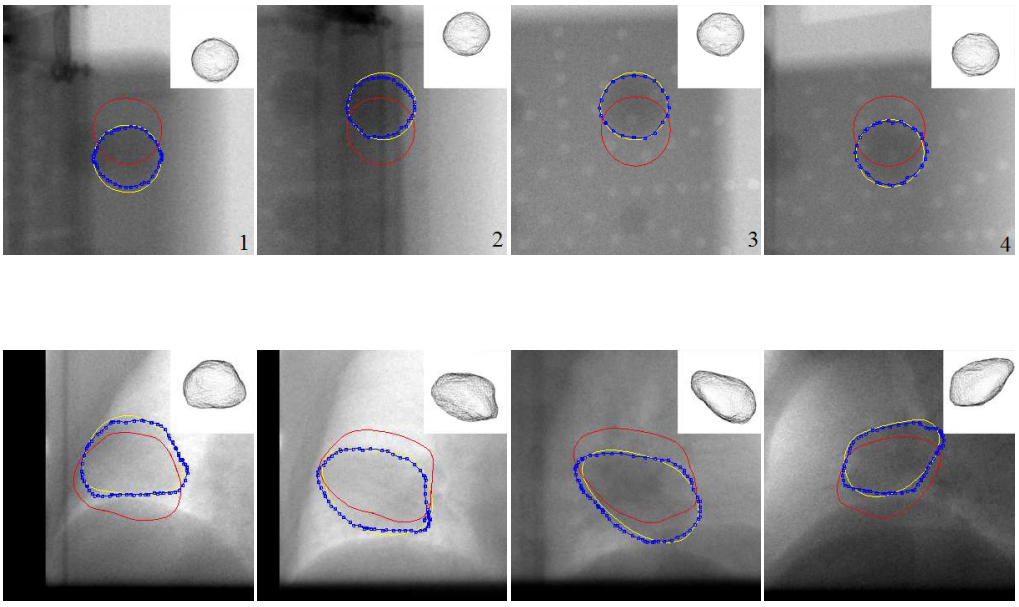

Figure 3-5: Detection result on Top row: the imaging phantom; Bottom row: a patient with tumor above the diaphragm. Red: silhouette outline of initial mesh; blue: detected tumor contour (deformed silhouette outline); yellow: contour of ground truth for phantom images, manually annotated contour for patient images. The detected 3D tumor mesh of the corresponding respiratory bin is displayed on the top-right corner.

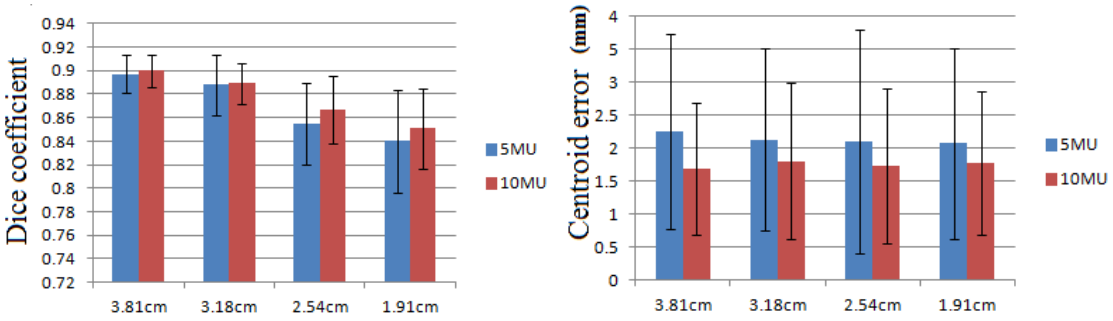

Figure 3-6: Mean and standard deviation of **Left**: dice coefficient between detected contour and ground truth; **Right**: centroid difference between detected contour and ground truth over 200 projection images of four spherical inserts.

The evaluation is based on the four largest inserts, since there is no strong boundary information of the two smaller ones in the MVCBCT projection images (Figure 3-4). Two metrics were employed to validate the detection result: The 2D dice coefficient and the difference of centroid positions along the SI direction.

Figure 3-6 shows the mean and standard deviation values of those metrics over 200 projection images for the four largest inserts tested. It can be seen that the dice coefficient decreases slightly when the tumor size goes down, while this phenomenon does not occur in the centroid error. An imaging dose of 10 MU obtains better accuracy for centroid localization and a slight improvement in the dice coefficient. For patient images, the tumor was independently contoured by two clinical experts. The average contour was computed to compare with the detection result. The difference between the two manual contours is also quantified.

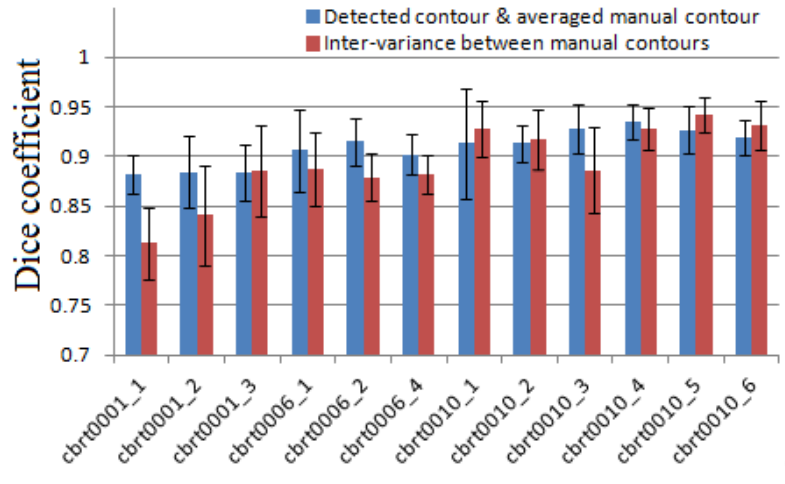

(a)

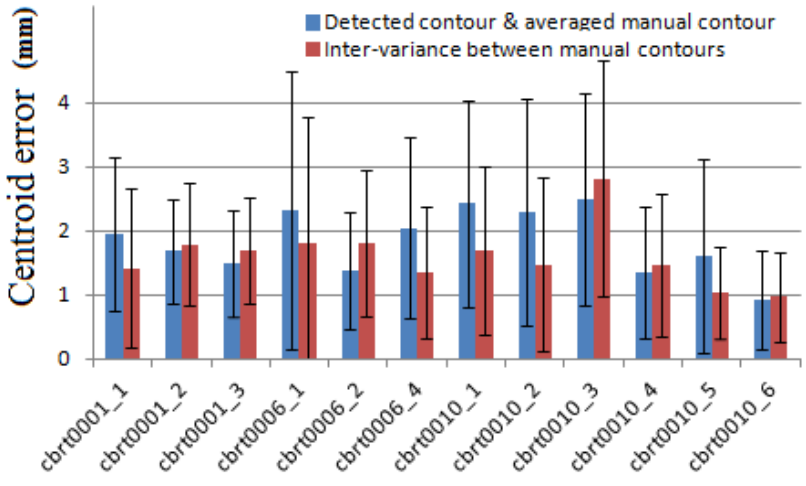

(b)

Figure 3-7: Mean and standard deviation of **(a)** dice coefficient; **(b)** centroid difference over 200 projection images of 12 MVCBT scans of patients.

Figure 3-7 shows the dice coefficient and centroid difference over 12 MVCBCT scans from 3 patients, where it can be seen that the overall dice coefficient of the proposed method is even better than variations between manual contours. This result is expected, since the detection incorporates motion constraints as well as information from multiple images that belong to the same corresponding bin, while the manual contour is

based solely on one projection image, which contains several confounding objects generated by the projection of other tissues.

On average, the phantom study obtained a dice coefficient of 0.87±0.03 and a centroid error of 1.94±1.31*mm*. Results based on 12 MVCBCT scans from 3 patients obtained 0.91±0.03 for dice coefficient and 1.83±1.31*mm* for centroid error, compared with a difference between two sets of independent manual contours of 0.89±0.03 and 1.61±1.19*mm*, respectively. As discussed in the last chapter, based on a study of three patients, a motion of 3mm in excess of planned motion did not have a significant change (<1%) in their tumor control probability (TCP) (Siochi et al., 2008). Moreover, a setup error of 5*mm* is typically added to the gross tumor volume (GTV) for treatment delivery. For both phantom and patient studies, the quantified centroid accuracy is generally acceptable within the clinical requirement.

CHAPTER 4

BIMODAL MVCBCT VIA CORRELATED RECONSTRUCTION

In the previous chapters, we have shown the advances in MVCBCT imaging, which have made it clinically possible to perform patient localization prior to each treatment by registering the treatment CT to the planning CT. This process uses the treatment beam from a linear accelerator (linac) and an electronic portal imaging device (EPID) to capture projection images as the gantry rotates. These projection images are used for reconstruction by default. They could also be used in cine mode, where they could be exported into DICOM format for visualization and analysis. In Chapter 3, we have shown the feasibility of using MVCBCT projection images to identify tumor positions. The tumor motion amplitude could be further used to calibrate the strain gauge. However, as we have also presented in Chapter 3, the direct tumor segmentation framework is currently only suitable for large tumors. The method is not robust enough to capture the motion of small tumors, since the contrast in most of the projection images is low and the tumor boundary is poorly defined (see Figure 3-4). Tracking techniques that have been successfully applied to fluoroscopic images, such as methods based on template matching (Cui et al., 2007) or optical flow (Q. Xu et al., 2008) may not be robust enough for MVCBCT projection images as well.

An alternative approach may be to use the diaphragm motion since it correlates well with tumor motion for most lung cancer patients (Cervino et al., 2009). In a preliminary study conducted by Dr. Siochi(Siochi, 2007), he identified the IHDA and the superior edge of the tumor in MVCBCT projections from 27 treatment fractions of one non-small-cell lung cancer (NSCLC) patient. The tumor position correlates well with the IHDA position in these projection images, with an averaged coefficient of determination of 0.95 for the linear fit. Moreover, the diaphragm edge between air and tissue is clearly

visible in the projection images. Methods presented in Chapter 2 have been able to detect 2D IHDA positions in MVCBCT projection images semi-automatically, and convert them to 3D room coordinates using an interpolated ray tracing algorithm (Siochi, 2009). However, performing the same task for the tumor is more difficult.

One could use the MVCBCT images to quantify the relationship between tumor and diaphragm motion. Applying respiratory correlated (RC) reconstruction by retrospectively sorting all the projection data according to diaphragm position would reduce blurring significantly, enabling clinicians to identify tumor and diaphragm boundaries directly on the images. We can then derive the diaphragm-to-tumor motion ratio (DTMR), which is based on the tumor centroid displacement and the IHDA displacement between full exhale (FE) and full inhale (FI) CBCT images. The strain gauge signal could be calibrated for tumor motion by using the DTMR and correlating the IHDA positions with the corresponding strain gauge signal recorded for each projection image.

This chapter will be divided into three sections. The first section will show the feasibility of quantifying DTMR and tumor volume changes for a large tumor by using RC MVCBCT. However, RC MVCBCT based on one scan has many missing projection images; this causes severe view aliasing artifacts and degrades the reconstructed image quality, potentially limiting its applicability to larger tumors and small displacements. Section two describes the phantom tests that are carried to quantify the inaccuracies brought by the image degradation. It should be noted that the patient images could not provide ground truth for tumor size, shape or motion amplitude. At best, one can only hope to establish agreement among multiple dynamic imaging modalities such as Cine-MR and 4DCT. Hence, in order to quantify the errors in volume and motion determination, a phantom with spherical inserts was imaged to study the feasibility of using RC MVCBCT to quantify tumor motion and tumor volumes. The actual motion of the phantom and the size of the inserts are known and serve as ground truth. The last

section will present our current methods that were implemented in the clinical software "UIHC 4D verification", which is currently under clinical trial for strain gauge calibration based on correlated bimodal MVCBCT.

4.1 Patient studies

Current MVCBCT imaging uses all the projections to reconstruct a static image. By selecting projections belonging to the same respiratory phase, it is possible to reconstruct MVCBCT images of moving tumors with multiple phases. In this study the FE and FI phases are reconstructed for each MVCBCT scan. The superior-inferior position of the IHDA, provided by the previous step, is scaled from 0 to 100 to represent normalized respiratory phases. The ideal phase bin for the FE phase should be 0 to *pw*, and (*100−pw*) to 100 for the FI phase, where *pw* stands for the window size of the phase bin. But for real respiratory traces, especially for irregular breathing, inclusion of 0 or 100 will only encompass a small amount of projections. Both factors should be considered for proper phase window and level values. An exhaustive search strategy is applied to find these values. For the FI phase, it aims to find a phase window and level that maximize the averaged respiratory amplitude of projections within the phase window. For the FE phase, the same procedure is used for minimization of the amplitude.

The default CBCT reconstruction algorithm by Feldkamp, Davis, and Kress (FDK)(Feldkamp et al., 1984), is fast and produces good images, but an inadequate number of projections results in strong aliasing artifacts. Algorithms derived from Algebraic reconstruction techniques (ART)(Gordon, Bender, & Herman, 1970) are more robust for incomplete projections but require much more computation time due to iterative re-projection and backprojection (Mueller, Yagel, & Wheller, 1999a). Hardware

acceleration based on graphics cards made it feasible to accomplish cone beam ART reconstruction within a clinical time limit (Mueller, Yagel, & Wheller, 1999b).

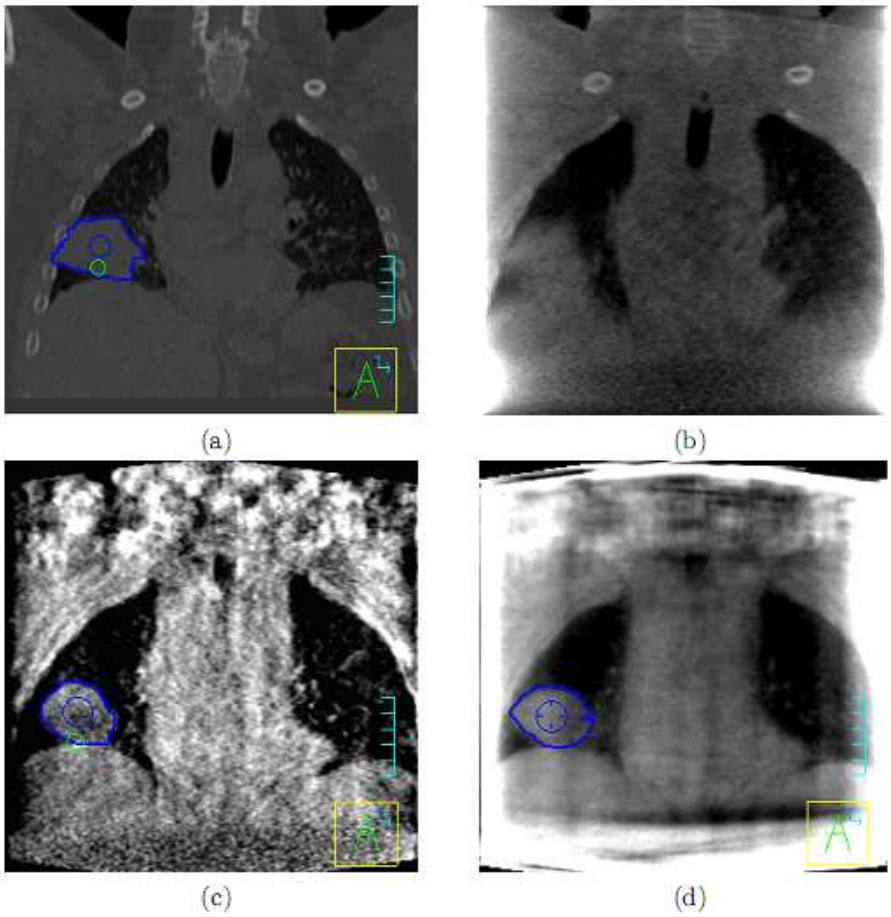

Figure 4-1: Image reconstruction example slice in coronal view: (a) FE phase of planning CT; (b) MVCBCT reconstructed from all the projections; (c) FE phase of RC MVCBCT reconstructed by FDK algorithm; (d) FE phase of RC MVCBCT reconstructed by ART algorithm (tumor contour is displayed in blue

We have tested both methods to investigate the feasibility of tumor contouring without considering reconstruction speed. The projection matrices of MVCBCT, which were derived during MVCBCT geometric calibration (Morin et al., 2006), are used for voxel-driven computations in FDK method and ray-driven models in ART (Galigekere,

Wiesent, & Holdsworth, 2003). A Bessel-Kraiser filter (Lewitt, 1990) is used as the interpolation kernel for ART, since it has less aliasing artifacts than bilinear or Gaussian kernels for ray-driven back-projection.

The IHDA position and tumor boundary in both FE and FI images are identified by a researcher without prior knowledge of the patient using the Pinnacle treatment planning software. The volume and centroid of the tumor and the DTMR are then calculated. These parameters are also quantified on the planning CT for comparison. Figure 4-1 shows one example of manual contouring of the tumor using Pinnacle. The figure is the same as Figure 1-3. It is displayed again here for convenient purpose.

Figure 4-1a shows one coronal slice of a 4D planning CT. The MVCBCT has a much lower contrast to noise ratio (CNR). In Figure 4-1b a MVCBCT image reconstructed using all the projection data is shown. Static tissues such as shoulders are visible, but objects in motion, such as ribs, hemi-diaphragms and the tumor are very blurred. In the example image of the respiratory sorted reconstruction, the tumor boundary and diaphragm are better defined, regardless of the reconstruction method: FDK (Figure 4-1c) or ART (Figure 4-1d). Reconstruction artifacts existed in both FDK-MVCBCT and ART-MVCBCT, further degrading the image quality. Both FDK and ART have truncation artifacts at the border of the imaging FOV. The intensities of organs outside the FOV contribute to the voxel at the FOV border during back-projection. For FDK, the streak artifact is observable, which is due to incomplete projections. The patient received audio-coaching during the treatment in order to encourage regular breathing. While this makes the gated RT treatment more reliable, it can also help improve the reconstruction of limited projection data by avoiding large gaps of missing projections. However there are some exceptions when the patient is unable to maintain the regularity during the scan. In our study, the IHDA respiratory phase in one of 16 MVCBCT images shows a very irregular pattern (Figure 4-2a), where the respiratory amplitudes for some maxima are much smaller than those of the other maxima. The exhaustive search strategy

had a hard time for this image, since no projections are within the FI phase window from frame 60 to 160 (Figure 4-2a). The image reconstructed in this projection set is severely degraded, making it impossible to contour the tumor correctly. For reference, Figure 4-2b shows a regular breathing pattern.

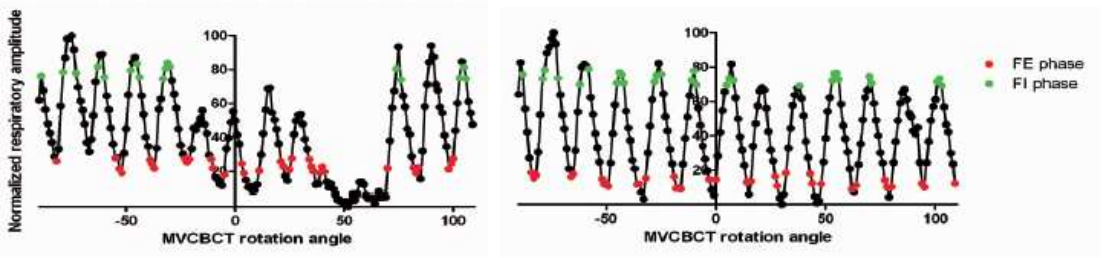

Figure 4-2: Normalized respiratory phase for **Left**: irregular breath; **Right**: regular breath.

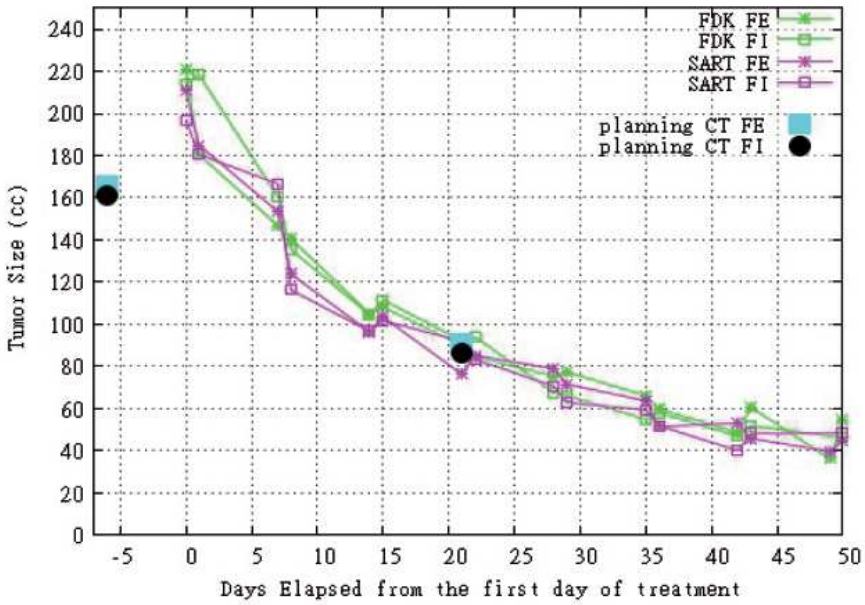

Figure 4-3: Tumor volume plotted against elapsed days from first fraction

The radiation effect on tumor volume over the course of radiotherapy is plotted in Figure 4-3. Images reconstructed by FDK and ART are both studied. The effect of radiotherapy shows an exponential pattern of volume shrinkage. The average discrepancy in tumor volume between FDK and ART methods is 9.38%, with a standard deviation of 7.2%. The discrepancy between the two methods may be due to human subjective error and improper setting of display window and level, which is shown to affect the object size measurement (Baxter & Sorenson, 1981). Although small errors existed between FDK and ART in size measurement, both methods agree well for the purpose of monitoring the trend of tumor change. Tumor volumes derived from two 4D planning CT scans are also shown in the graph, which can be considered as a gold standard. For the planning CT taken 6 days before the start of radiotherapy treatments, the tumor size is much smaller than the tumor size in both FDK-MVCBCT and ART-MVCBCT images taken minutes before the first radiation treatment. This may be due to tumor growth during the 6 day interim between imaging and treatment, since there is no radiation given during the 6 day interim and the tumor was particularly aggressive. The tumor size contoured in the second planning CT agrees well with the MVCBCT taken on the same day.

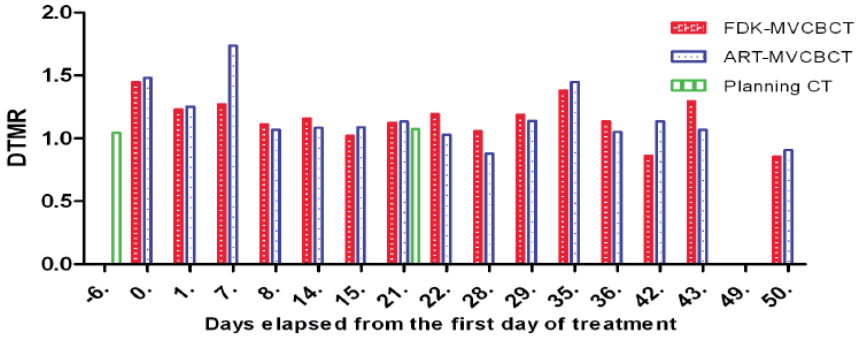

Figure 4-4: DTMR value for 15 MVCBCT and 2 planning CT (MVCBCT with irregular breathing is excluded).

DTMR values are plotted in Figure 4-4. DTMR is computed from the IHDA motion and tumor motion, which is displayed in Figure 4-5. The measured motion is generally consistent between FDK-MVCBCT and ART-MVCBCT. The measured IHDA motion ranges from 0.78cm to 2.17cm, with an average and standard deviation of the difference between FDK and SART methods of 0.058cm ± 0.052cm. The tumor motion ranges from 0.8cm to 1.82cm, with a deviation between the two methods of 0.131cm±0.112cm.

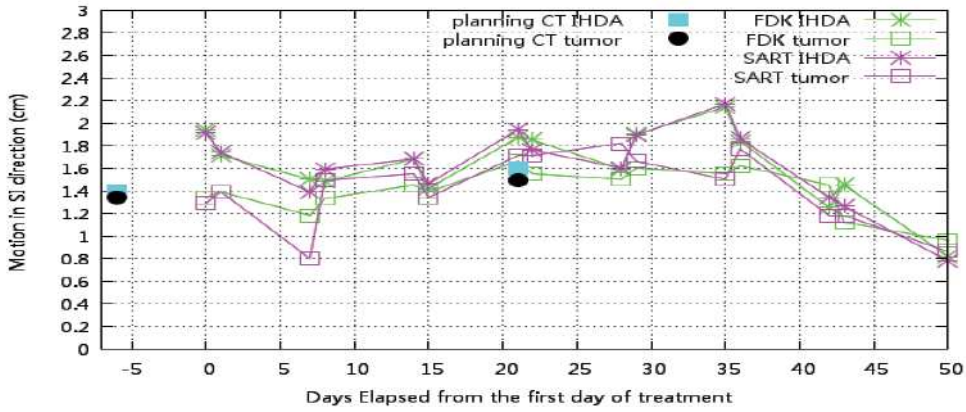

Figure 4-5: Motion of IHDA and tumor centroid for 15 MVCBCT and 2 planning CT (MVCBCT with irregular breathing is excluded).

Comparing tumor and IHDA motion to the slice thickness in the superior-inferior direction, which is 1.071mm and 3.0mm for the MVCBCT and 4DCT respectively, variation by one voxel in the IHDA identification may induce a 10% DTMR change. This error is consistent with the average difference between FDK and ART measurements. There are a few cases with a significant exception such as the one on day 7. The motion of both the IHDA and the tumor centroid in this scan is relatively small. The division between the two measured motions to compute the DTMR further increases the inaccuracy, which is part of the reason for the larger error. DTMR from the planning

4DCT taken 6 days before the first treatment day is much smaller than that of the MVCBCT, possibly due to discrepancies in tumor volume and/or natural variations in breathing patterns from one day to the next. For the planning 4D CT taken on the 4th week, the DTMR is close to that of the MVCBCT. Typically most images have a DTMR larger than 1, which is consistent with lung expansion during inhale. For the few cases where DTMR is smaller than 1, they may be due to manual identification and contouring errors, but it is also possible that the patient was breathing more with their chest than with their diaphragm.

To sum up, we have verified the feasibility of assessing tumor response based on respiratory sorted MVCBCT derived tumor volumes. Parameters measured for the tumor contour and the IHDA in MVCBCT images are close to those of the planning CT and are in a reasonable range, except for a few cases in the first week of the MVCBCT, probably due to the time delay between 4DCT imaging and the first treatment fraction. The comparison of the DTMR for planning CT data and MVCBCT data also shows that it is feasible to use limited projection reconstruction to determine the tumor and diaphragm motion relationship. Generally, the validation work presented in this section shows the feasibility of observing trends in tumor size changes and measuring the DTMR to establish a relationship between tumor and diaphragm motion. Reconstruction artifacts induced by incomplete projections and truncations are the main reasons that affect tumor contour accuracy. The accuracy of using respiratory sorted MVCBCT reconstruction to measure object size and motion still needs to be assessed. It will be very helpful to image an object with prior knowledge about its density, shape and size, in order to quantify the reconstruction error. The next section will focus on the quantification of the reconstruction accuracy.

4.2 Phantom studies

The details of the phantom design and the predefined motion can be seen in section 3.2.1. It is not only used for validation of the segmentation framework introduced in Chapter 3, but also used for validation for the correlated reconstruction approach presented in this chapter. The respiratory signal is based on the cranio-caudal motion of the center of the spherical insert. It is automatically rescaled into a relative motion range from 0 to 100, which corresponds to the most superior and the most inferior positions, respectively. This is similar to patient studies, where the rescaling is applied to the motion of the IHDA. 3D images at FE (0%) and FI (100%) are sufficient to quantify "tumor" displacement between full exhale and inhale states. Projection images are sorted to those two respiratory states with a fixed amplitude interval. The size of the allowed amplitude interval is a compromise between view aliasing artifacts (the reduction of which requires more projections) and residual motion (the reduction of which requires fewer projections). The interval is set at 10%, which corresponds to 3.0 mm in our study. Hence, the FE image is reconstructed from projections with sphere positions of approximately 0 to 3 mm from full exhale position. For the FI image, the selected projections have sphere positions of approximately 27 to 30 mm inferior to the full exhale position. For a CBCT scan that acquires 200 projections of a phantom that moves according to Figure 2-3, about 70 projections are included in the FE phase, while about 30 belong to the FI phase.

Image reconstruction was performed using the Feldkamp, Davis, Kress (FDK) method (Feldkamp et al., 1984). For the MVCBCT imaging of a static phantom, a clinical FDK reconstruction system is used. The dimension of the 3D volumetric image is 256 × 256 × 274 (274 is in the craniocaudal direction), with a voxel spacing of 1.0 mm. For imaging of the moving phantom, an offline FDK algorithm is developed for the RC reconstruction. (The offline application uses the same algorithm as the online version, but

it is used to reduce demand for the clinical imaging workstation that performs the online reconstruction.) The sorted projections are reconstructed into an image of 256×256×256, with a voxel spacing of 1.071 mm. The dimension of each 3D image for the 4DCT scan is 512×512×274 (274 in the craniocaudal direction), with a transverse slice thickness of 1.0 mm.

The commercially available product of MVCBCT uses a 6 MV treatment beam line (TBL), while a test system in our clinic uses a 4.2 MeV imaging beam line (IBL). The lower energy photons provide a better quality image for the same dose (Faddegon et al., 2008; Faddegon et al., 2010; Flynn et al., 2009), allowing us to determine if RC MVCBCT benefits from the new beam line. For both TBL and IBL modes, the standard protocols use a 200° arc from -90° to 110°, generating one projection image per degree. We also tested a TBL protocol with a full rotation (359° arc), so that we can evaluate whether the increased number of projections improves our ability to determine tumor sizes and motion from RC MVCBCT.

We acquired 12 scans, six with the phantom at rest and six with the phantom in motion. The six scans used the three modes (200° IBL, 200° TBL, 359° TBL) at 5 and 10 MU. The phantom was also scanned at rest and in motion using 4D kVCT to compare our RC MVCBCT results against a clinical 4D system. All the 3D MVCBCT and kV CT volumetric images were stored in DICOM format and imported into the Philips Pinnacle (Philips Medical Systems, Andover, MA) treatment planning system. All spherical inserts in all the images were contoured. The volume and center of the contoured regions of interest were derived using Pinnacle's measurement tools. The displacements between volumes in the FE and FI images were computed from the difference of the centroid positions.

Previous studies have demonstrated that the display window center (WC) and window width (WW) significantly influence the apparent size of an object in CT imaging (Baxter & Sorenson, 1981; Magnusson, 1987). It was found that the WC should be half

of the attenuation differences between the object and the background in order to yield the correct size. In this study, we set the WC at half of the attenuation difference between the spherical insert and the basswood frame. The WW is set as the attenuation difference.

4.2.1 Image quality

Figure 4-6 shows one coronal slice of the FE phase for kVCT and RC MVCBCT imaging for different protocols. Figure 4-7 compares the attenuation profiles of those images for the largest two spherical inserts. For the kVCT, the image intensity is distributed uniformly within each spherical insert and the CT number represents the material density well. For the other three RC MVCBCT images, the image intensity is no longer uniformly distributed, as noise occurs in both wax and basswood regions. There is some difference between the CT number in the RC MVCBCT and the CT number that corresponds to the actual density of the material. As expected, the uniformity within the sphere improves as the dose is increased from 5 to 10 MU (from upper right to lower left panel), and as one goes to a softer energy spectrum (from lower left, TBL, to lower right, IBL). The smallest insert is identifiable in images reconstructed using IBL or images reconstructed from 359 projections. Using a wider range of projections and IBL improves the imaging quality.

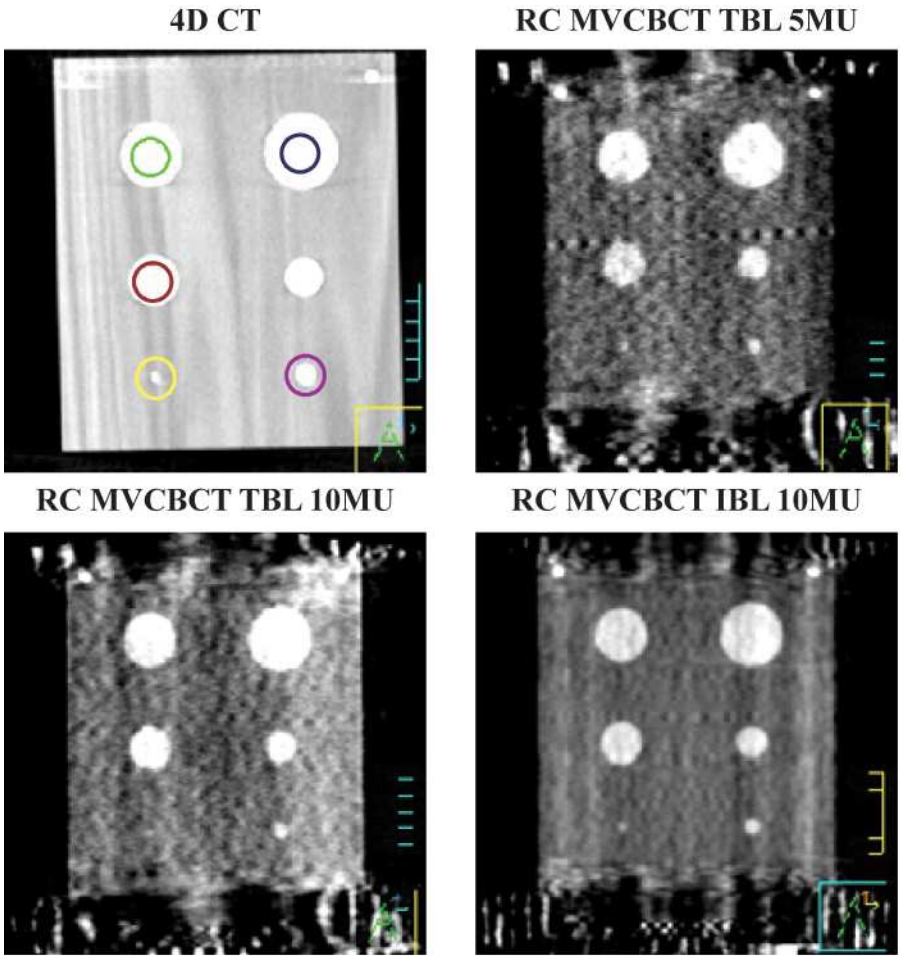

Figure 4-6: One coronal slice of the phantom imaged using kVCT (top-left), RC MVCBCT with 5 MU TBL (top-right), RC MVCBCT with 10 MU TBL (bottom-left), and RC MVCBCT with 10 MU IBL (bottom-right).

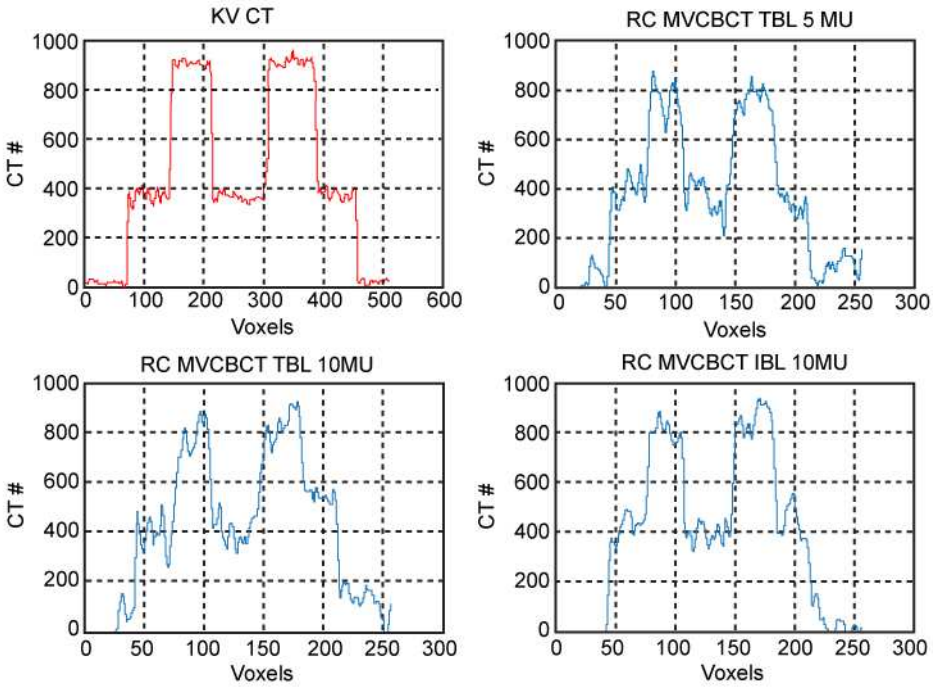

Figure 4-7: Imaging profile of the two largest inserts in FE phase images using kVCT (top-left), RC MVCBCT with 5 MU TBL (top-right), RC MVCBCT with 10 MU TBL (bottom-left), and RC MVCBCT with 10 MU IBL (bottom-right).

4.2.2 Volume quantification

We use the relative error to measure the accuracy of volume determination. The relative error is defined as the normalized difference with the nominal designed value:

$$relative\ error = \left| V_{actual} - V_{designed} \right| / V_{designed} \tag{4-1}$$

where V_{actual} is the volume measured from the contours and $V_{designed}$ is the nominal designed volume.

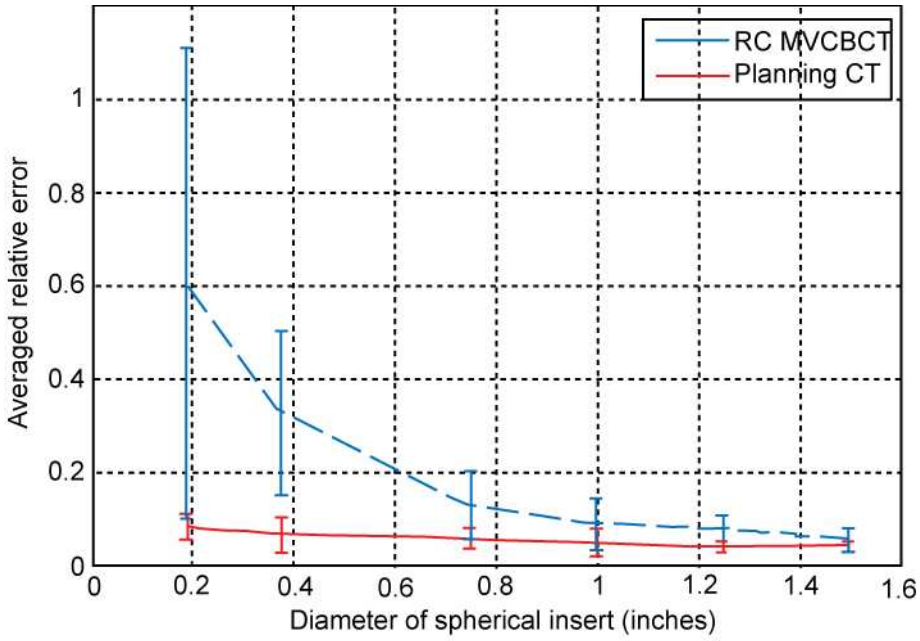

Figure 4-8: Relative error in volume as a function of the phantom insert diameter.

Figure 4-8 compares the average and standard deviation of the relative error in volume for all the kVCT images and RC MVCBCT images. For the planning CT, the error is within 10% for all the inserts of different sizes. For RC MVCBCT, an inverse relationship between object size and relative error is present. Image degradation due to view aliasing artifacts and residual motion only affects the apparent size of the border region for large objects, but may affect the small object entirely. The image pixel dimension also affects smaller objects, since it is a larger fraction of the object's diameter. The residual motion of 3 mm also has a greater effect on smaller objects. The average error of the four larger inserts is about 10%, but errors increase significantly when the object diameter is less than 1 cm, indicating that volume measurement in RC MVCBCT is not suitable for small objects. For larger tumors, we have observed tumor volume reduction through a course of treatment using methods similar to what is described in the last section (Figure 4-3), so RC MVCBCT could provide tumor response assessments for

tumors larger than 2 cm in diameter, as verified by 4D kVCT imaging. However, the case study was for a regular breather who provided a sufficient distribution of uniformly spaced projections for RC MVCBCT. Irregular breathers will most likely have fewer projections with irregular spacing and could induce more artifacts. Further studies with irregular breathing patterns programmed into the phantom would be needed to determine the limitations on these situations.

We further reclassified the results based on different imaging parameters to study their influence on the accuracy of volume determination. Table 4-1 to Table 4-4 show the averages and standard deviations of relative errors belonging to different subsets of imaging parameters, including different respiratory states (Table 4-1), number of projections (Table 4-2), imaging dose (Table 4-3) and source energy (Table 4-4).

In Table 4-1, the relative error of static objects using standard MVCBCT is significantly smaller than that for FE or FI images using RC reconstruction. The error using static object MVCBCT data is even comparable to that of the kVCT for the four larger inserts. This is, in part, a consequence of using fewer projections, as can be seen as well in Table 4-2 where the relative errors for a complete rotation (359°) are lower than those for a 200° arc. However, one would expect that since the FE phase has more projections (70) than the FI phase (40), the FE phase should have better accuracy. This seems to be true only for the smallest sphere, while for the larger spheres, the FI phase is slightly better. This could be a consequence of the actual residual motion in the reconstruction. Although the projection sorting algorithm used a 3 mm window, the actual residual motion could be slightly smaller for the FI phase than for the FE phase. In fact, for the FI phase, typically only two projections were selected per respiratory cycle. With fewer projections in the FI phase, the likelihood of spanning the entire 3 mm window is lower.

It is very likely that more projections available in a wider range of angles for each phase may reduce the view aliasing artifacts for tumors, although the effect of these

artifacts on volume determination for spherical objects seems to be less of an issue than residual motion. However, using a 359° rotation increases the image acquisition time. This presents a compromise between reducing setup time and finding a more accurate protocol.

Table 4-3 and Table 4-4 present counterintuitive results. One would expect higher imaging doses to produce better images and, hence, improved volume determination. Similarly, one would expect softer energies to yield lower volume errors due to improved image quality. Figure 4-6 shows how image quality improves according to this expected pattern. Table 4-3 and Table 4-4, however, show the opposite trend. The differences, however, are within the standard deviations. Within experimental error, they essentially produce the same result. It is possible that the amount of residual motion varies quite a bit due to the random starting phase for image acquisition, and this is just enough to affect the results.

Sphere diameter, cm	Static	FE phase	FI phase
3.81	3.02%±1.53%	5.81%±2.03%	4.74%±3.12%
3.18	2.60%±2.28%	8.42%±2.95%	7.08%±3.03%
2.54	3.08%±2.51%	10.6%±5.20%	6.43%±5.26%
1.91	7.95%±10.3%	15.8%±5.65%	9.52%±8.11%
0.95	8.11%±6.73%	33.6%±20.3%	31.4%±16.4%
0.48	16.7%±10.1%	27.6%±19.9%	100%±48.3%

Table 4-1: Average and standard deviation of relative volume error for FE and FI phases

Sphere diameter, cm	200 degrees	359 degrees
3.81	2.84%±1.70%	5.91%±3.40%
3.18	6.33%±3.81%	5.12%±3.87%
2.54	8.09%±6.43%	3.62%±2.14%
1.91	11.8%±9.47%	6.58%±4.38%
0.95	21.3%±18.8%	19.3%±18.1%
0.48	55.8%±48.8%	36.2%±25.7%

Table 4-2: Average and standard deviation of relative volume error for different arcs

Sphere diameter, cm	5 MU	10 MU
3.81	3.66%±2.06%	5.38%±2.69%
3.18	4.52%±3.15%	7.54%±3.64%
2.54	5.29%±4.33%	8.08%±6.01%
1.91	8.20%±5.91%	14.0%±10.0%
0.95	23.9%±18.0%	24.7%±20.7%
0.48	42.1%±52.8%	47.7%±41.8%

Table 4-3: Average and standard deviation of relative volume error for 5 and 10 MU

Sphere diameter cm	kV CT	IBL MVCBCT	TBL MVCBCT
3.81	4.02%±1.04%	4.81%±0.85%	4.37%±3.02%
3.18	3.80%±1.10%	6.65%±3.79%	5.72%±3.71%
2.54	4.69%±2.94%	8.36%±5.64%	5.86%±5.13%
1.91	5.66%±2.28%	14.8%±9.76%	9.21%±7.55%
0.95	6.37%±3.89%	32.5%±20.1%	20.3%±17.6%
0.4	7.98%±2.76%	45.0%±62.8%	45.1%±37.3%

Table 4-4: Average and standard deviation of relative volume error for different energies

4.2.3 Motion quantification

Similar to volume determination, we also use relative error to present the normalized accuracy of motion quantification, expressed as:

$$relative\ error = \left| M_{actual} - M_{designed} \right| / M_{designed} \tag{4-2}$$

where M represents the displacement of the centroid between FE and FI respiratory states and the subscripts are consistent with those in (4-1). Figure 4-9 shows the average and standard deviation of the relative error of the motion of the six spherical inserts when using kV CT and RC MVCBCT. It should be noted that there is only one kV CT scan of a moving object. The measured displacement is very accurate for this kV CT scan. The three largest inserts have exactly the same motion measurement as the nominal designed value of 30*mm*. The error for the smallest of the three inserts is within 2%. For RC MVCBCT, the errors for the five largest inserts are all about 5%. The error is slightly larger for the smallest insert at 6.8%. All the relative error of motion is within 10%, which correlates well with the 10% amplitude interval in amplitude-based projection sorting.

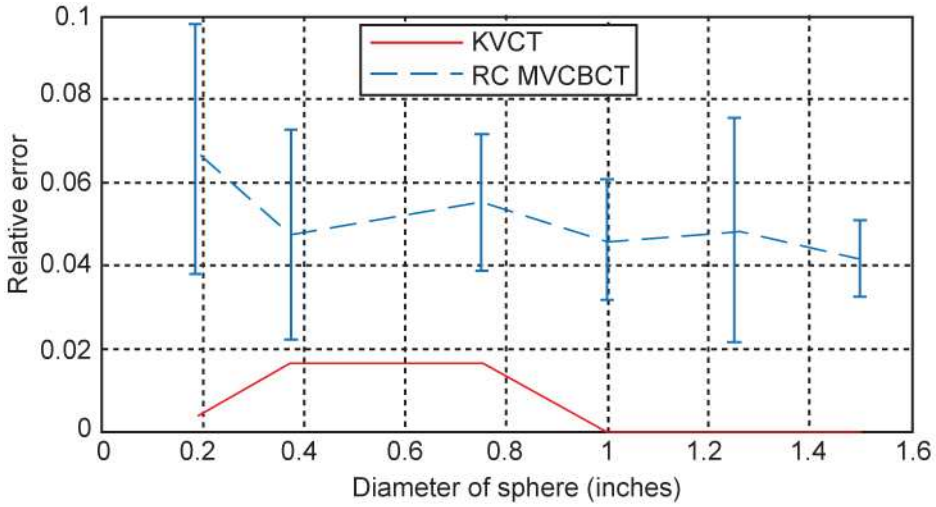

Figure 4-9: Relative error in displacement as a function of the phantom insert diameter.

Since the difference of motion quantification between different inserts is small, we present the average and standard deviation of the relative error in Table 4-5 by summarizing all the inserts belonging to the same type of RC MVCBCT scan. The nomenclature for the various imaging parameters is consistent with that of the previous section. The difference in relative error is very small (0.3%) between different imaging parameters, indicating that motion quantification is comparably more robust and insensitive to variation in manual contouring than volume determination. It is feasible to quantify tumor motion amplitudes between FE and FI respiratory states by using RC MVCBCT, even for objects with a diameter of about 0.5 cm. It should be noted that typical tumor motion amplitudes range from 1.0 cm to 2.5 cm, which is smaller than the phantom motion in this study. This gives us confidence to extend the practice of evaluating motion between the FE and FI respiratory states of 4DCT data to cases of RC MVCBCT taken immediately prior to treatment, to determine if the maximum motion is consistent with the one determined at the time of treatment planning

Imaging parameter	Relative error
kVCT	0.61%±0.83%
All RC MVCBCT	5.06%±2.14%
IBL	5.00%±2.07%
TBL	5.09%±2.22%
5MU	4.90%±2.21%
10MU	5.20%±2.13%
TBL 200	4.94%±2.41%
TBL 359	5.22%±2.13%

Table 4-5: Average and standard deviation of relative error of motion using kVCT and RC MVCBCT

4.2.4 Discussions of phantom experiment

Based on the error analysis in section 2.6.3, it is shown that Δk has larger influence in determining ΔT than ΔD. So it would be desirable to make Δk as small as possible. In section 2.6.3, a rough estimation of Δk on the order of 10% is used. In the RC reconstruction of patient images, it is further shown that the difference of DTMR quantification between FDK and SART algorithm is 11.3±10.4%. However, the studies taken on patient images lack the ground truth information. In this subsection Δk is further analyzed based on the motion quantification accuracy that derived from phantom images. First, the DTMR is rewritten here:

$$k = \frac{D_{EI}}{T_{EI}} \tag{4-3}$$

where D_{EI} and T_{EI} is used to represent the range of motion between FE and FI phase of 3D MVCBCT volume for diaphragm and tumor respectively. The error of DTMR can be further expanded as:

$$\Delta k = \frac{\Delta D_{EI}}{T_{EI}} + \Delta T_{EI} \frac{D_{EI}}{T_{EI}^{\ 2}} = \frac{\Delta D_{EI}}{T_{EI}} + \Delta T_{EI} \frac{k}{T_{EI}} \tag{4-4}$$

Similar to the analysis in section 2.6.3, if normal distribution assumption is used for all the random variables, the standard deviation of Δk can be written as,

$$\mathrm{var}_{\Delta k} = \sqrt{\frac{\mathrm{var}^2_{\Delta D_{EI}}}{T_{EI}^{\ 2}} + \mathrm{var}^2_{\Delta T_{EI}} \frac{k^2}{T_{EI}^{\ 2}}} \tag{4-5}$$

where it is influenced by both D_{EI} and T_{EI}. A typical value of diaphragm motion (D_{EI}) and tumor motion (T_{EI}) would be 25*mm* and 20*mm*, respectively. ΔT_{EI} achieves standard deviation of 1.52*mm* based on the phantom studies, while ΔD_{EI} reaches 0.58*mm*, based on the difference of motion quantification between FDK and SART algorithm for patient images. This set of parameters make Δk equal to 9.57%, which is very close to the 10% estimation.

Generally, the results of phantom studies provide some lower bound on errors, since the error may be greater due to inaccuracies in contouring non-spherical objects and reconstruction errors arising from irregular breathing patterns. First, because the study used spheres, they may be less susceptible to view aliasing artifacts. Volume determination for tumors may be less accurate than what is noted here, but these studies at least establish a lower limit on tumor sizes that can be evaluated with RC MVCBCT. For motion assessment, however, since the centroid of the tumor is used, it will be less sensitive to the identification of the tumor edges. This could explain why the accuracy for motion assessment is more robust. This could carry over into patients as well, and manual

identification of the tumor in projection images for a test patient showed that the tumor displacements between full inhale and exhale, averaged over all imaged respiratory cycles, was within 3 to 5 mm of the value determined from RC MVCBCT.

When one determines volumes and motion within a patient, they need to know whether their imaging methods are causing errors. Using spheres allows us to reduce the possible errors coming from user variability in contouring, and instead allows us to determine possible errors that come from the reconstruction of fewer projections than what one would normally expect. The patient imaging study presented in the last section has to rely on comparison of the RC MVCBCT results against the results from the 4D planning CT. While volumes can be compared for MVCBCT and 4DCT images taken on the same day, one cannot compare the amplitude of motion from full exhale to full inhale since the respiratory motion for the two separate imaging sessions may be different. This is the best one can do for patient studies, since the true motion and volume of the tumor cannot be established; even the 4D planning CT will contain residual motion and artifacts, and its usefulness in serving as ground truth is subject to these errors.

In this section, the feasibility of using RC MVCBCT to quantify object motion and size has been evaluated. The primary source of object boundary detection errors is the reconstruction error induced by missing projections. Better accuracy can be achieved for volume determination when the object is sufficiently large (a minimum diameter of 2 cm). For larger tumors, response assessment in terms of volume reduction is feasible for regular breathers, at least until the tumor shrinks down to 2 cm, where a 4D kVCT would be needed for volume determination. Motion measurement results, on the other hand, are more robust. The relative error is within 10% for even the smallest object, and it is independent of energy, dose and protocol. This would allow us to relate diaphragm motion to tumor motion which, in turn, could be used for calibrating surrogates of tumor motion (since we can track the diaphragm in the projections), even for the smallest lung tumors that are clinically encountered in radiotherapy. The phantom studies in this work

can serve as a quality assurance method for any type of respiratory-correlated imaging, since they provide ground truth for size and motion, which cannot be unequivocally established with patient images. In the next section, we will present our current technique based on a clinical software "UIHC 4D verification" to quantify tumor and IHDA motion in real patient images to derive DTMR. The procedure of using IHDA motion signal and DTMR value to calibrate the strain gauge will also be presented.

4.3 Current method implemented for strain gauge calibration on clinical software

To calibrate the strain gauge based on IHDA motion signal and DTMR value, one has to derive both the tumor centroid and IHDA position in FE and FI phases of the 3D MVCBCT volume. The IHDA position could be directly determined from the volumetric image. The tumor centroid position, however, should be computed from a 3D segmented tumor mask.

For the phantom study, the manual segmentation based on the spherical inserts is relatively easy, since the clinicians can directly fit a spherical shape to match the boundary of inserts. However, for patient images, the irregular shape of the tumor requires that the tumor boundary has to be identified slice by slice. This is very tedious in 3D images. An automatic segmentation approach is needed. However, the variation of tumor in size, shape, structural pattern, and the degree of attachment to normal anatomic structures makes the automatic segmentation a challenging task. Over the years there have been many publications devoted to this area, including gray value thresholding (Diciotti et al., 2008; Goo et al., 2005), region growing (Brown et al., 1997; Brown et al., 2001; Dehmeshki, Amin, Valdivieso, & Ye, 2008), classification based approach (Armato III, Giger, & MacMahon, 2001), and optimization based techniques (Opfer &

Wiemker, 2007; Wang et al., 2009). There are also many studies dedicated to lung tumor segmentation in a series of follow-up CT scans, such as patient-specific prior model developed by Brown et al. (Brown et al., 2001), and techniques combining segmentation and registration (Kabus, Müller, Wiemker, & Fischer, 2008). These methods took advantage of the similarities of tumor shape of the same patient in different scans.

Though many clinical tools such as Pinnacle have integrated algorithms for lung tumor segmentation, there is still a long way to go before clinicians can rely solely on the result of automatic algorithms to create GTVs for the treatment. Furthermore, the tumor segmentation in the RC MVCBCT volume is more error-prone than diagnostic CT, due to the poorer imaging quality and view-aliasing artifact. Human verification and modification is still indispensable at the current stage. To develop a tool useful for clinical application, the accuracy of the segmentation approach is not our primary concern in this proposal. Instead, we try to implement an efficient approach which enables intuitive user interaction and modification during the segmentation. The tumor segmentation procedure could be semi-automatic, but it should not take longer than the clinical limit.

In this section, we will first discuss two graph-based algorithms that we have implemented for tumor segmentation. In the last section we will present how to use the derived DTMR and IHDA motion to calibrate the strain gauge.

4.3.1 Optimal graph search based approach

In Chapter 3, a novel method based on graph search framework for 3D organ segmentation from 2D projection images was presented. In this section, the graph search framework is used again, but for a different application: simultaneously segment the tumor in both the FE and FI phases of MVCBCT images. One of the advantages of using

graph search methods is that we can impose the shape similarity between the two phases to the segmentation result. Though there is some deformation when the tumor moves from FE phase to FI phase, the general shape should not change too much during respiration. The optimal graph search method is very helpful to meet our needs, since the constraint on the distance of the tumor surface in different phases can be represented by the inter-column edge. A detailed description of our implementation is as follows.

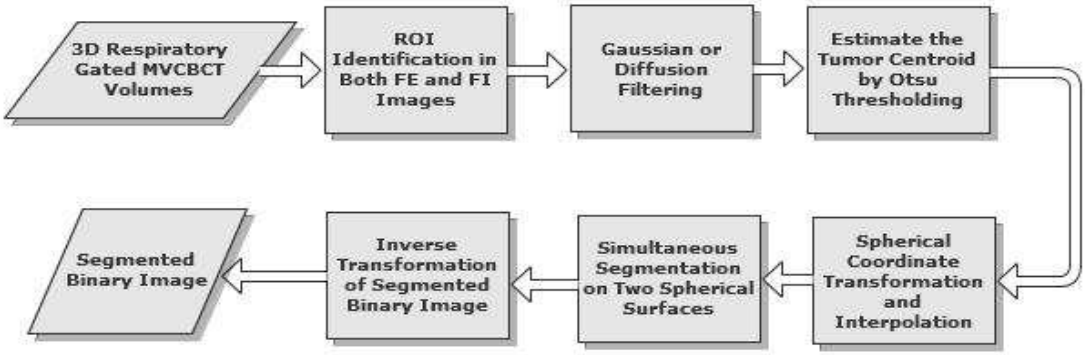

Figure 4-10: Flowchart of simultaneous segmentation of tumor in both FE and FI images using optimal graph search method

Figure 4-10 shows the main framework of the method. First, the user is required to initialize a region of interest (ROI) of tumor in both FE and FI images. In the current interface, the ROI is a 3D ellipsoid that contains the entire tumor. A screen layout is shown in Figure 4-11, where the FE and FI can be displayed simultaneously on the screen by adjusting the transparency of each image. The purple ellipse represents the ROI contour in this slice. The input is the 3D volumetric region specified by the ROI. The algorithm starts by pre-filtering the 3D ROI image, either based on a Gaussian filter or the anisotropic diffusion filter. Generally speaking, the Gaussian filter is faster, but the

diffusion filter has the advantage of preserving the boundary while reducing noise at the same time.

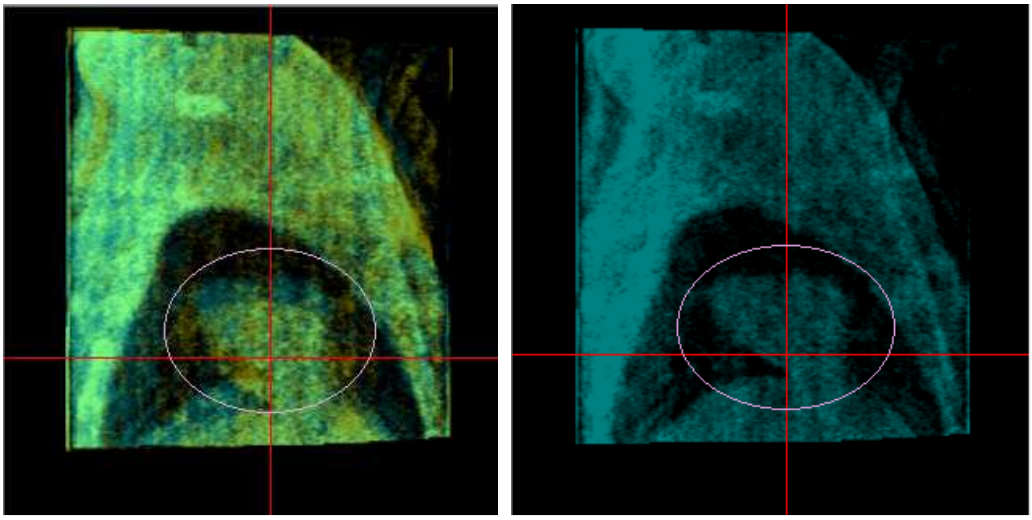

Figure 4-11: Left: A screen layout showing the FE (blue) and FI image (yellow) together in one sagittal plane; Right: only with FE image.

To restrict the change of the tumor surface from FE to FI phase, we have to first know about the relative motion of the tumor. Otsu's method (Otsu, 1975) is used to convert the gray scale image to a binary segmented image under an optimized threshold value. Thus a rough position of the tumor centroid can be estimated by taking the average of all the "foreground" pixels in the binary image. Otsu's method is based on the assumption that the image to be segmented generally contains two classes of pixels. This assumption matches our situation well, since the attenuation coefficients of the lung tumor and the surrounding pulmonary region are significantly distinct. Some of the peripheral lung tissues, such as the diaphragm and normal organs, have attenuation coefficients that are very similar to that of the tumor. However, these tissues exist in both

FE and FI images. The error of relative motion of the tumor induced by these tissues can be greatly cancelled by subtraction between the tumor centroid in two images.

Based on the estimation of the tumor centroid, we are able to establish the correspondence between the two images. The process of graph construction is based on a spherical coordinate system (r, θ, φ), where r represents the distance to the origin, θ represents the inclination angle measured from the zenith direction (SI direction in patient coordinates), φ represents the azimuth angle (Figure 4-12a). The tumor centroid in each image is the origin of the coordinate system. The transformation from the original Cartesian coordinate to the spherical coordinate is as follows:

$$r = \sqrt{x^2 + y^2 + z^2}$$
$$\theta = a\sin\left(\sqrt{x^2 + y^2} \Big/ \sqrt{x^2 + y^2 + z^2}\right)$$
$$\varphi = a\sin\left(y \Big/ \sqrt{x^2 + y^2}\right)$$

(4-6)

A 4D graph is created from two 3D ROI volumes, where the 4D coordinate (r, θ, φ, t) is used to specify each node of the graph. The additional parameter t represents the phase of the image. Currently since there are only FE and FI images, t only has two values: 0 and 1. The other three parameters (r, θ, φ) identifies the position of the node in the original image using equation (4-6). The cost of each node $C(r, \theta, \varphi, t)$ is based on the gradient amplitude, which is computed as the difference of filtered gray value of the image (represented by G) between adjacent nodes along the radial direction:

$$C(r,\theta,\varphi,t) = G((r + dr,\theta,\varphi,t) - G(r,\theta,\varphi,t)$$

(4-7)

In this equation dr is the smallest unit along the radial direction, which is equal to one voxel spacing in our application. As discussed, the tumor has larger gray values

(attenuation coefficients) than the surrounding area. Thus the cost function designed in this way favors the direction of the gradient that points outwards from the origin. This property enables the detected surface to locate on the boundary that has a higher intensity than the inner side. To derive gray values in spherical coordinates, bilinear interpolation is applied to resample the original image in Cartesian coordinates.

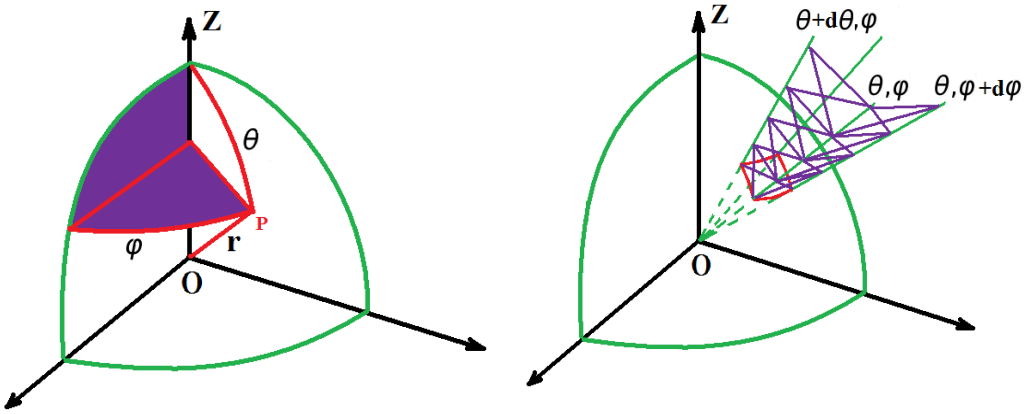

Figure 4-12: **Left**: A simple illustration of the spherical coordinates used in tumor surface segmentation; **Right**: An illustration of inter-column constraint.

Each column of the graph is composed of all the nodes that have same value of (θ, φ, t). There are two types of constraint applied to the simultaneous surface segmentation: surface smoothness constraint ΔR_{intra} and inter-surface constraint ΔR_{inter}. The first constraint connects adjacent columns in one image, which is illustrated in Figure 4-12b. We set the constraint along both θ and φ directions, which requires that the node position of one surface between adjacent columns should not be larger than ΔR_{intra}. The inter-surface constraint requires that the difference of the node position from two surfaces in the same column (θ, φ) should not be larger than ΔR_{inter}. Under this constraint the tumor surfaces in two images are able to interrelate with each other. The smaller ΔR_{inter} is, the

more the constraint is forced on the shape similarities. In the current implementation we set ΔR_{inter} to dr, ΔR_{inter} as five times dr.

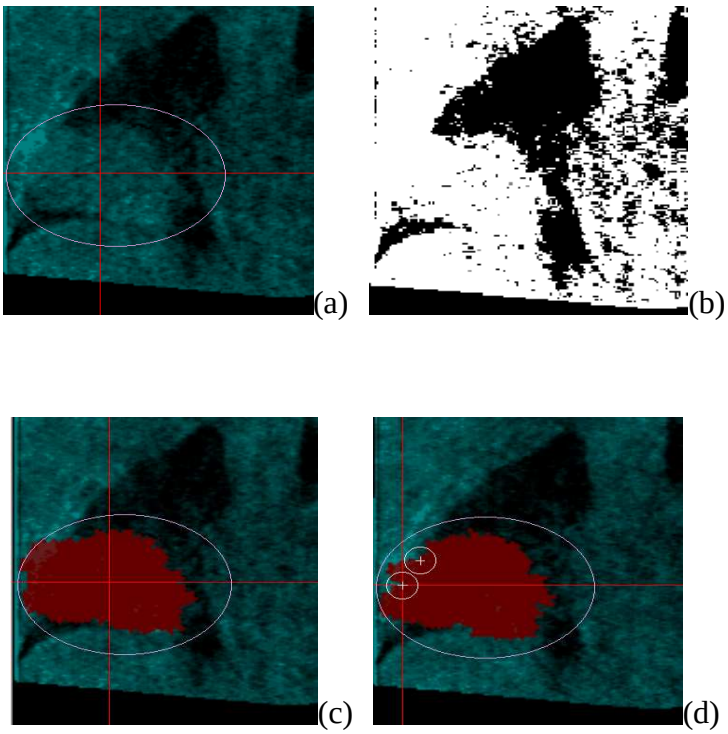

Figure 4-13: 3D tumor segmentation in RC MVCBCT volumes based on the graph search method. The image is shown in a coronal plane. (a) original image; (b) result after Otsu threshold; (c) segmented result based on graph search (red region); (d) segmented result after user correction. The user added two constraint points in this image, which makes a change in the tumor surface.

The two interrelated surfaces are able to be detected, which have the maximum summation of cost values satisfying both smoothness and inter-surface constraints. The constraint optimization is realized by transforming the problem into computing a minimum *s-t* cuts problem. According to the graph construction procedure, each node (r, θ, φ, t) has to connect with three nodes from other columns to apply the smoothness and inter-surface constraint. The three nodes are $(\max(r_{\min}, r - \Delta R_{inra}), \theta + d\theta, \varphi, t)$,

$(\max(r_{\min}, r - \Delta R_{\text{int } ra}), \theta, \varphi + d\varphi, t)$ and $(\max(r_{\min}, r - \Delta R_{\text{int } er}), \theta, \varphi, t + dt)$, where r_{min} is the bottom node of each graph. Apart from those edges, other types of edges are also needed, including the intra-column edges connecting the descending node, and edges connecting *s* and *t* nodes. The minimum *s*-*t* cuts problem could be further solved by maximal flow/minimum cut algorithm in polynomial time such as push-relabel (Cherkassky & Goldberg, 1997) or Boykov's method (Boykov & Kolmogorov, 2004). After the completion of maximum flow computation, the node is transformed back to Cartesian coordinates. After the minimal cut computation, the node that connects to *s* belongs to the tumor, while the node that connects to *t* is the background.

We have also made this algorithm work interactively with the user's modification. In the current GUI we have designed, the user is able to add a few constraint points, which are used to force the surface to locate on the specified locations. This constraint is realized by changing the cost value of the corresponding node to be large enough to guarantee that the desired node is on the boundary of the segmentation result. An example of the segmentation result without and with the user's modification is shown in Figure 4-13c and Figure 4-13d respectively, where the user is able to make the tumor surface pass through the desired locations.

4.3.2 Interactive graph cut algorithm

Though tumor segmentation based on optimal graph search provides a promising solution to our requirement, there are several limitations of the current implementation. First, since the double-surface segmentation is performed on the radial basis, the tumor in both FE and FI images has to be star-shaped. However, this is not always true from our experience with the patient images. Second, the transformation between Cartesian coordinates and spherical coordinates, as well as the interpolation process, is very time-

consuming. Methods based directly on original imaging coordinates would be more desirable. Third, the interactive modification by the user is not very easy to manipulate under the radial basis framework. The user has to draw the constraint points one by one and should be very careful on the position of the surface. It would confuse the algorithm if the user happens to click on two nodes that belong to the same column of the constructed graph.

Considering all those factors, more recently we have implemented a more flexible algorithm based on interactive graph cuts. This method was first proposed by Boykov et al. (Boykov, Veksler, & Zabih, 2001; Boykov & Funka-Lea, 2006) and is a powerful technique for optimal boundary segmentation. It is also based on solving a maximum flow/minimum cut problem in the constructed graph, which is similar to the previous method. However, there is no topology of "column" in the graph cut algorithm. Each image voxel is a node in the graph, which makes the constructed graph based on the original image coordinate (each voxel is connected to its neighboring voxels). The segmentation result is a direct separation of all the image voxels into two sets. These characteristics makes the graph cuts algorithm significantly different from the graph search method. One of the great advantages of this method to our application is that the user can interactively identify the labeling of some of the image voxels as "object" or "background". Once an initial segmentation is complete, the user can further modify the manual labeling and redo the segmentation. The segmentation on the subsequent times can utilize the information of the remaining edge capacity of the graph from the previous round, which makes the computation of maximum flow much faster than the first time.

The workflow of the interactive graph cuts method is shown in Figure 4-14: , where several steps are the same as those of the previous method. It differs in two aspects: (1) there is no forward or inverse transformation and interpolation of the coordinates; (2) the manual labeling can be used efficiently in multiple times to assist the clinicians to modify the segmentation result.

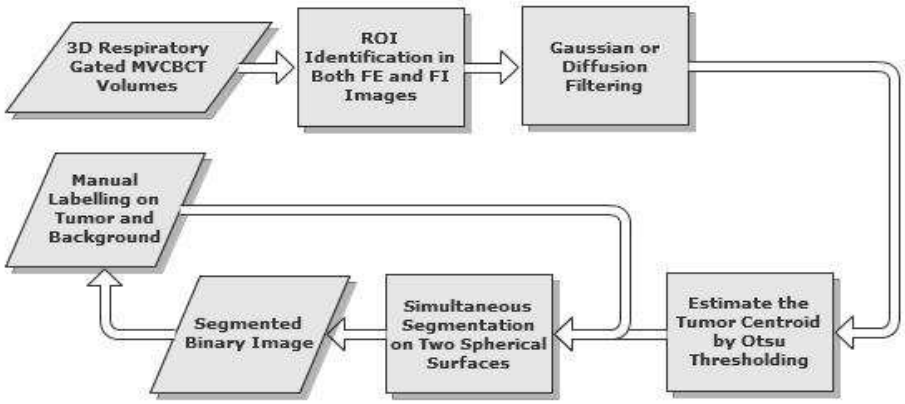

Figure 4-14: Flowchart of simultaneous segmentation of tumor in both FE and FI images using interactive graph cuts algorithm.

Once the initial estimation of the tumor centroid in two images is determined, the position of the tumor centroid is used as the origin of the image coordinate. We use the 4D coordinate *(x, y, z, t)* to represent the graph nodes, where *(x, y, z)* is the Cartesian coordinate of the image voxel. Similar to the previous subsection, *t* is the phase number of the image. There are also two types of edges in this graph: edge connects adjacent voxels in the same image, and edge connects voxels that have the same position from two images. The intra-image edge is based on a 26-neighborhood metric. Thus each node *(x, y, z, t)* is connected to *(x+dx, y+dy, z+dz, t)*, where the possible value of *dx, dy, dz* is {-1, 0, 1} and the neighborhood criterion requires that $max(dx, dy, dz) \leqq 1$. The inter-image edge constrains the shape difference of the tumor. Each node *(x, y, z, t)* is connected with *(x, y, z, t+dt)*, where *dt* could be 1 or -1.

From my experience, the boundary penalties set in each edge capacity plays a vital role in the final segmentation result. A poor set of boundary penalties may result in shrinkage of the segmented result to the initial labeling. In the current implementation, we used the function proposed in Boykov's paper (Boykov & Funka-Lea, 2006):

$$B_{p,q} = \exp[-\frac{(I_p - I_q)^2}{2\sigma^2}]$$

(4-8)

In this equation, the boundary penalties $B_{p,q}$ that connects voxel p and q is determined by the gray value of those voxels I_p, I_q and a parameter σ representing the variance of the gray value. This function penalizes a lot for discontinuities between pixels of similar intensities when $|Ip\text{-}Iq|<\sigma$. Conversely, the penalty is small when $|Ip\text{-}Iq|>\sigma$. Thus we have to choose this parameter very carefully. To achieve a robust segmentation result, currently we calculate the variance of image intensities prior to the graph cuts computation. The ROI image is the smallest rectangular box that contains the user-specified ellipsoid. All the voxels outside the ellipsoid is automatically assigned background label, while the voxels within a certain distance to the origin are assigned foreground (tumor). Our algorithm starts with the computation of the standard deviation among all the foreground and background voxels respectively. The parameter σ for intra-image edge is a scale of the summation of foreground and background variance. A different scale is applied for the inter-image edge.

The major problems of using the graph cuts algorithm without user initialization is the leakage to the surrounding tissues when the tumor is attached to a tissue that has very similar attenuation coefficients (Figure 4-15b). However, this problem could be solved by reducing the tumor ROI and manual identification (Figure 4-15c). Recently, Song et al. (Song, Chen, Bai, Sonka, & Wu, 2011) presented a new segmentation approach that incorporates the advantages of both graph cut and graph search algorithm. This approach enables simultaneous segmentation of tumor and the surrounding surface like the diaphragm, and is able to partly solve the leakage problem in some cases. Promising results have been achieved in some of the RC MVCBCT images, which makes the algorithm potentially useful in segmentation of the tumor which is attached to the surrounding tissues. On the other hand, even if the leakage problem is alleviated, the manual modification in some other problematic areas is still required. Our current framework based on graph cuts segmentation is able to achieve satisfying results after

adding three or four areas of manual labeling, based on visual inspection. For a tumor with a diameter larger than 5cm, the current algorithm is able to segment a tumor in FE and FI images simultaneously within 5sec, using an Intel® Core ™ i7-2620M CPU @2.70GHz laptop computer with 4GB RAM. The segmentation using information of previous edge capacities is within one second.

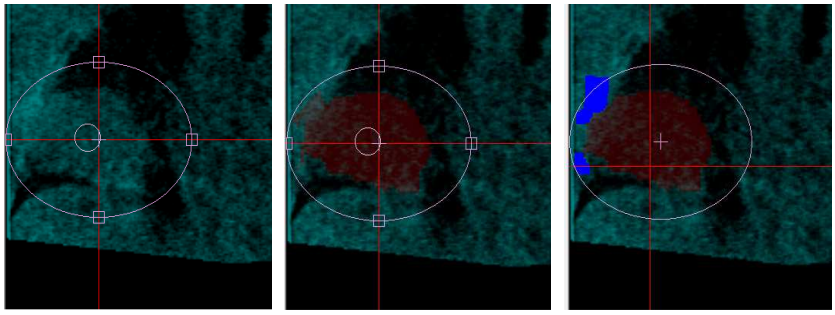

Figure 4-15: 3D tumor segmentation in RC MVCBCT volume using interactive graph cuts. Result is shown in coronal slice: (a) original image; (b) initial segmentation (red region) based on elliptical ROI without manual correction. Some part of the segmented volume leaks to the peripheral lung regions on the left; (c) modified segmentation (red region) with manual correction (blue region).

4.3.3 Clinical software for strain gauge calibration

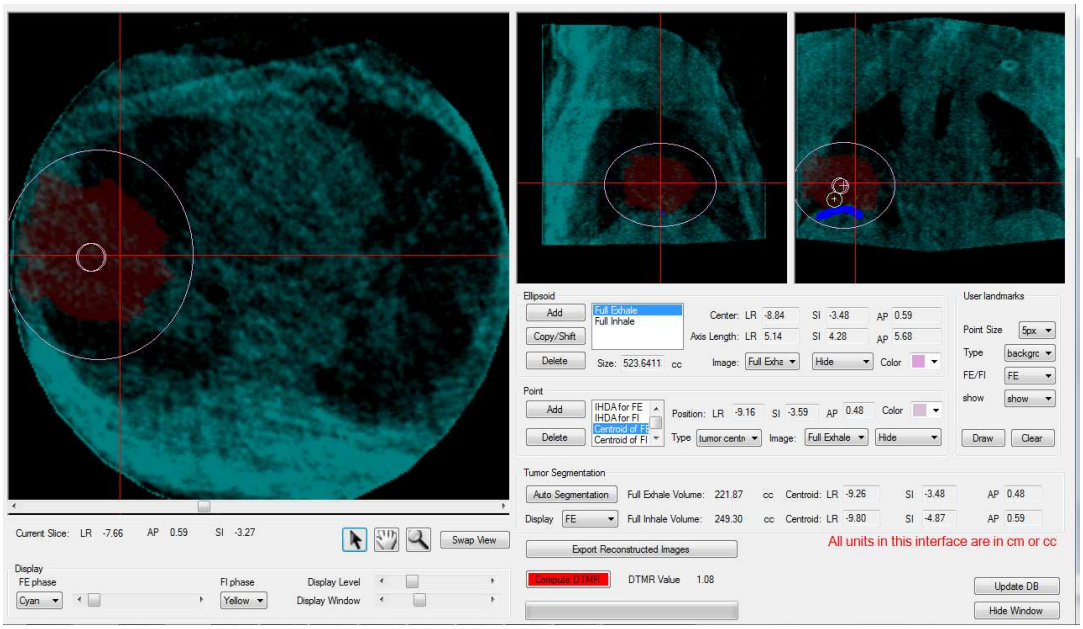

Figure 4-16: The user interactive interface to quantify DTMR after reconstruction of both full exhale and full inhale phase of MVCBCT. The full exhale image is shown as green in axial plane, lateral plane and sagittal plane from left to right. The dark red area is the tumor segmentation result.

In the current framework, after the volume of FE and FI phases are reconstructed, the clinicians are able to segment the tumor semi-automatically in a user-interactive interface introduced in section 4.3.2. The IHDA position in the two volumes can be identified directly by using the interpolated ray tracing algorithm. A snapshot of the current user interface containing the volume of full exhale is shown in Figure 4-16, where the tumor and diaphragm boundaries are much clearer than those of the un-correlated volume.

Generally we assume a linear relationship between diaphragm and tumor motion. Since the FE and FI phase of MVCBCT is averaged from all the projection images sorted to FE and FI respectively, the DTMR is a significant clinical parameter to describe the

overall scale of linearity during the scan. Once the DTMR is determined, the clinicians are able to move into another user interactive interface to quantify the gating threshold for treatment. A snapshot of this GUI is shown in Figure 4-17. In the left, the correlation between strain gauge and IHDA is plotted, where the vertical axis is the absolute amplitude of the IHDA, and the horizontal axis is the percentage scale of the strain gauge. Two parabolic curves are fitted for the relationship between the two variables in inhale and exhale phase respectively. The fitting is based on random sample consensus (RANSAC) (Fischler & Bolles, 1981), where only a subset of sampled points which are deemed "good for fitting" are used, while excluding the potential outliers. The fitting is based on the least square metric.

The difference in the correlation pattern in exhale and inhale phase is due to the phase difference between the strain gauge and diaphragm motion. The workflow is often initiated with a given allowed tumor motion margin, which represents the range of amplitude that allows the beam to turn on. By multiplication with DTMR, we can derive the allowed range of IHDA motion. Thus the threshold of the strain gauge during exhale and inhale phases could be determined by finding the intersection with the parabolic curves. In the example shown in Figure 4-17, the DTMR is 1.08. A 10mm tumor motion range is given, which results in 33% exhale and 63% inhale threshold.

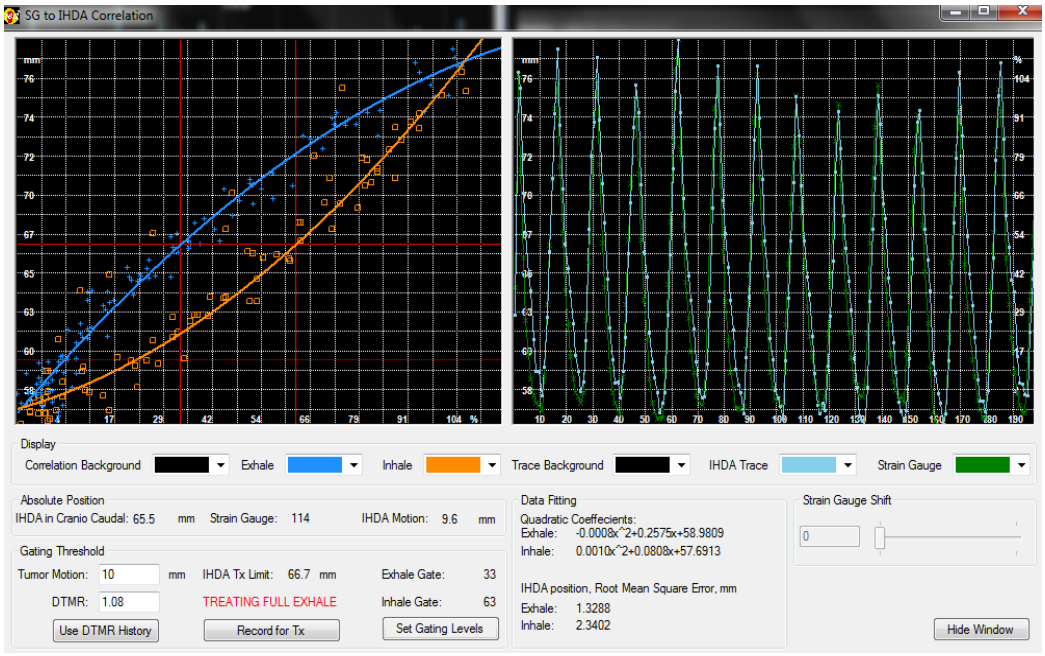

Figure 4-17: the user interactive interface to determine the gating threshold during treatment based on DTMR. The blue and orange curve in the left fits the correlation between IHDA position and strain gauge percentage in exhale and inhale phases respectively. The strain gauge percentage value and IHDA motion amplitude as a function of time is shown on the right.

CHAPTER 5

MOTION COMPENSATED RECONSTRUCTION

In the last chapter, the accuracy of using RC volume for motion and volume quantification of the tumor has been shown. However, the major disadvantage of RC reconstruction approach is the view-aliasing artifacts caused by an insufficient number of projection images. This problem can be mitigated by using multiple rotations or slowing the gantry rotation speed (T. Li et al., 2006; T. Li & Xing, 2007)(T. Li et al., 2006; T. Li & Xing, 2007) to increases the number of projection images for each phase. However, for those methods, the increased image acquisition time and the amount of imaging dose delivered to the patient make it impractical to implement clinically. Other approaches seek to reduce the aliasing artifacts using algebraic reconstruction techniques and compressed sensing theory (Leng et al., 2008; Sidky & Pan, 2008), which enable accurate image reconstruction using under-sampled projection images. These iterative reconstruction algorithms are very time-consuming and require GPU platform for clinical implementations.

An alternative approach is based on motion compensated (MC) reconstruction. In this method a motion model is provided in advance of the reconstruction and is incorporated into the de-convolution process during the back-projection. Usually, the motion model is represented by a time sequence of displacement vector fields (DVF). A mathematical description of the MC approach based on Feldkamp, Kress, Davis (FDK) reconstruction algorithm is explained in the work of Schafer et. al. (Schafer, Borgert, Rasche, & Grass, 2006). A straightforward method of deriving patient motion is to perform a deformable registration among different phases of the 4D planning CT to obtain a 4D DVF (T. Li et al., 2006; Rit, Wolthaus, van Herk, & Sonke, 2009; Q. Zhang et al., 2010). The accuracy of this approach is degraded by the motion that occurs

between treatment planning and treatment delivery. Li. et al. proposed registering the different phases of gated KV-CBCT images (T. Li et al., 2007). However, since the 3D RC cone beam volumes are contaminated with severe aliasing artifacts, the accuracy of using those images to derive DVF remains ambiguous.

One promising solution is to use MVCBCT projection images to monitor or detect intra-fractional motion, since they have a high temporal resolution (about 0.3s for MVCBCT). Different approaches based on 2D motion detection have been proposed, including (1) monitoring tumor change by projecting a volume of interest for visualization (Reitz et al., 2008); (2) extracting the 2D/3D position of a projected implanted marker (T. Li, Schreibmann, Yang, & Xing, 2006) or diaphragm edge (Siochi, 2009), which can also be used as respiratory signal for RC reconstruction; (3) performing deformable registration between the projected 3D volume and the 2D projection images to create a displacement vector field (FOV) for motion-compensated reconstruction. Direct tumor tracking or detection in 2D images is mainly focused on fluoroscopy (Shimizu et al., 2001). However, few studies have addressed direct tumor detection in MVCBCT projection images, which suffer from relatively poor contrast due to the energy range of the imaging photons and the interfering anatomies. The registration approach aims to optimize some similar metric between the forward-projected image of the 3D volume and the original projection image (T. Li et al., 2007; Rit et al., 2009). Once again, the iterative scheme of forward-projection and optimization is extremely slow, making it difficult for an immediate application in the treatment room.

Alternatively, one can compute a (3D+t) deformable object model from the 2D projection images and makes use of this model for MC reconstruction. Various approaches have been proposed for recovering a 3D shape from 2D projections, including the thorax and the lung (Lotjonen et al., 1999; Lotjonen, Reissman, Magnin, & Katila, 1999)(Sato, Moriyama, Hanayama, Naito, & Tamura, 1997; Veisterä & Lötjönen, 2001) and left ventricle surfaces (Chen et al., 2011; Moriyama et al., 2002; Sato et al., 1997;

Veisterä & Lötjönen, 2001). Usually, a geometric prior model is segmented from a 3D planning volume and projected onto 2D projection images (orthogonal biplane or multi-views). Then the model is deformed according to the information provided in the projection images. The computation of displacement vectors for the deformation varies among different studies, including manual contoured outline (Veisterä & Lötjönen, 2001), boundary detection along the projected normal direction of silhouette outline (Chen et al., 2011), elastic matching between virtual projections and real X-ray images (Lotjonen et al., 1999; Lotjonen, Reissman et al., 1999), and iterative fitting to a 4D closed surface based on B-splines (Moriyama et al., 2002; Sato et al., 1997).

In this chapter a novel MC reconstruction approach that uses the DVF generated from a 3D dynamic geometrical object shape model is presented, which is based on the segmentation framework introduced in chapter 3. The new approach has several advantages, which make it distinctive from previous methods:

(1) The method takes advantage of the projection images to generate DVF while maintaining a clinical acceptable time frame. Instead of being used for deformable registration with forward projection (T. Li et al., 2007), the projection images are used to compute the deformation of a geometric prior model;

(2) The deformation of the geometric prior model is computed simultaneously for all the respiratory phases. We convert the mesh deformation into a multiple interrelated 3D surface detection problem, where the globally optimal solution can be found in polynomial time by solving a maximum flow problem in a 4D directed graph;

(3) Both mesh surface smoothness constraint and motion displacement constraints are employed in the graph search framework, which makes the object motion segmentation very robust.

The method is tested on lung motion model extraction from MVCBCT projection images. The DVFs generated from lung motion model are used for respiratory MC reconstruction. The method is compared with three other approaches based on reconstruction accuracy: (1) RC FDK reconstruction, (2) MC reconstruction using DVF generated from 4D planning CT and (3) MC reconstruction using DVF generated from RC MVCBCT. This chapter is organized as follows. Section 1 introduces the details of our MC reconstruction approach. Section 2 describes how the new method is compared and validated with other three traditional MC reconstruction approaches, while the evaluation result is also presented. Section 3 concludes with a discussion of the experimental results.

5.1 The motion compensation framework

Figure 5-1 shows the general framework for deriving DVF from MVCBCT projection images. It's a natural extension of the segmentation framework introduced in chapter 3. The lung with the tumor is segmented in the full exhale (FE) phase of the 4D planning CT. A B-spline deformable registration method is used to derive the DVF from the FE phase to the full inhale (FI) phase of the planning CT (Cao, Du, Ding, Reinhardt, & Christensen, 2010). The DVF is then used to deform the lung mesh created from the FE image to generate a mesh for the FI phase. Since these steps only require the 4D planning CT, they can be performed after the planning scan.

On the treatment day, once all the projection images are acquired, a 3D MVCBCT is reconstructed from all the projections. The lung model generated in the FE and FI phases of the planning CT is aligned to the cone beam coordinates. The averaged mesh between the FE and the FI phase is computed and used as the initial mesh model, which is further projected onto each 2DCB projection. The CB projections are sorted according

to 3D anatomical positions of the ipsi-lateral hemi-diaphragm apex (IHDA) into several respiratory bins. The locations of mesh points in each respiratory phase are computed by using the segmentation framework introduced in Chapter 3. The major difference to tumor segmentation is that a subset of mesh edges called “candidate edges” are used instead of silhouette edges to provide external forces to deform the mesh. The reason of using those edges for lung motion segmentation will be discussed in details later.

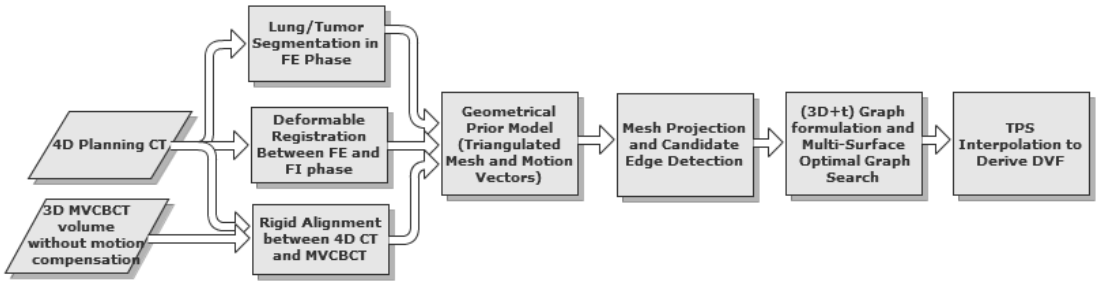

Figure 5-1: The general framework for deriving DVF from MVCBCT projection images

5.1.1 Respiratory signals and phase sorting

During the localization scan, the CB projections are correlated with the respiratory signal. The standard of care for this procedure is motion monitoring using the AZ-733V respiratory gating system (Anzai Medical Co., Tokyo, Japan). However, several studies have suggested that more accurate tumor motion may be determined when using internal anatomical surrogates, such as the apex of the diaphragm (Cervino et al., 2009; Keall et al., 2006). The respiratory signal used in this study is based on this approach, which detects the apex of the diaphragm using the algorithm presented in chapter 2. The respiratory sorting is based on both the motion amplitude of the diaphragm and the inhale/exhale session. This involves three steps: First, the local maxima and

minima of the signal are detected. Second, based on those maxima/minima positions, each projection image is labeled with a binary respiratory state “exhale” or “inhale”. Finally, the projection images are sorted into multiple bins based on both the amplitude and the label. Figure 5-2 illustrates an example of the respiratory sorting. One may wonder why phase 8 to 11 is missing in the second wave valley. That is exactly how the algorithm works. During the second wave valley the IHDA does not go that far towards inferior location, assigning phase 8 to 11 would vary IHDA location from what it should be during the first wave valley.

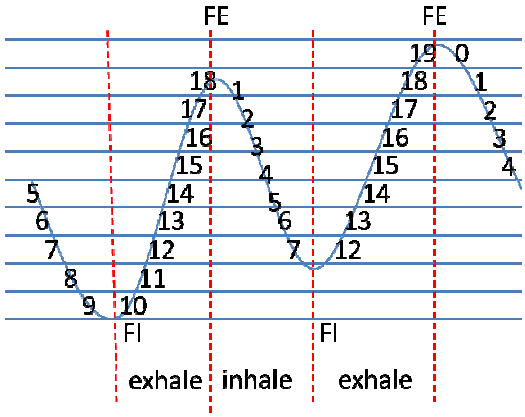

Figure 5-2: An example showing a respiratory signal sorted into 20 respiratory bins ranging from 0 to 19.

5.1.2 The initial lung model

Segmentation of the lung takes two steps. First, an automatic algorithm is implemented to generate a binary image of the whole thoracic cavity based on gray level threshold and connected with component labeling. The binary image contains both lungs, including the trachea and the bronchia. Secondly, manual adjustment is used to keep the

cancerous lung while removing everything else. A triangulated mesh of the lung is generated from the binary image using the marching cubes algorithm {207 Lorensen, W.E. 1987} (Figure 5-3). Using an accurate B-spline deformable registration algorithm, we preserved both the parenchymal tissue volume and probability measure of vessel structure {208 Cao, K. 2010}. The optimization metric is based on the sum of the squared tissue volume difference and the sum of the squared vesselness measure difference, respectively {208 Cao, K. 2010}.

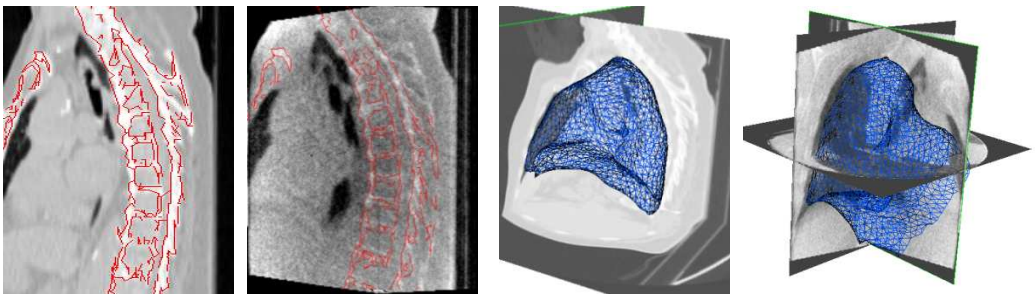

Figure 5-3: The major process of generating initial lung shape model in the MVCBCT coordinate: (a) bony structures (red) segmented from 4D planning CT; (b) The alignment of the bony structures onto the fully reconstructed MVCBCT; (c) Triangulated lung mesh segmented from the FE phase of 4D planning CT; (d) The lung mesh transformed to the MVCBCT coordinate.

The mesh created in the FI phase is derived from the FE phase based on the DVF computed during inter-phase registration. Using our in-house software platform, the MVCBCT image without MC is rigidly aligned to the coordinates of the 4DCT using bony anatomic structures (see Figure 5-3a, b). The lung meshes in the FE and FI phases are then transformed to the cone beam geometry (Figure 5-3d), which provides the initial lung shape and motion model. The initial model is the average of the meshes of the FE and FI phases. For each mesh point, a range of motion is determined using the equation $P_{mean}+\alpha(P_{FE}-P_{mean})$ and $P_{mean}+\alpha(P_{FI}-P_{mean})$, where P_{FE} and P_{FI} is the corresponding

positions in FE and FI phases, respectively, and P_{mean} is the mean position. α is used to control the allowed range, which is typically set between 1.5 and 2. In this study, it is assumed that each mesh point moves along the direction defined by P_{fe} and P_{fi}, providing a close approximation to the real motion trajectory. The generation of the initial mesh is performed off-line during the planning stage and can be completed within 2 minutes.

5.1.3 Candidate edge selection

The gradient amplitude and the direction of the lung boundary are the most salient features of the projection images. In order to deform the initial mesh towards these desired locations, the mesh points that correspond to the strong boundary in the projection images should be selected as anchor points to guide the deformation of the other points. For tumor segmentation, the strong boundary in the projection images typically corresponds to the silhouette contour of the mesh, which has been discussed in section 3.1.3. This is the same case for left ventricle segmentation in C-arm cone beam projection images, with details in my previous paper (Chen et al., 2011). Unlike the left ventricle or tumor, however, the lung mesh is a concave shape. During inspiration the lung walls bulges outward while the diaphragm hollows inward. Due to this characteristic, the silhouette contour of the projected lung mesh may not correspond to an equally strong boundary in the projection image. This is indicated by the red arrow in Figure 5-4.

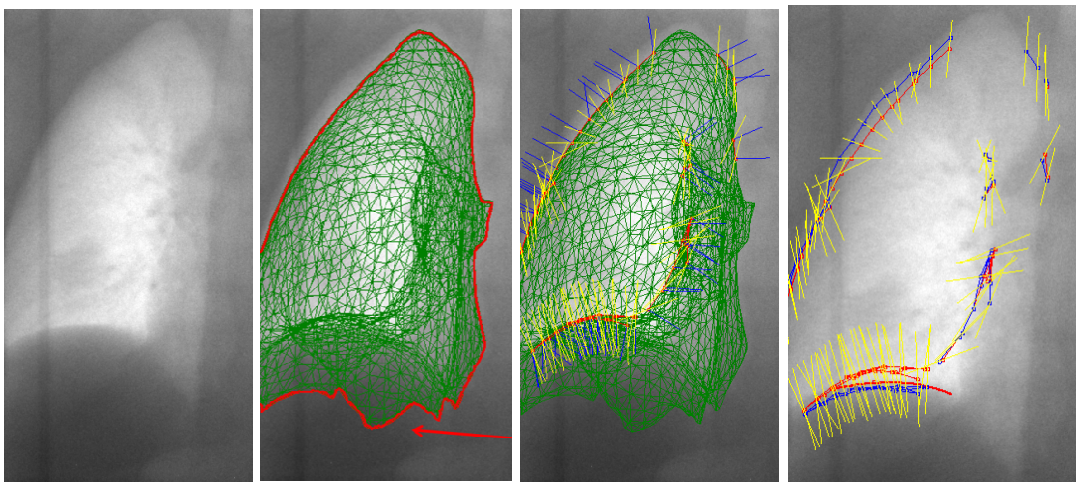

Figure 5-4: (a) Original MVCBCT projection image; (b) The projection of the initial lung mesh (green) and the silhouette contour (red). Note that the part of the contour at the bottom does not have corresponding strong gradient. (c) Projected initial lung mesh (green), detected candidate edge (red contour), projected motion direction (yellow line), projected normal direction (blue line); (d) original candidate edge (red), projected motion direction (yellow line), deformed candidate edge after optimal graph search (blue).

Instead of using the silhouette contour as our boundary when aligning the mesh with the projection image, we define a subset of mesh edges as candidate edges. A candidate edge is required to satisfy two conditions: (1) all the neighboring points should be on one side of the edge in the projection space; (2) the surface region near the edge should be smooth. The first criterion guarantees that the ray integral on two sides of the candidate edge is different. The second one ensures that the difference is large enough to produce a high contrast. The detected intensity of the projection images can be computed as a ray integral of the attenuation coefficients as a 3D volume: $I = I_0 e^{-\int \mu(r)dr}$. Since the attenuation coefficient of the lung is distinct from the surrounding tissue, the gradient in the CB projection is caused by the difference in the length of the beam that passes through the lung. Figure 5-5 compares three locations where an edge may exist. Due to large differences in the ray accumulation, the top two locations are likely to correspond to a strong gradient, while the bottom location may have a weak or even invisible gradient.

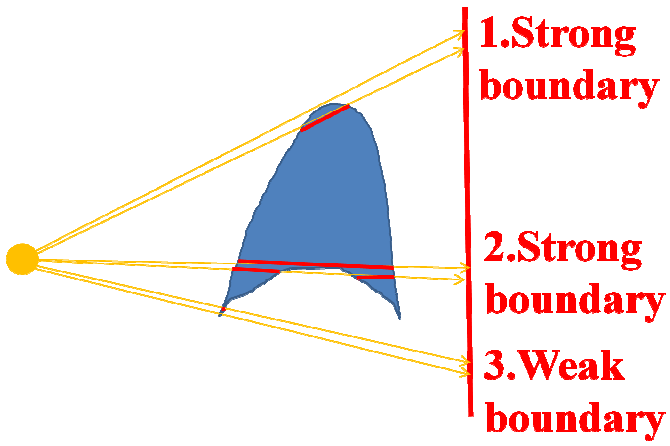

Figure 5-5: An illustration representing likely strong and weak boundaries. The top two locations produce distinctive differences, as marked by the red lines passing through the lung. The bottom boundary is very indistinctive with little difference visible around its intersections with the lung.

5.1.4 Multiple surface detection via optimal graph search

The multiple surface segmentation procedure follows the graph search framework which is presented in chapter 3. It should be further noted that there are three types of mesh points in any given phase of the constructed graph shown in Figure 3-3: non-candidate points, candidate points belonging to one candidate edge, and candidate points belonging to several candidate edges in different projections. It is the weight of the candidate points that contribute to surface detection and pulls the non-candidate point by smoothness constraints. For candidate points belonging to several candidate edges in different projections, the weight is a combination of image gradients in multiple MVCBCT projection images.

5.1.5 TPS interpolation

Figure 5-6 shows projection of the deformed mesh in four projection images after the optimal graph search. Figure 5-4d shows the deformed candidate edge in projection space. The deformed edges move toward locations with strong image gradients, such as the diaphragm and the lung wall.

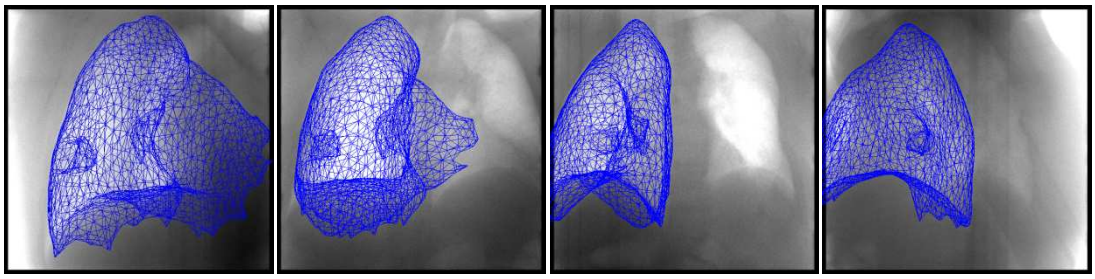

Figure 5-6: Deformed mesh after optimal graph search. (a) 0% inhale phase; (b) 50% inhale phase; (c) 100% inhale phase; (d) 50% exhale phase.

To generate the DVF, the displacements for all the voxels in the 3D volume need to be interpolated. The thin plate spline (TPS) interpolation algorithm (Bookstein, 1989) is used to generate a 3D DVF using the displacement of a known point set called "anchor points." The TPS interpolation aims to minimize the physical energy function as follows:

$$E = \sum_{i=1}^{k} \| f(x_i) - y_i \|^2 + \lambda \iint_{R^2} \left[\left(\frac{\partial^2 z}{\partial x^2}\right) + 2\left(\frac{\partial^2 z}{\partial x \partial y}\right) + \left(\frac{\partial^2 z}{\partial y^2}\right) \right] dxdy \quad (5\text{-}1)$$

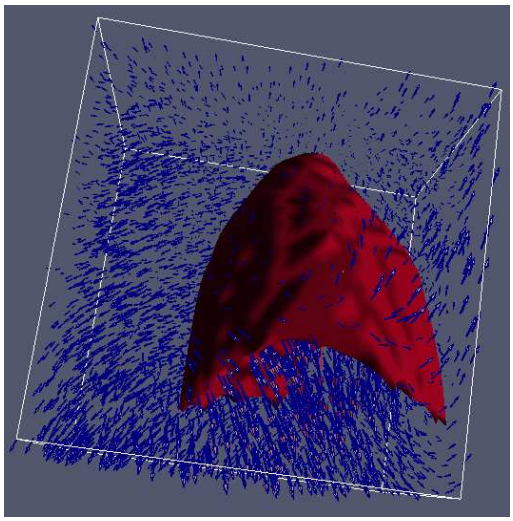

Figure 5-7: DVF from 0% inhale (FE) phase to 100% (FI) inhale phase. The mesh in 0% inhale phase is used as the reference phase

The first term of the algorithm represents the interpolation error of the anchor points while the second term represents the bending energy of the transformation of a "thin plate." The parameter λ is tuned appropriately to control the balance between the exact mapping of the anchor points and the rigidity of the deformation. For our purposes the anchor points are also the candidate points. Figure 5-7 shows the DVF from 0% inhale phase to 100% exhale phase. Two sets of images taken at FE and FI are reconstructed using the proposed approach. For the FE phase, the DVF is generated between the deformed mesh at 0% exhale which serves as the reference phase. For FI, the 100% inhale phase is used as the reference phase.

5.2 Experiments with the motion compensated approach

The MC reconstruction method is tested on the same 12 MVCBCT localization scans that were used in tumor segmentation approach. Again, those scans were taken

from three patients who have large NSCLC tumors (>10cm^3) in the bottom lobes of their lungs, which are visible in the projection images. A total of four sets of 4D planning CTs were used to generate the initial lung mesh model and provide a reference for evaluation. For the first two patients, one planning CT scan was taken several days prior to the treatment session. Two scans were captured for the third patient, since the tumor changed during the course of treatment and re-planning was required. For each 4DCT set, a 3D time sequence of volumes was acquired, representing ten different respiratory phases ranging from 0% to 100% on the inhale and exhale session. All the algorithms introduced in this study were implemented using our in-house software "MING DICOM".

5.2.1 Other MC reconstruction approaches for comparison

Three different methods are used in comparison to the proposed approach: RC FDK, MC FDK using the deformation of the 4D CT and MC FDK using the deformation of the RC MVCBCT. For the RC FDK, the projection images are sorted into two subsets (FE/FI) to reconstruct 3D volumetric images. The limited number of projection images (200 using the default setting) restricts image production in other respiratory phases, since fewer projections occur during the middle of inhalation or exhalation. The sorting of the projection images is based on the superior-inferior direction of the IHDA signal only, since the motion pattern differs in the middle of the inhale/exhale phases. Compared to phase-based sorting schemes, amplitude-based methods are able to control the residual motion by adjusting the gating window. The size of the gating window is a tradeoff between view-aliasing artifact and motion artifact. Based on our experience, at least 30 projection images are needed in each phase to produce a clinically meaningful image set. To include sufficient images, the width of the gating window ranges from 10%

to 25% for FE phase, and 20% to 40% for FI phase (We scale the maximum and minimum of the amplitude to 100% and 0% respectively).

The RC MVCBCT in the FE and FI phase is further used to generate two sets of 3D DVF (FE to FI, FI to FE) for the MC approach. Similar to the RC FDK method, two phases (one at FE and one at FI) of images are produced. DVF from FE to FI are used to reconstruct the images during the FE phase, while DVF from FI to FE are used to reconstruct the images for the inhale phase. During the reconstruction, the DVF is interpolated for CB projections that belong to intermediate phases.

Since there are more than 10 phases of images in one 4D CT set, a 4D DVF is generated using the image of each phase with respect to a reference phase. The DVF is converted into cone beam coordinates using the transformation information derived during the alignment of the two images (see Figure 5-3a, b). Interpolation of DVF for intermediate phases is also needed.

5.2.2 Reconstructed images

Figure 5-8 shows the results of MVCBCT at FE phase using the various approaches discussed in this paper. It is evident that for the FDK without MC (row a), strong motion artifacts in both tumor and diaphragm are visible. For RC reconstruction (row b), the motion artifact is greatly reduced, however there are still strong view-aliasing artifacts (the streaking and banding). For the MC methods (rows c to e), the motion is reduced without introducing aliasing artifacts.

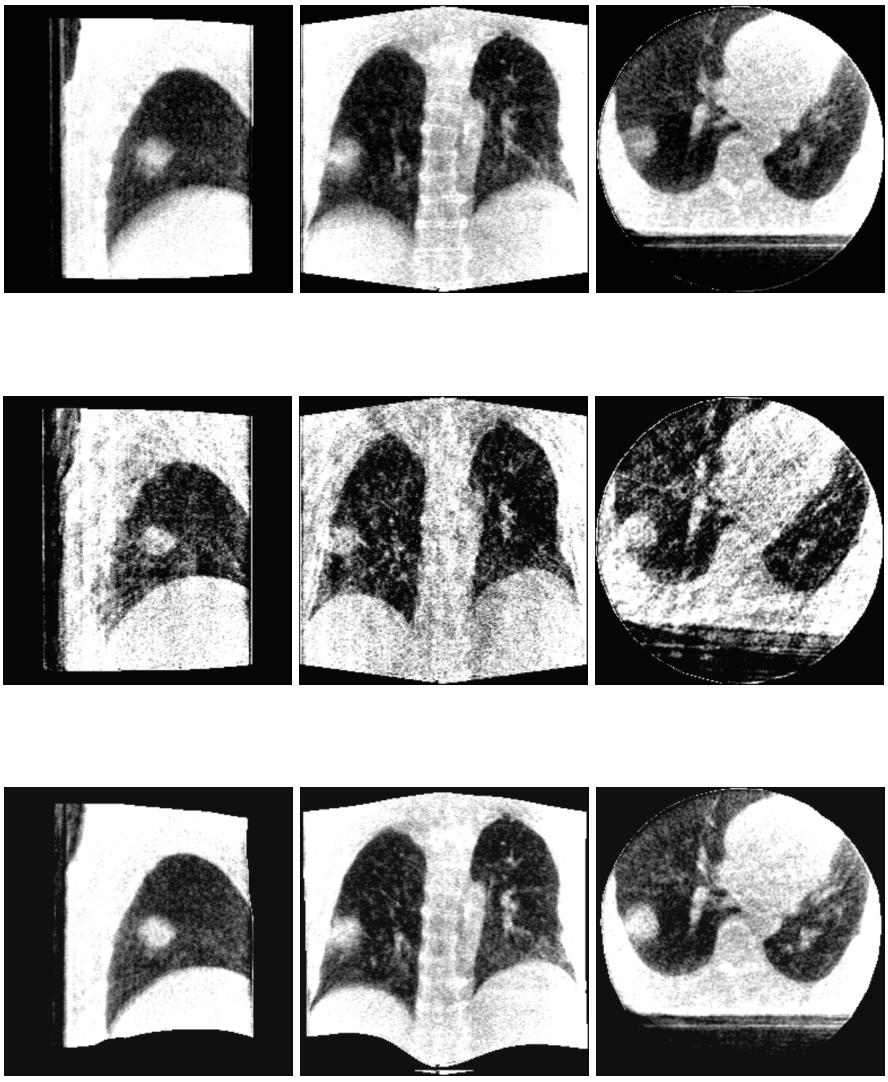

Figure 5-8: Reconstructed MVCBCT at the FE phase for one patient using different approaches. From left to right are the images of sagittal, coronal and axial views, respectively. (a) Conventional FDK using all the projection images; (b) RC reconstruction; (c) Motion compensated using 4D CT; (d) Motion compensated using RC MVCBCT; (e) The new approach.

(d)

(e)

Figure 5-8 continued

Figure 5-9 shows a single profile aligned in a superior-inferior direction passing through the tumor. It is evident that the edge of the tumor and the diaphragm is much smoother in Figure 5-9a, showing obvious motion artifacts. For both the RC reconstruction and the proposed approach, the edge becomes much steeper. Some features generated using the 4D CT approach (Figure 5-9b) are preserved in the image reconstructed using the proposed approach (Figure 5-9c): the two small peaks located between the tumor and the lung wall are particularly noteworthy. The difference in the location of the edges between the reconstructed MVCBCT and the 4D CT, is due to the different respiratory sorting techniques applied for the reconstruction. Further differences were introduced due to the change of motion that occurred between the planning time and the treatment time.

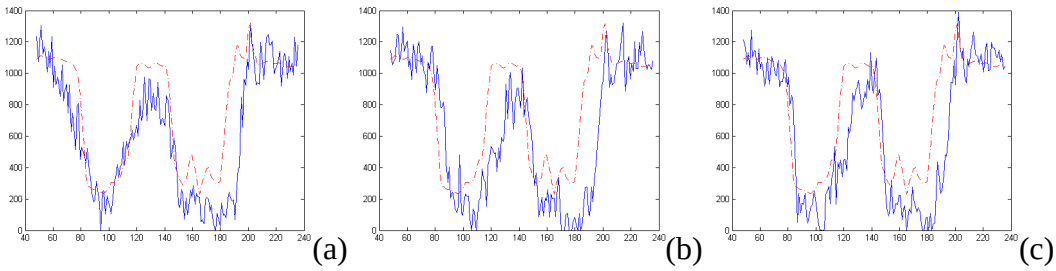

Figure 5-9: Profile of reconstructed MVCBCT (blue) and 4D CT (red) along superior-inferior direction (x-axis is superior-inferior direction in physical coordinate, y-axis is the CT number). (a) Conventional FDK; (b) RC reconstruction; (c) proposed approach. The difference in edge location is due to the change in motion pattern between planning CT and CBCT.

5.2.3 Volume measurement accuracy

Several metrics are used to evaluate the target localization and image quality of the reconstructed image. First, the accuracy of tumor volumetric measurement is tested on data derived from 12 MVCBCT scans. For images with poor quality, such as RC FDK, there would be a very large variance of manually annotated contours of the tumor by different physicians. The edge of the tumor is sometimes difficult to define on these images. To minimize inter-observer variability, a semi-automatic approach is implemented to segment the tumor and quantify the tumor size. The algorithm starts with a user-defined region of interest (ROI) in the 3D volume. The Otsu threshold (Otsu, 1975) and connected region labeling is used to segment the tumor within the ROI. Since the data provided by the CT scans of the tumor and the surrounding soft tissue inside the lung differs greatly, the Otsu threshold tries to find the optimal threshold that minimizes the intra-variance of the two separating classes. The tumor volume calculated from the planning 4D CT is used as ground truth and the relative error is computed as follows:

$$Relative\ Volume\ \ Error = \frac{|V_{4DCT} - V_{MVCBCT}|}{V_{4DCT}} \tag{5-2}$$

Figure 5-10 shows the relative error of tumor quantification of 12 MVCBCT daily localization scans. To reduce errors that may occur due to any change in tumor volume between the planning CT and the treatment/localization CT, we also analyze four MVCBCT scans taken closest to the planning day for each patient. The time period between the planning CT and MVCBCT scan is less than 6 days and there is no radiation therapy during this intermission. These images are marked with asterisks in Figure 5-10. According to a study on tumor growth conducted by Arai *et al*, a large cell carcinoma has a doubling time of 67.5 days, which is the most aggressive type of NSCLC (Arai et al., 1994). Based on the linear growth and exponential growth models, the growth rate for a six-day time period can be estimated to be 8.9% and 6% respectively, which can be considered as upper bound. Table 5-1 and Table 5-2 show that MC reconstruction based on 4D CT scans and the proposed method have better tumor quantification accuracy than the other two approaches (RC MVCBCT, MC reconstruction using DVF computed from 4D CT, MC reconstruction using DVF computed from RC MVCBCT is abbreviated for "RC", "MC-4DCT", "MC-CBCT" respectively).

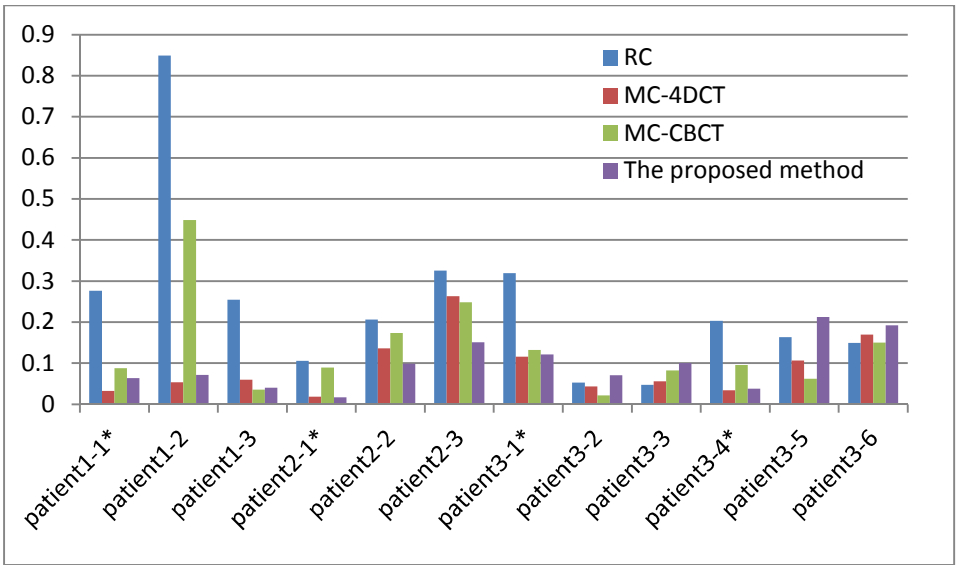

Figure 5-10: Relative error of tumor volume quantification in 12 MVCBCT images. The bars with an asterisk represent the first MVCBCT scan after the 4D planning CT which is used as ground truth

Relative Error	RC	MC-4DCT	MC-CBCT	Proposed Method
FE phase	27.71%±22.4%	7.10%±7.52%	12.15%±9.77%	7.78±7.10%
FI phase	21.47%±22.1%	11.00%±7.37%	14.93%±14.83%	11.81±6.68%

Table 5-1: Overall relative error of volume measurement.

Relative Error	RC	MC-4DCT	MC-CBCT	Proposed Method
FE phase	22.76%±12.65%	3.38%±3.46%	9.26%±4.64%	3.39±3.64%
FI phase	22.42%±10.02%	6.60%±6.03%	10.94%±7.54%	8.57±8.31%

Table 5-2: Overall relative error for the 4 MVCBCT scans close to planning day.

5.2.4 Motion measurement accuracy

Motion measurement accuracy is another important clinical parameter in radiotherapy. In this study the motion of IHDA positions from FE to FI is manually identified, which has a very small inter-observer variability. The displacement of the IHDA in the superior-inferior (SI) direction is compared to the average peak-to-valley IHDA motion in the SI direction during the cone beam scan. This is considered as ground truth. The SI direction of motion of the IHDA is automatically determined from the 2D projection images using the method introduced in chapter 2. Similar to volume measurement, a relative error is used:

$$Relative\ \ Motion\ \ Error = \frac{\left| M_{4DCT} - M_{MVCBCT} \right|}{M_{4DCT}} \tag{5-3}$$

Figure 5-11 shows the relative error for 12 patients. The overall accuracy for the four methods is shown in Table 5-3, where the RC reconstruction method and the proposed method have greater accuracy than both the MC-4DCT and the MC-CBCT. Motion correction based on 4D CT reveals the largest error which is mainly due to the inconsistency of the motion pattern between the planning session and the localization session.

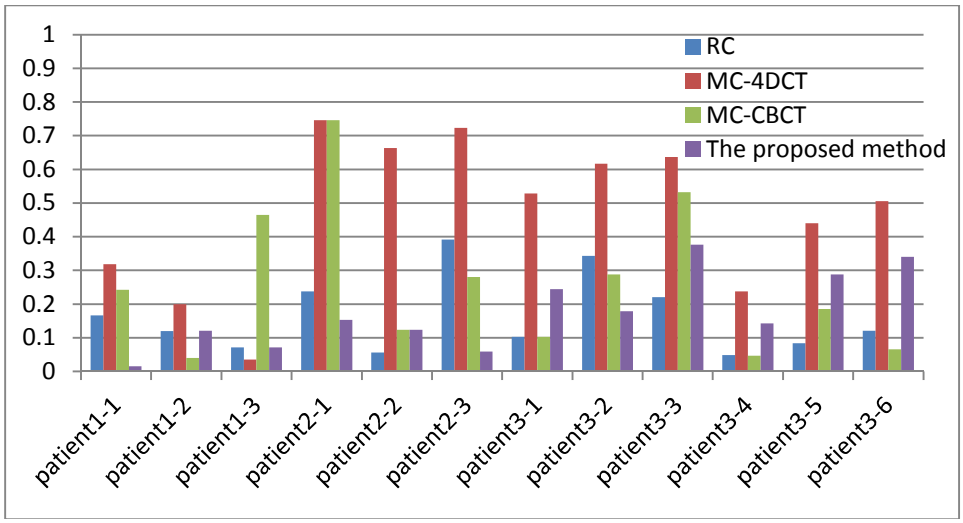

Figure 5-11: Relative error of IHDA motion quantification in 12 MVCBCT images

Reconstruction method	RC	MC-4DCT	MC-CBCT	Proposed method
Relative error	16.36%±11.27%	47.09%±22.78%	26.00%±22.02%	17.62±11.38%

Table 5-3: Overall relative error for IHDA motion

5.2.5 Image quality measurement

Contrast to noise ratio (CNR) is a simple and objective measure of the detectability of certain structures with uniform intensity. In this study it is used to assess the image quality in the tumor and diaphragm region based on the following formula:

$$CNR = \frac{\left| I_{object} - I_{background} \right|}{\sigma_{object}} \tag{5-4}$$

where I and σ are the mean and standard deviation within the object (tumor or diaphragm) or background. The segmentation of the tumor and the diaphragm is based on

the same approach that is used for tumor volume measurement. The results of CNR are shown in Table 5-4, where it is evident that 4D CT has significantly better CNR than MVCBCT, and RC CBCT has smallest CNR value. CNR of the proposed method is slightly better than the other three approaches.

Location	4D CT	RC-CBCT	MC-4D CT	MC-CBCT	MC-mesh
Tumor FE	6.33±2.44	2.37±0.30	3.51±0.35	3.42±0.40	3.85±0.42
Tumor FI	6.81±2.72	2.30±0.29	3.51±0.46	3.34±0.50	3.58±0.33
Diaphragm FE	12.36±4.96	2.37±0.45	3.32±0.85	2.93±0.81	3.53±1.06
Diaphragm FI	11.00±4.20	2.50±0.38	3.29±0.78	3.08±0.82	3.40±0.93

Table 5-4: CNR in different regions using different reconstruction approaches

5.3 Discussions and conclusions for the new MC approach

In this study, we developed a novel MC reconstruction approach for daily MVCBCT localization. The method is based on deforming the lung mesh using the image information provided by 2D cone beam projections. Our approach has the best overall performance among the four approaches compared. It has the second best accuracy in both tumor volume measurement and diaphragm motion measurement. MC using 4D CT is slightly better than the proposed approach in tumor volume measurement, but more inaccurate in diaphragm motion measurement. RC FDK has slightly better accuracy in motion measurement, but its performance in tumor volume measurement and CNR is the worst among the four. For CNR, the proposed method is the best among the four methods.

There are several advantages of the proposed approach. First, generating a DVF based on 2D projection images is more accurate than using the 4D CT and RC CBCT. This comparison formed the basis of a previous study. (T. Li et al., 2007). RC CBCT contains severe aliasing artifacts, which cause inaccuracies in the 4D DVF during

registration. This is well illustrated by our results of the motion measurement error; RC FDK has the best accuracy among the four, but MC using those RC CBCT images is more error-prone. Conversely, the reproducibility of the deformation during the 4D planning CT is not reliable on the MVCBCT scan, as seen in the motion quantification result. The MC reconstruction using DVF from 4D CT has up to 47% relative error in motion quantification. The IHDA motion between 0% and 100% exhale of the 4D CT is also quantified, which is much smaller than the average peak to valley IHDA motion extracted from CB projections. In one case the IHDA motion in 4D CT was 8 mm, while the average IHDA motion in one MVCBCT scan was up to 22 mm. Apart from the change in motion amplitude, another possible reason to account for this inconsistency is that the respiratory signal used during 4D CT acquisition is relative phase based. The proposed method, on the other hand, utilizes the absolute 3D IHDA position as the respiratory signal. The deformation of the projected mesh points in 2D space can be accurately back-projected to 3D space using the projection matrix of the cone beam system.

Second, the proposed approach can be used “on-the-fly” in cases where the estimation and compensation of the respiratory motion during the acquisition of CB projections is needed. Although manual editing of the initial lung model derived from the 4D CT is required, these procedures can be accomplished right after the acquisition of the planning CT. To further improve efficiency, the manual alignment correction may be replaced with available commercial registration software. For MC reconstruction using the proposed method, the deformation, DVF interpolation and MC reconstruction are fully automated. The proposed approach obviates the protracted need of forward projection registration required by the image-space to projection-space registration method (T. Li et al., 2007). Calculation times for the deformed mesh computation via optimal graph search take about a minute using an Intel (R) Core (TM) i-7 2620M CPU with 4GB RAM. Generating a DVF using the same processor takes about five minutes,

although calculation times may be reduced through the use of a computationally light interpolation technique.

Though free of reconstruction artifacts, 2D CB images contain a lot of noise due to MV photon scatter (Figure 5-4). There are confounding edges that lead the mesh deformation towards the wrong locations in projection space. The proposed method consists of two components to avoid those edges. First, the use of the dot product between the vector of the projected normal direction and the gradient can eliminate the indistinct edges with the gradient where it is not conforming to the desired direction. The second one is the use of the smoothness and inter-phase constraints as used in the optimal graph search method, where the motion of one mesh point in one respiratory phase is limited by the position of its neighboring point and its neighboring phase.

The primary source of inaccuracy in the proposed approach is the location of the lung in some of the CB projection images. Among the image sets that we used, the whole lung is visible in only one CB projection set. The portion of the lung needed to determine the CBCT volume is located outside of the field of view on the two remaining image sets. In cases where the lower part of the diaphragm is located outside of the image, the algorithm has difficulty in detecting the candidate edges, which may explain why the motion error is greater for two of the patients.

All three patients used in this study had large NSCLC tumors (>10cm^3). Large tumors also form a part of the initial lung mesh so that the candidate edges that delineate the tumor in CB projections can guide the tumor deformation during DVF estimation. However, there might be no candidate edge for a small tumor in the projection space. The tumor deformation has to rely on the interpolation from the deformed lung mesh only, which may not represent the real tumor deformation and for this reason there may be no candidate edges for small tumors. Future studies will focus on patients with tumors of varying sizes in more locations. The accuracy of mesh deformation will also be evaluated in the projection space.

Overall, compared with three traditional methods, the new method which is presented in this chapter shows superior target localization accuracy and image quality. This improvement is achieved by utilizing the 2D MVCBCT projections for both DVF generation and MC reconstruction.

CHAPTER 6

ENHANCEMENT OF PROJECTION IMAGES VIA BACKGROUND SUBTRACTION

In the previous chapters, we have discussed the advantages and current technical limitations of MVCBCT. We have presented several new approaches that try to reduce the inaccuracies brought by using strain gauge with the MVCBCT system, including direct IHDA and tumor detection from 2D projection images, RC reconstruction, and the motion compensated reconstruction approach. Ideally, it would be desirable if the tumor position could be detected accurately and robustly from 2D projection images. However, the presented tumor segmentation technique (shown in chapter 3) is more suitable for large tumors. Detection of small tumors is limited by low image contrast and confounding objects. The strain gauge calibration relying on 3D RC or MC reconstruction approach is based on the linear relationship assumption between IHDA and tumor motion. The DTMR quantified from the FE phase and the FI phase can be considered the average value of the 200 projection images.

In this chapter, we will present a new enhancement framework that tries to improve the visualization effect of MVCBCT projection images. Similar to IHDA or tumor detection presented in chapter 2 and 3, the enhancement framework is also based on using the projection images of MVCBCT as a concept of "cine" mode to observe the intra-fractional motion, as they provide a high temporal resolution (about 0.3 s for each frame). The MVCBCT projection images can be considered as rotational fluoroscopic video, which can be used for visual guidance in many interventional procedures, such as the angiographic C-arm system for real-time cardiac and vessel imaging (Cusma, Bell, Wondrow, Taubel, & Holmes, 1999; Fahrig, Fox, Lownie, & Holdsworth, 1997; Orth, Wallace, & Kuo, 2008). However, the major limitations of using cone beam projection

images for visual guidance is the scattering of beam photons and lacking depth information, which are prevalent in all the previous applications. The organ of interest (OOI), such as the left ventricle for cardiac imaging, or the diaphragm and the tumor for lung imaging, is often superimposed with other anatomical structures, making it less distinguishable from the surrounding tissues, which is illustrated in Figure 6-1 for several examples. The overlapping with non-interest organs limits the use of projection images for accurate localization and segmentation of OOI. It would be desirable if the accumulation of the ray integral of those non-interest tissues (background) can be avoided, thus removing the confounding regions for better visualization.

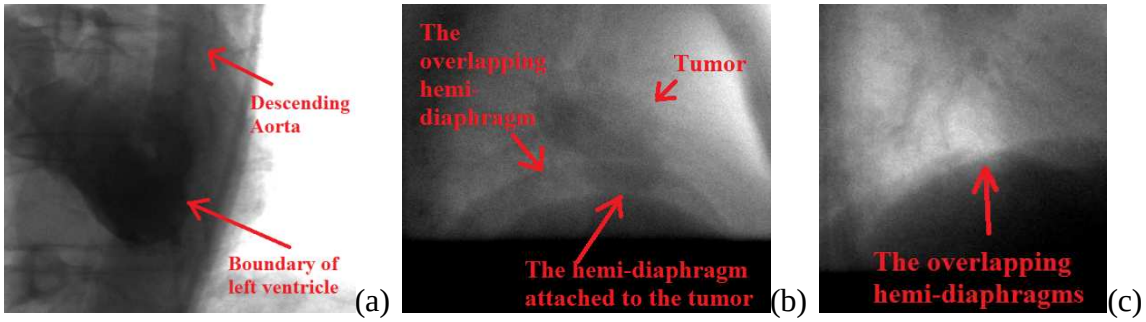

Figure 6-1: Examples of some cone beam projection images which have significant overlapping organs: (a) C-arm angiography of left ventricular area. The left ventricle is overlapped with descending aorta; (b) MVCBCT projection images of lung with NSCLC. The tumor and the hemi-diaphragm overlapped with the contra-lateral hemi-diaphragm; (c) The overlapping of the contra-lateral hemi-diaphragms.

The enhancement framework is based on avoiding the ray integral of non-interest tissues to derive the enhanced projection images for MVCBCT. The method is tested on both phantom images and NSCLC patient images. Two schemes were applied to derive the enhanced OOI. The first approach removes all the non-interest tissues (background) in the 3D volume and projects the remaining OOI onto the projection space. The second

approach removes the OOI in the 3D volume and projects all the background information on the projection space. The projected background image is used to subtract from the original projection image. This method is similar to the principle of digital subtraction angiography (DSA) (Brody, 1982), which is created by subtracting the imaging data before and after the administration of a contrast agent. Zhang et.al. proposed a method to remove the background information for projection images of kilo-voltage (KV) CT (J. Zhang, Yi, Lasio, Suntharalingam, & Yu, 2009). However, they only isolated a slice of interest from the KV image and the enhanced projection image only contains organ information of one specific slice. Our study is distinguished in three aspects. Firstly, we isolate the whole OOI to enhance the projection image, rather than a single slice of the volume. Secondly, we compare the direct projection and background subtraction approach in terms of image quality and 2D organ detection accuracy. Both pros and cons of the two methods are presented. Thirdly, we incorporate RC reconstruction into the OOI enhancement framework, which is proved to be more suitable for imaging areas containing respiratory motion.

This chapter is organized as follows. Section 1 introduces the details of the enhancement framework and the imaging data used for validation. Section 2 shows the result of the validation on different metrics with a discussion section. Section 3 concludes with a potential range of applications of the method.

6.1 The enhancement framework

6.1.1 The general principles

The electrical portal imaging device (EPID) of MVCBCT is a flat panel detector receiving attenuated X-ray from the beam source. The detected intensity of projection angle θ at pixel location (u, v) is given by:

$$I(u,v,\theta) = I_0(\theta)e^{-P(u,v,\theta)}[1+SPR(u,v,\theta)]$$

(6-1)

where $I_0(\theta)$ is the mean detector intensity for a non-attenuated X-ray beam at projection angle θ. This factor varies with exposure and cannot be measured with an object in the X-ray field. It is represented as a function of θ since small variation occurs in different projection angles. The detected intensity is composed of the primary beam and scattered radiation. The scattered radiation deviates from the straight line path between the X-ray beam and the image detector, which is a major source of image degradation. Here SPR is the scatter-to-noise ratio (Joseph & Spital, 1982). $P(u,v,\theta)$ is the primary beam attenuation, which is equal to the line integral of the linear attenuation coefficient along the ray direction:

$$P(u,v,t) = \int_{r\in L} \mu(\vec{r})d\vec{r}$$

(6-2)

The line integral along L of 3D tomographic image can be divided into OOI region L_o and non-OOI (background) region L_b:

$$P(u,v,\theta) = P_o(u,v,\theta) + P_b(u,v,\theta) = \int_{r\in L_o} \mu(\vec{r})d\vec{r} + \int_{r\in L_b} \mu(\vec{r})d\vec{r}$$

(6-3)

Combining Equation (6-1) and (6-3), we can derive

$$I(u,v,\theta) = I_0(\theta)e^{Po(u,v,\theta)}e^{Pb(u,v,\theta)}[1+SPR(u,v,\theta)]$$

(6-4)

As mentioned earlier, two schemes are experimented in this study to derive an OOI-enhanced projection image. The first approach is to remove all the non-OOI regions in the volume and project the OOI part onto the 2D space, generating an image with the detected intensity as:

$$I_{OOI}(u,v,\theta) = I_0(\theta)e^{P_o'(u,v,\theta)},$$

(6-5)

where the derived new intensity is represented as I_{OOI}. Here we use P_o' instead of P_o, since Po' is the line integral of OOI region using the attenuation coefficients of the reconstructed volume, which is different from the real coefficients of the patient anatomy to some degree.

The second approach projects the non-OOI regions onto the 2D space and subtract from the original image, deriving a new background-subtracted image I_{BS}.

$$I_{BS}(u,v,\theta) = I_0(\theta)P_o(u,v,\theta)P_b(u,v,\theta)[1+SPR(u,v,\theta)] - I_0(\theta)P_b'(u,v,\theta)$$

(6-6)

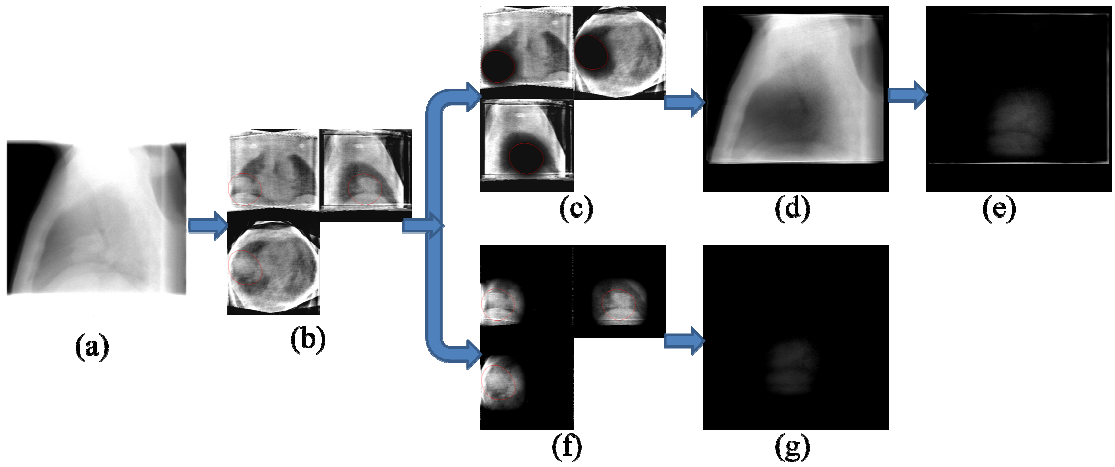

Figure 6-2: Intermediate results of the proposed method: (a) One original projection image with the pixel value shown as accumulated attenuation coefficients; (b) RC reconstructed volume based on SART; (c) Volumetric image with OOI removed; (d) Reprojection of volume (c); (e) subtraction of (a) & (d); (f) Volumetric image with non-OOI region removed; (g) Reprojection of volume (f).

Similar to Equation (6-5), P_b' is used to represent the line integral of the reconstructed attenuated coefficients, which is different from the real coefficients of the

patient anatomy (P_b). Figure 6-2 shows the workflow of the proposed method, with the intermediate results for each step. The OOI can be any organs or tissues the clinicians with to get better visualization in the 2D projection images. In this example the OOI is the lung containing the tumor mass.

6.1.2 Numerical projection based on SART

The image reconstruction of the unprocessed volume is based on simultaneous algebraic reconstruction technique (SART) (Andersen & Kak, 1984). The computation of the ray integral based on image reconstructed by SART algorithm is inherently more authentic than that of Feldkamp algorithm (Feldkamp et al., 1984), since it makes the integral of the projection ray converge to the detected intensity of the 2D projection data during the iterations. This feature enables the algorithm to generate the numerically projected image close to the original detected intensity. Compared to ART, on the other hand, SART has no stripping nor aliasing artifact (Mueller, Yagel, & Wheller, 1999a), which is more suitable for cone beam reconstruction. SART updates the linear attenuation coefficient of each voxel by the following equation:

$$vjk = v_j^{k-1} + \lambda \frac{\sum_{\rho_i \in P_\theta} \frac{(pi - \sum_{n=1}^{N} w_{in} v_n^{k-1})}{\sum_{n=1}^{N} w_{in}} w_{ij}}{\sum_{\rho_i \in P_\theta} w_{ij}} \tag{6-7}$$

The equation shows how to update the *j*th voxel from *(k-1)*th iteration to *k*th iteration. The numerator of the correction term on the right is the difference between the original pixel value p_i and the numerically projected value, which is the line integral

along the path of the X-ray. The correction term depends on a weighted average of all rays of projection P_θ that traverse the voxel j, where θ denotes the projection angle.

To compute each voxel's contribution $w_{ij}v_j$ to P_i in Equation (6-7), an interpolation kernel h is used for the continuous volume representation:

$$f(x,y,z) = \sum_{n_x}\sum_{n_y}\sum_{n_z} f(n_x,n_y,n_z)h(x-n_x,y-n_y,z-n_z),$$

(6-8)

where x, y, z and n_x, n_y, n_z is the continuous and discrete Cartesian coordinate representation of the volumetric image, respectively. Among various choices of h, we use a kernel based on the Kaiser-Bessel window, which has many good features, such as fast decay for frequencies past the Nyquist rate and radial symmetry (Mueller, Yagel, & Wheller, 1999a). The line integral as a function of distance to the voxel center is pre-computed analytically into a kernel-footprint (Mueller, Yagel, & Wheller, 1999b). During the re-projection and back-projection process of SART, only the distance between the voxel center and the ray needs to be computed. Generally, a ray passing through the volume can be represented as:

$$\vec{x}(t) = \vec{s} + \vec{d}t$$

(6-9)

where s is the position of the X-ray source in room coordinate at one orientation angle. d is an R3 direction vector of the ray, which is usually normalized. t is a parameter indicating the distance to the beam source. Different from diagnostic CT system, many cone beam system is dependent on a 3×4 matrix **P** for each projection angle to accurately define the 3D-to-2D projection. Given a 3D point in room coordinate $\boldsymbol{v_3}=\{x,y,z,w_3\}$, its corresponding 2D projection location $\boldsymbol{v_2}=\{u,v,w_2\}$ can be defined by $\boldsymbol{v_2}=\mathbf{P}\cdot\boldsymbol{v_3}$, where $\boldsymbol{v_3}$ and $\boldsymbol{v_2}$ are both represented as homogeneous coordinate. The projection matrix can also be used to determine the beam source position.

$$\vec{s} = -P_3^{-1} p_4$$

(6-10)

Where P_3 is the matrix containing the first three columns of **P** and p_4 is the fourth column. The direction vector d can be computed from 2D projected position $[u,v]$.

$$\vec{d} = -P_3^{-1} p^+$$

(6-11)

where $p^+ = [u,v,1]^T$. The distance between the voxel center and the ray can be computed as:

$$\|r\| = \left\|\vec{d} \times (\vec{s} - \overrightarrow{v_j})\right\|$$

(6-12)

Here v_j is the jth voxel's center position.

The proposed method based on SART can be applied based on either standard reconstruction or RC reconstruction approach, where only a subset of projection images are selected and backprojected to 3D volume in the latter case.

6.2 Verification of enhancement framework

The proposed method was tested on the imaging phantom, which was described in details in section. Similar to previous introduced phantom experiment (chapter 3 and 4), the predefined motion and the size of the phantom inserts are used to serve as ground truth for the evaluation. The OOI enhancement technique is based on RC SART reconstruction for scans with motion. The predefined motion function of the phantom is used to provide the respiratory signal for the RC reconstruction. The projection images are divided into 8 equally spaced respiratory bins based on the amplitude of the motion.

Projection images belonging to the same respiratory bin are used to reconstruct a RC 3D volume, which is further used for OOI enhancement

The method was also tested on 11 MVCBCT scans from 6 patients due to the limited hardware resources for computation. The OOI enhancement is performed on the diaphragm region. The patient scans used an imaging dose of 10MU. The number that one scan covers for patient respiratory cycle ranges from 6 to 20 in our study. The respiratory signal used for RC reconstruction is based on the 3D position of ipsi-lateral hemi-diaphragm apex (IHDA), where it can be extracted from projection images using the detection algorithm introduced in chapter 2. Manual correction is made after the automatic detection to guarantee that there is no clinically significant error of IHDA position. Similar to phantom study, the RC reconstruction is based on 8 respiratory bins respectively to evaluate the influence of the residual motion to the image quality.

As discussed in chapter 4, the RC reconstruction contains residual motion. Sometimes the tumor is attached to the peripheral organs, which have very similar attenuation coefficients with tumor. These factors make accurate delineation of the tumor boundary hard to achieve. Though we could choose the tumor as OOI, it is difficult to measure the performance of the enhancement without a convincing ground truth of the tumor boundary. Instead, the diaphragm area is chosen as OOI for patient images, since the diaphragm in 2D projections has strong contrast and is able to be recognized in most cases.

6.2.1 Derived enhanced images

Figure 6-3 and Figure 6-4 shows the result of enhanced projection image of the phantom and the patient, respectively. The subfigure a, b, c and d are the original image, projected background image, background-subtracted image and projected OOI image,

respectively. The spherical inserts and the diaphragm are chosen to be the OOI region for phantom images and patient images, respectively.

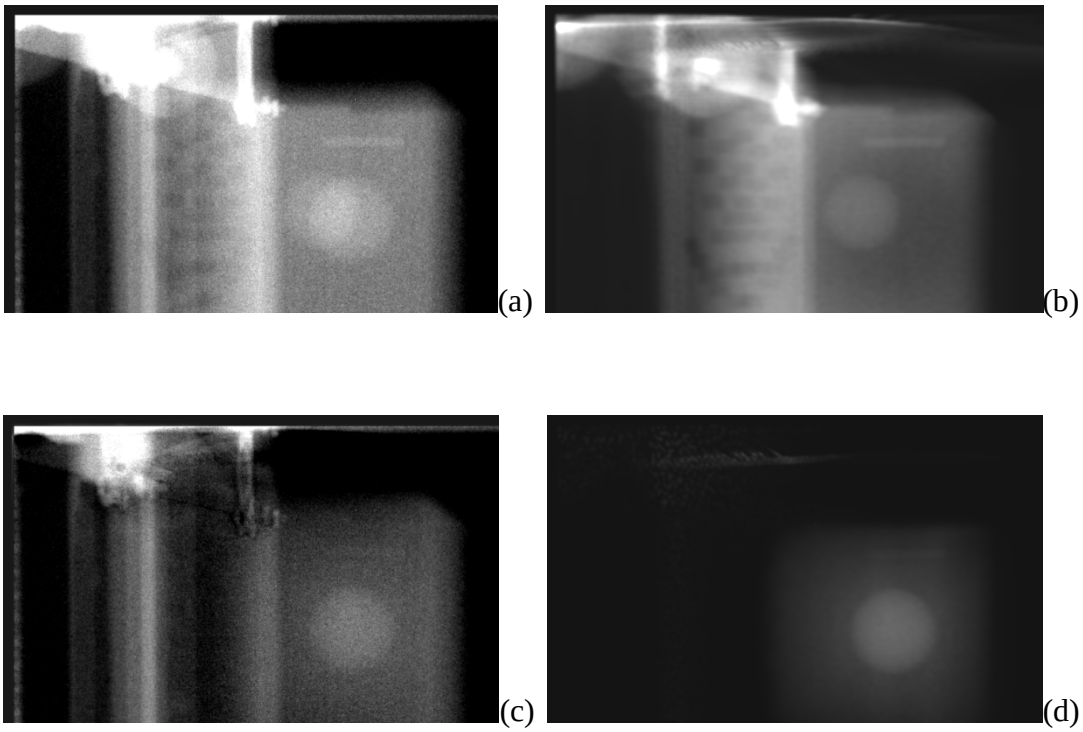

Figure 6-3: One frame of OOI enhanced beam attenuation image of static phantom under 5MU MVCBCT scan. The largest spherical insert is chosen as OOI in this example. (a) The original image; (b) projected image of non-OOI (background) region; (c) subtracted image; (d) projected image of OOI region. All the images are displayed using the same level and window.

In Figure 6-3 it can be seen that the overlap of the two spherical inserts that originally exists in the un-processed image disappears. In Figure 6-4 the overlapping diaphragm originally exists in the unprocessed image disappears in both images of direct OOI projection and background subtraction. Figure 6-5 shows the intensity of the four images in Figure 6-3 along the profile that traverse horizontally through the center of the largest sphere. It can be found that the projected OOI or projected background image has

less noise than the other two images. It is consistent with Equation (6-5) and Equation (6-6), where only background-subtracted image contains SPR term. The numerical projection of either the OOI or the background is free of scattered radiation.

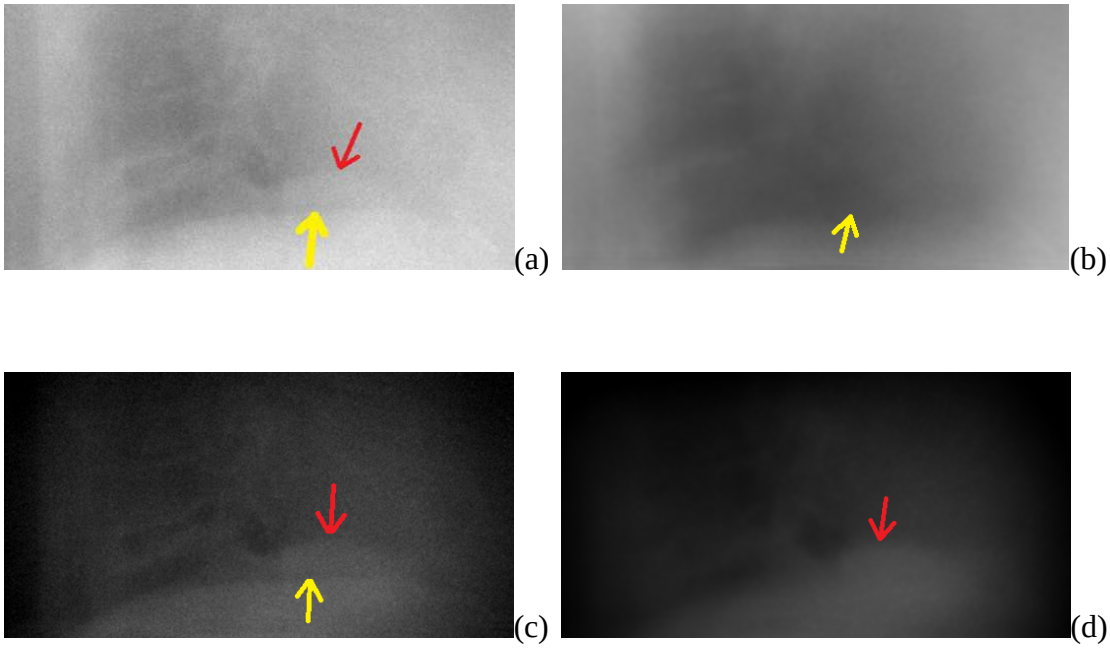

Figure 6-4: One frame of OOI enhanced beam attenuation image of patient under 10MU MVCBCT scan. (a) The original image; (b) projected image of non-OOI (background) region; (c) subtracted image; (d) projected image of OOI region. All the images are displayed using the same level and window. The red arrows points to the desired hemi-diaphragm. The yellow arrow points to CLHD. Note how the gradient becomes relatively stronger than the CLHD in the enhanced images.

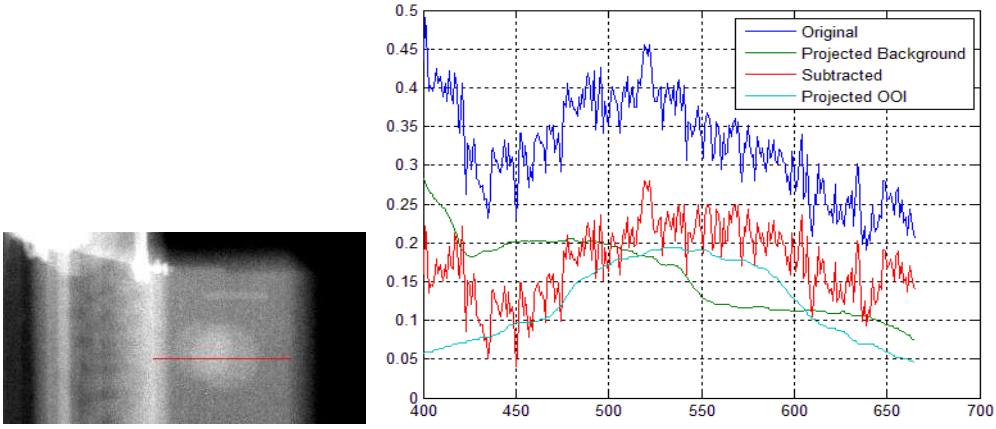

Figure 6-5: The pixel intensity of the four images along the profile shown in the left.

6.2.2 Image quality measurement based on CNR

Different metrics were employed to evaluate the outcome of the OOI-enhanced approach. Firstly, we explore the intensity change along the profiles in both unprocessed and enhanced images. The contrast-to-noise ratio (CNR), which is a simple and objective measure of the detectability of certain structures with uniform intensity, is used to measure the profiles of the interested regions. For phantom studies, we investigate the CNR along profiles that are perpendicular to the 2D boundary of the spherical inserts. Since the size and the motion of the phantom inserts are predefined, the 2D boundary can be derived based on 3D-to-2D projection of the 3D shape

For patient studies, the 2D IHDA position is manually identified in all the projection images. Two rectangular regions, which are located superior and inferior to the IHDA, are selected to measure the CNR in the diaphragm region. CNR is defined as follow:

$$CNR = \frac{I_1 - I_2}{\sqrt{\sigma_1 + \sigma_2}} \qquad (6\text{-}13)$$

where I and σ represents the average and standard deviation of the profile intensities. The subscript "*1*" and "*2*" represents the two regions used to quantify CNR. For phantom images they are the regions that locate inside and outside the boundary of spherical insert, while for patient images they are the regions that locate superior and inferior to IHDA.

Figure 6-6 compares the CNR quantified from original (unprocessed) images, OOI projected images (obj_reproj), and background subtracted images (bkg_sub), respectively on the five larger spherical inserts. The column and the error bar show the average and the standard deviation of CNR over 200 projection images, respectively. There is significant improvement (two to three fold, generally) by using direct OOI projection approach, while background subtraction approach improves the CNR slightly. The average improvement of the direct projection approach is 365% and 238% for static and motion scan, respectively, while the background subtraction approach achieves 21.4% and 13.8%.

Generally, the static scan has much better CNR than the scan with motion, since residual motion exists during the image acquisition of each projection image, which blurs the object boundary. The names of "sphere 1" to "sphere 5" is in the order from the largest inserts to the smallest one, thus the improvement by background subtraction method decreases as the object size decreases. It is probably due to that as the object size decreases, the limit of the MVCBCT hardware, such as the resolution of 3D volume and the scattered noise becomes more detrimental to the background subtraction method.

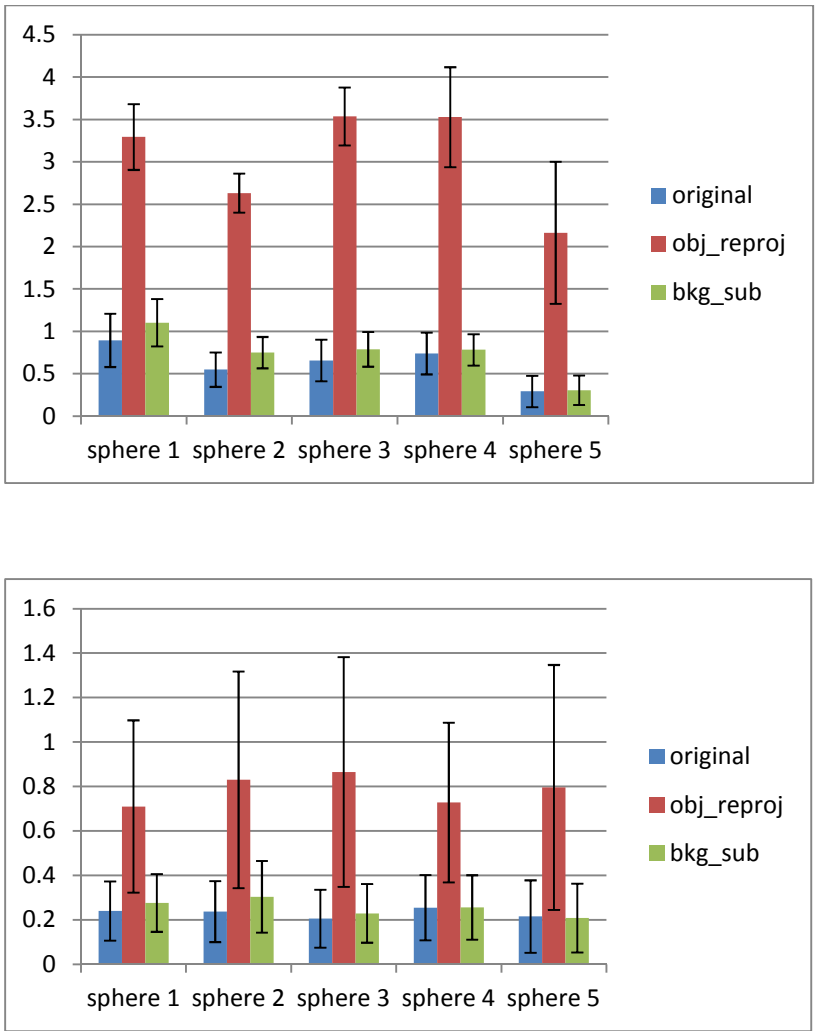

Figure 6-6: Average and standard deviation of CNR over 200 projection images of the five larger spherical inserts of the phantom. Top: static scan; Bottom: scan with predefined motion.

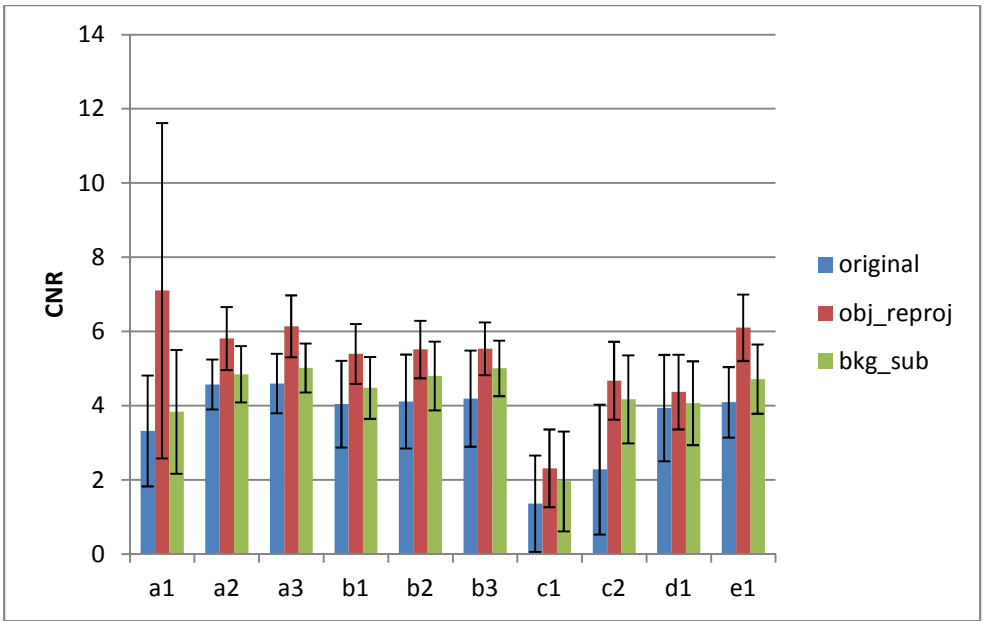

Figure 6-7: Average and standard deviation of CNR of diaphragm region of 10 MVCBCT scans from 5 patients.

Figure 6-7: shows the CNR of diaphragm region from 10 MVCBCT scans. Both enhancement methods achieve an increased CNR for all the images. The average CNR increase derived by direct projection is 50.8%, compared with 22.3% of the background subtraction approach.

6.2.3 Improvement on detection accuracy of phantom inserts

We further evaluate the feasibility of using OOI-enhanced images to extract tumor motion from projection images based on the framework presented in chapter 3. In this section, the segmentation framework is used to evaluate the detection accuracy on OOI-enhanced images.

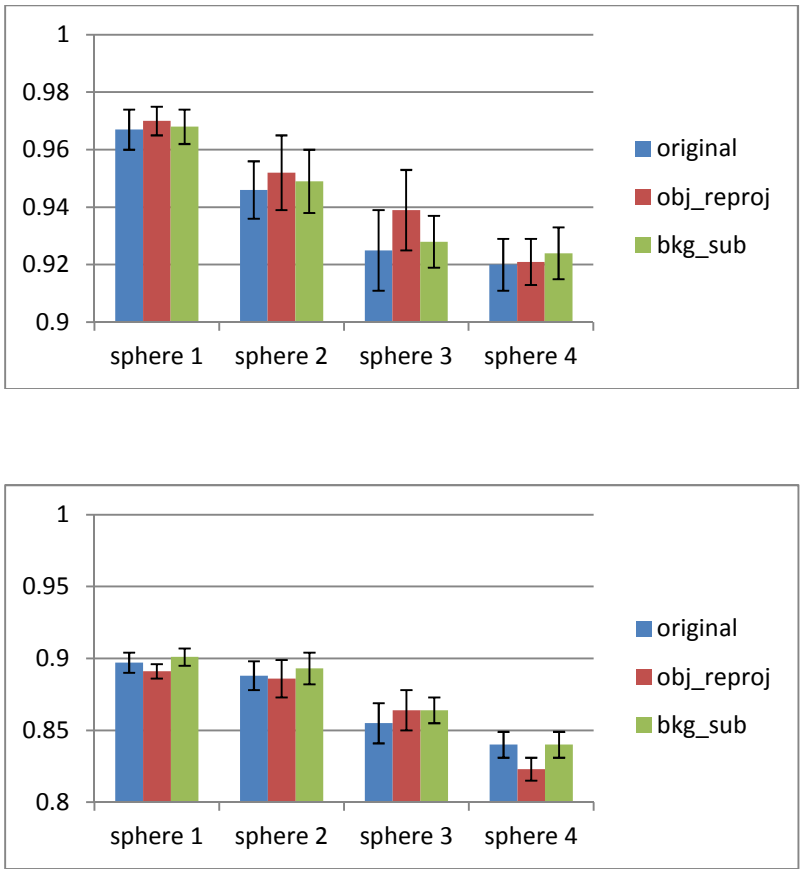

Figure 6-8: Average and standard deviation of dice coefficient of four largest spherical inserts: Top: static scan; Bottom: scan with predefined motion.

Similar to the study described in chapter 3, dice coefficient and the object centroid error is also used to quantify the improvement on detection accuracy. For both metrics, the detected contour of the spherical inserts is compared with the ground truth, which is computed as the projection from the predefined size and 3D motion trajectory. Figure 6-8 shows the dice coefficient of the four largest spherical inserts of the phantom. Generally, the dice coefficient decreases as the size decreases, since the fluctuation on the boundary brings larger variance for smaller size. The overall improvement of the direct projection approach is 0.6% and -0.5% for static scan and motion scan, respectively. The background subtraction approach achieves 2.9% and 0.5%.

Figure 6-9: shows the centorid difference between the detected contour of the spherical inserts and the projected ground truth. The direct OOI projection method reduces the error tremendously in static scan, but not for motion scan, where the overall improvement is 65.2% (static) and -4.1% (motion). The background subtraction approach reduces the error slightly in almost every case, which achieves 1.8% and 4.5%. It should be noted that for motion scan, the graph search framework actually divides the motion of the phantom into several discretized phases. This is a major factor that leads to larger error in the motion scan. The improvement made by OOI-enhancement technique, on the other hand, is primarily related to the error that caused by the interference of overlapping objects. Statistically this improvement can be observed in the experimental result, e.g. the slight improvement of background subtraction approach in nearly all the cases.

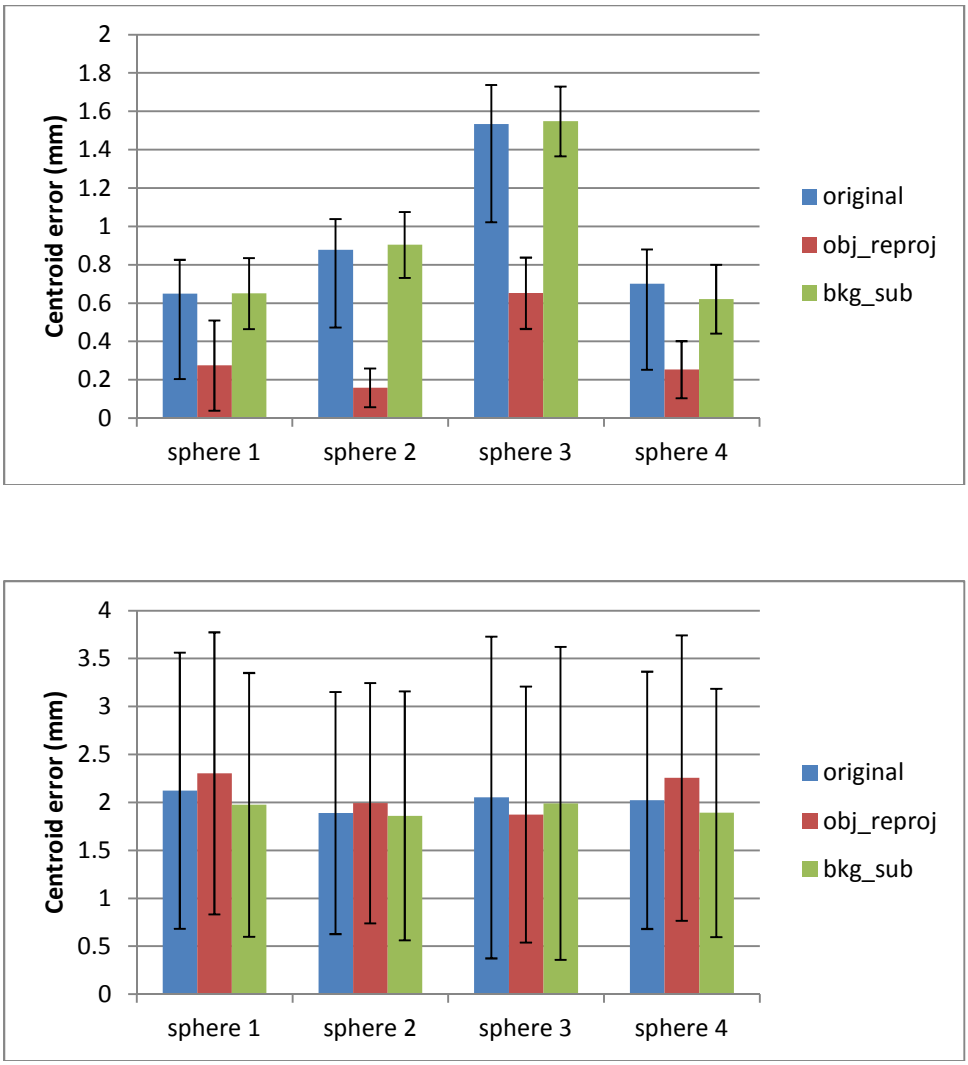

Figure 6-9: Average and standard deviation of centroid error of four largest spherical inserts: Top: static scan; Bottom: motion scan.

6.2.4 Improvement on IHDA detection accuracy

In the original image of Figure 6-4, there are two visible boundaries of the diaphragm, which are two separate hemi-diaphragms that locate at the bottom of the left and the right lung, respectively. In chapter 2, we have shown that in the case when the contra-lateral hemi-diaphragm (CLHD) locates close to the desired IHDA, the gradient-

based DHT approach may sometimes consider the CLHD as the detected diaphragm boundary. In some cases the CLHD even makes manual identification of IHDA error-prone. The overlapping of CLHD occurs mainly near the rotation angle of ±90°, when the two lungs locate in the same direction of the projecting rays. Both OOI-projection and background subtraction provide promising solutions to avoid the influence of CLHD, since the boundaries of CLHD in those 2D projection images could be eliminated, or reduced to some degree.

To evaluate the improvement of IHDA detection accuracy using the proposed method, we quantified the IHDA detection error based on original images, OOI projected images and background-subtracted images, respectively. The detected IHDA based on DHT is compared with manually identified IHDA by a clinical expert. The error is measured as the difference in 3D superior-inferior (SI) direction, where the IHDA position in 2D projection space can be converted to 3D room coordinate based on interpolated ray tracing method (Siochi, 2009).

Figure 6-10 shows the IHDA detection accuracy in 11 MVCBCT scans from 6 patients. Scan *f1* is not included CNR quantification because the tumor is attached to the diaphragm for this patient, which makes CNR value irregular from other images. Generally, when the detection is successful in the overlapping cases, there is nearly no improvement by applying OOI-enhanced techniques. The direct OOI-projection approach may even reduce the detection accuracy slightly, since the continuous motion of IHDA is further descritized into 8 phases during the RC reconstruction. However, when DHT is misled to CLHD in some projection images, OOI-enhanced approach is able to correct the problems successfully (image d1, for example, note that the large standard deviation represents the misdetection in those frames). Since the manual identification of IHDA is performed in the original image, the boundary may not look exactly the same in the OOI enhanced images. It is not surprised that the error increases slightly in the good cases, such as b1 and c1.

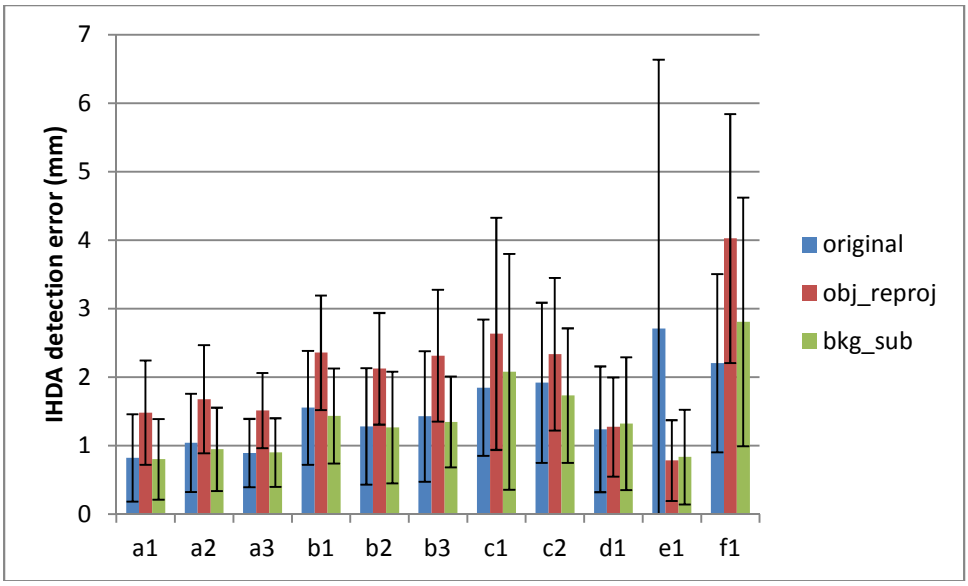

Figure 6-10: Average and standard deviation of IHDA detection error along 3D SI direction from 11 MVCBCT scans of 6 patients.

Figure 6-11 and Figure 6-12 further shows examples of using OOI-enhanced techniques to correct CLHD interference during IHDA detection. Figure 6-12 compares the Hough accumulation array computed from the unprocessed image and background-subtracted image. It can be seen that the accumulation value of the CLHD appears stronger than the desired IHDA in the first few frames, which misleads the DHT detection to the wrong trajectory. In the accumulation array computed from background-subtracted images, the desired IHDA trajectory becomes relatively larger than the CLHD. One frame example in the image space is shown in Figure 6-11**,** where the misled diaphragm position is successfully corrected.

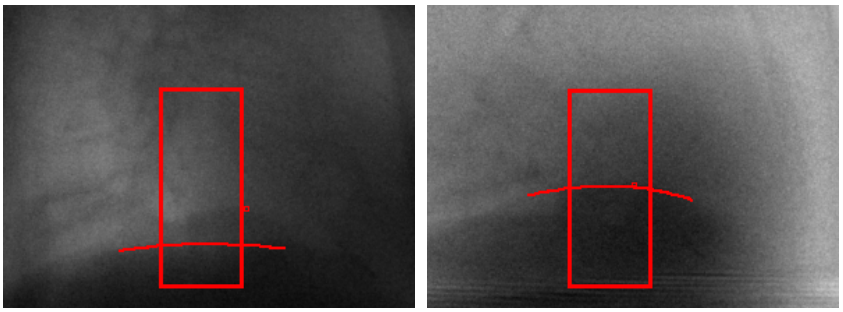

Figure 6-11: Successful correction to the interference of CLHD in IHDA detection: left: DHT detection is misled to the CLHD on the unprocessed image; right: DHT works correct on the background subtracted image. Red rectangle: region of interest of IHDA; Red contour: detected diaphragm contour; Red point: manually identified position, used as ground truth.

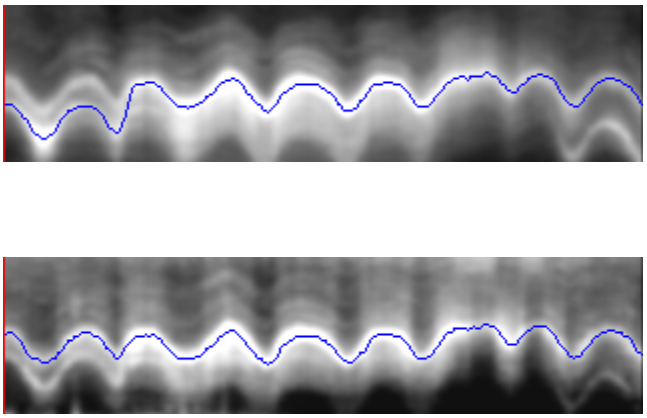

Figure 6-12: 2D visualization of the Hough accumulation space through entire image sequence. Top: Hough space computed from unprocessed images; Bottom: Hough space computed from background subtracted images. Note how the accumulation value of the superior diaphragm becomes relatively larger and influence the detected trajectory (blue contour).

6.2.5 Discussions of the enhancement framework

From the previous experimental results, we can conclude that the direct OOI projection approach is very suitable to enhance static OOI. It replaces the original scattering–contaminated image with a new noise-free one. It achieves significant improvement on both CNR and detection accuracy, since the interference of overlapping objects is eliminated. However, when motion exists, the fidelity of the projected OOI becomes a question. Though CNR improvement is still significant, the detection accuracy is reduced generally. It is primarily due to the fact that the respiratory gating process groups the motion into several bins. Residual motion exists for each phase bin and the reconstructed image is actually averaged from all the projection images that are selected in the window (Dietrich, Jetter, Tücking, Nill, & Oelfke, 2006; T. Li et al., 2006; Sonke, Zijp, Remeijer, & van Herk, 2005). For the projection images that are selected to the same phase bin, the direct projection approach generates new images for those rotation angles from the same 3D volume, in spite of the residual motion that previously existed. The projected object is thus deviated from the original location as a result of the gating. Though one could apply motion compensated reconstruction method using a prior model of displacement fields (T. Li et al., 2007; Rit et al., 2009; Schafer et al., 2006), the accuracy of the motion model to represent the real motion remains a question.

Though the background subtraction method also requires a gating process for motion scan, the original OOI boundary information is not lost after projection and subtraction. Thus the boundary location can be retained. This can explain why the detection accuracy does not deteriorate by using this approach. However, the background subtraction method also retains the scattered radiation in the subtracted image, which can explain why the CNR is relatively low compared to the direct projection approach.

Moreover, the background subtraction approach cannot eliminate the background information completely. This is primarily due to three reasons: scattered radiation,

reconstruction error and the aforementioned grouping during the gating process. For scattered radiation, the cone beam CT based on 2D planar detector generally receives more photons than traditional multi-detector CT based on fan-beam geometry (Orth et al., 2008). For both MV photons used in MVCBCT and KV photons used in diagnostic imaging, Compton scattering comprises the majority of interactions for normal tissues in the body. The noise level due to Compton scattering is lower for MV photons, since the scattering is mostly in the forward direction. For KV photons, the scattering is more isotropic (Morin et al., 2006).

The reconstruction error could be due to several factors. Firstly, the lack of projection images causes view-aliasing artifact in the reconstructed volume. In our implementation, the 200 projection images are divided into 8 respiratory bins, generating only 25 images for each phase bin on the average. Through SART algorithm has the advantage of dealing with view-aliasing artifacts than methods based on filtered-backprojection, it can never eliminate the image degradation due to missing projections. These artifacts will bring further inaccuracies in the projected OOI or background images. Though one could reduce the number of respiratory bins to have more projection images, the larger gating window brings larger object detection inaccuracies.

Secondly, it is quite usual that the patient anatomy extends beyond the field of view (FOV) of the cone beam system. On one hand, it induces the truncation artifact, which makes the tissues near the truncated region has much higher attenuations. On the other hand, the tissue locates outside the FOV of the volumetric image is not accounted during the forward projection, which makes P_b' less than what it should be. Though extrapolation techniques exist (Ohnesorge, Flohr, Schwarz, Heiken, & Bae, 2000), it cannot eliminate the inaccuracies brought by truncation. Based on our experience, the performance of OOI enhancement performs much better for images without truncation (such as phantom images). But truncation occurs for most of the NSCLC patients imaged by MVCBCT.

Generally, the enhancement framework based on SART introduced in this chapter is a feasibility study, where we only concern about the improvement based on detection accuracy or image quality of the projection images. Running time is not considered here, since current implementation of SART algorithm based on CPU platform takes about 7~8 hours for RC reconstruction. To make the proposed feasible for clinical application, the running time is not longer a trivial issue. Current implementation for fast SART computation requires GPU platform, which could be considered as future work.

One may think it is a contradiction that the IHDA motion signal is used as input for phase sorting, while at the same time the IHDA detection accuracy is used to evaluate the performance of the enhancement. It should be noted that the input IHDA is manually corrected, which guarantees that the phase sorting is reasonable. For a practical clinical implementation that uses the enhanced images for IHDA detection, the phase sorting has to be based on strain gauge signals. However, the feasibility study introduced in this chapter tries to focus on the performance of the enhancement framework only. It tries to avoid any error that is not related to the enhancement framework itself,since phase sorting based on the relative phase signal of the strain gauge may induce larger errors than that of IHDA. Moreover, the evaluation is also tested on CNR and tumor segmentation accuracy, which is not in a “chicken and egg” relationship with the enhancement procedure.

To sum up, this chapter introduces two OOI enhancement methods based on cone beam CT geometry are presented, which are based the forward projection of OOI and background region, respectively. The direct projection approach achieves significant enhancement performance for static OOI, in terms of both CNR and boundary detection accuracy. The background subtraction approach improves the CNR and the detection accuracy for both static and moving OOI slightly but robustly. The experiments based on both phantom and patient images show the clinical feasibility to improve the detection

accuracy of tumor and diaphragm in projection images. The proposed OOI enhancement technique can be generalized on any cone beam CT systems.

CHAPTER 7

CONCLUSION AND FUTURE DIRECTIONS

Respiratory motion management is an important research area of adaptive radiation therapy to lung cancer. Accurate gating and conformal shape of the radiation beam during the treatment delivery is a challenging problem. In this thesis, several new approaches based on MVCBCT localization system are proposed to improve the accuracy of treatment delivery.

In chapter 2, a semi-automatic and a fully-automatic framework are developed for IHDA detection in MVCBCT projection images. The IHDA motion along SI direction can be used as respiratory signal, which is an internal surrogate to tumor motion. Currently, the semi-automatic framework has been implemented in a clinical software "UIHC 4D Verification" and under clinical trial. The method requires manual initialization of IHDA position in 4 frames. The semi-automatic framework is tested on 19 patient images, deriving an error of 1.341±0.640*mm* and 1.228±0.220*mm* for DHT and PDF tracking, respectively. This error is clinically acceptable, based on the fact that 3*mm* excess of tumor motion only leads to a 1% change of tumor control probability. Besides, both methods are within the clinical time requirement. The software was also implemented with manual adjustment function, which allows the clinicians to rectify the problematic detection. In the future, we will test the software under longer term to validate the robustness of this method.

The fully automatic approach replaces the manual initialization step with automatic ROI localization. The ROI of IHDA in the projection image is detected by estimating the IHDA range of motion in the reconstructed 3D volume. The estimation is based on template fitting and morphological analysis. The automatic framework is tested on 35 scans, deriving an accuracy of 2.933±4.189 *mm* and 1.714±1.544 *mm* for the DHT

and tracking based approach, respectively. The automatic approach is somewhat less accurate than the semi-automatic approach, due to problematic ROI initialization in some images. However, the automatic ROI determination followed by PDF-based tracking algorithm still fulfills the clinical requirement on the IHDA detection accuracy. Moreover, the system could be still relied on manual rectification on a few frames of projection images, which could be processed within the time requirement. Currently, the fully automatic framework is implemented in a separate platform called "MING-DICOM". In the future, it can be implemented as part of the clinical software "UIHC 4D Verification", which could be used for guidance for the ROI initialization. The clinicians can verify the ROI initialization manually. For problematic initialization, they can rectify it based on the semi-automatic framework. Since the automatic initialization is good for most cases, it could further save the running time of the procedure.

In chapter 3, a novel method for direct tumor segmentation from projection images is developed. It is based on the idea of converting the quasi-periodic motion segmentation into an optimal interrelated surface detection problem. The problem can be further be solved by a graph search framework. A 4D directed graph is constructed based on an initialized mesh model, where the cost value for this graph is computed from the point location of a silhouette outline of projected tumor mesh in 2D projection images. The method was first evaluated on four different sized phantom inserts (all above 1.9 *cm* in diameter) with a predefined motion of 3.0 *cm* to mimic the imaging of lung tumors. A dice coefficient of 0.87±0.03 and a centroid error of 1.94±1.31*mm* were obtained. Results based on 12 MVCBCT scans from 3 patients obtained 0.91±0.03 for dice coefficient and 1.83±1.31*mm* for centroid error, compared with a difference between two sets of independent manual contours of 0.89±0.03 and 1.61±1.19*mm*, respectively. These results show the clinical feasibility of the proposed approach. The limit of tumor segmentation validation is that there is no ground truth of patient data available. We can only compare with the detected tumor contour with the manual contour. However, the fidelity of the

manual contour remains a question, since the inter-variance between two users is comparable to the variance between detected contour and the average of manual contour. Though 4D CT generally provides volumetric image series with clear tumor boundary, the tumor shape and size would be different from MVCBCT scan. On the other hand, the imaging phantom provides ground truth data about "tumor" shape, size and position during the motion. The phantom used in this study has a spherical shape, which is relatively easy for 2D-to-3D shape recovery. In the future, we will design and make a new imaging phantom with more complicated "tumor" shape. The method will be further validated on those complicated shapes.

In chapter 4, the accuracy of using RC MVCBCT to measure DTMR value is quantified. The DTMR measurement accuracy is further divided into study of quantification of volume and motion measurement. Again, patient images face the same problem of lacking ground truth data of tumor volume and motion amplitude. However, a clear exponential trend of tumor shrinkage is observable by manually contouring and measuring the tumor size through the course of radiotherapy. For phantom images, an average error of 10% is achieved for phantom inserts with a diameter of 1.9cm. For tumor motion quantification, an average error of 5% is achieved for phantom inserts with any size, given the nominal motion amplitude of 30*mm*. We further draw our conclusion that there is more than 99% probability of using the proposed IHDA detection approach and RC reconstruction technique to derive the average tumor localization accuracy within 3.0*mm*. This conclusion is based on the normal distribution assumption of the measured variables, including IHDA detection accuracy from 2D projection images, IHDA and tumor motion between FE phase and FI phase in 3D volume.

On the other hand, the imaging phantom only provides a lower bound of error for motion and volume quantification, since the phantom inserts are spherical in shape. We believe that irregular shape under the same condition would bring larger errors due to the segmentation inaccuracies. Similar to the previous segmentation framework, we will

design and make a new phantom with more complicated inserts to mimic tumor shape. The volume and motion measurement accuracy will be evaluated again on this new platform.

In Chapter 5, a new motion compensated reconstruction approach is developed, which utilizes the prior motion model that was extracted from 2D projection images. The new method is compared with two traditional MC reconstruction approaches, which utilize prior motion model from 4D CT and RC MVCBCT, respectively. The RC reconstruction approach alone is also included for comparison. The proposed method is tested on 12 patient MVCBCT scans, where for each scan, 3D volume in FE and FI phase is reconstructed respectively. We measure the CNR value, the tumor volume and IHDA motion amplitude between FE and FI phase. The ground truth of tumor volume is based on 4D CT, where we try to minimize the inter-fractional change of tumor size by selecting MVCBCT scan that is close to the corresponding 4D CT scan. The ground truth of IHDA motion amplitude is based on the 3D motion extracted from 2D projection images. Overall, the new method has best performance in terms of image quality and fidelity to the real motion. For IHDA motion amplitude quantification, the new approach reaches a comparable accuracy as RC reconstruction technique, where both methods are better than MC based on 4D CT and RC MVCBCT. For tumor volume measurement, the new approach derives a similar accuracy with MC based on 4D CT, where both methods are better than two RC-MVCBCT related approaches. For image quality measurement based on CNR, the new approach has the highest CNR in both diaphragm and tumor area.

Currently the MC reconstruction method is based on the segmentation framework introduced in chapter 3. The projection images are sorted into 20 bins, where 10 bins are used for exhale phase and the other 10 bins are used for inhale phase. The resolution of the lung mesh used for segmentation is set to make the running time of reconstruction process within an acceptable time. Generally, increasing the number of bins would improve the temporal resolution of the motion model, which may potentially increase the

motion amplitude accuracy or even the tumor volume accuracy as well. However, increasing the number of bins would reduce the number of projections for each bin, which may make the 2D-to-3D shape recovery not robust. On the other hand, increasing the mesh resolution would further increase the reconstruction accuracy. Future studies can be based on varying the number of bins and the mesh resolution of the reconstruction process. The new MC reconstruction approach could also be validated on imaging phantom, where the lung mesh model can be created from the basswood frame. We believe that the motion and volume quantification accuracy derived by the new MC method would be better than the RC reconstruction technique.

In Chapter 6, a novel approach of enhancing MVCBCT projection images is introduced. The enhancement framework starts by reconstructing a 3D volume from 2D projection images based on simultaneous algebraic reconstruction technique (SART). Then the region of the organ of interest (OOI) is manually identified. Two strategies are used for image enhancement: the first approach sets the attenuation coefficient of non-OOI region to zero and projects the volume that contains only the OOI region onto projection images; while the second approach sets the attenuation coefficient of OOI region to zero and projects the non-OOI region onto 2D to create a background image. The final enhanced image is derived by subtracting the background image from the original projection. The enhanced images generated by the two strategies were evaluated on two MVCBCT scans of phantom images and 10 patient images based on different metrics. The direct projection approach achieves an improvement of 365%, 238% and 60.9% on average of contrast to noise ratio (CNR) on static phantom insert, moving phantom insert and patient diaphragm respectively. For the background subtraction approach, CNR improvement is 21.4%, 13.8% and 19.6%. In terms of detection accuracy, the direct projection approach achieves improvement of 65.2% on the quantification of the centroid of the static phantom insert, but fails to improve the detection accuracy in the motion scan (with 13.6% drop in diaphragm apex quantification accuracy). The

background subtraction approach improves the detection accuracy slightly (on the order of 0.5% and 4% for dice coefficient and centroid error, respectively) for nearly all the cases and achieves 13.1% improvement for diaphragm apex quantification.

In all, the direct projection approach is able to derive enhanced OOI image with both improved CNR and detection accuracy for static object. For motion scan, the background subtraction approach is more suitable than the direct projection approach in terms of improving the detection accuracy. But the CNR improvement is not as large as the direct projection approach due to the scattered radiation. Future work may involve implementation of the algorithm to GPU platform and validation on more patient images.

REFERENCES

Andersen, A., & Kak, A. (1984). Simultaneous algebraic reconstruction technique (SART): a superior implementation of the ART algorithm. *Ultrasonic Imaging, 6*(1), 81-94.

Arai, T., Kuroishi, T., Saito, Y., Kurita, Y., Naruke, T., & Kaneko, M. (1994). Tumor doubling time and prognosis in lung cancer patients: evaluation from chest films and clinical follow-up study. *Japanese Journal of Clinical Oncology*, *24*(4), 199-204.

Armato III, S. G., Giger, M. L., & MacMahon, H. (2001). Automated detection of lung nodules in CT scans: preliminary results. *Medical Physics, 28*, 1552.

Ballard, D. H. (1981). Generalizing the Hough transform to detect arbitrary shapes. *Pattern Recognition, 13*(2), 111-122.

Baxter, B. S., & Sorenson, J. A. (1981). Factors affecting the measurement of size and CT number in computed tomography. *Investigative Radiology, 16*(4), 337.

Belderbos, J. S. A., Heemsbergen, W. D., De Jaeger, K., Baas, P., & Lebesque, J. V. (2006). Final results of a Phase I/II dose escalation trial in non-small-cell lung cancer using three-dimensional conformal radiotherapy. *International Journal of Radiation Oncology* Biology* Physics, 66*(1), 126-134.

Berbeco, R. I., Mostafavi, H., Sharp, G. C., & Jiang, S. B. (2005). Towards fluoroscopic respiratory gating for lung tumours without radiopaque markers. *Physics in Medicine and Biology, 50*, 4481.

Berbeco, R. I., Nishioka, S., Shirato, H., Chen, G. T. Y., & Jiang, S. B. (2005). Residual motion of lung tumours in gated radiotherapy with external respiratory surrogates. *Physics in Medicine and Biology, 50*, 3655.

Berbeco, R. I., Nishioka, S., Shirato, H., & Jiang, S. B. (2006). Residual motion of lung tumors in end-of-inhale respiratory gated radiotherapy based on external surrogates. *Medical Physics, 33*, 4149-4156.

Bookstein, F. L. (1989). Principal warps: Thin-plate splines and the decomposition of deformations. *Pattern Analysis and Machine Intelligence, IEEE Transactions on, 11*(6), 567-585.

Boykov, Y., & Funka-Lea, G. (2006). Graph cuts and efficient nd image segmentation. *International Journal of Computer Vision, 70*(2), 109-131.

Boykov, Y., & Kolmogorov, V. (2004). An experimental comparison of min-cut/max-flow algorithms for energy minimization in vision. *Pattern Analysis and Machine Intelligence, IEEE Transactions on, 26*(9), 1124-1137.

Boykov, Y., Veksler, O., & Zabih, R. (2001). Fast approximate energy minimization via graph cuts. *IEEE Transactions on Pattern Analysis and Machine Intelligence, ,* 1222-1239.

Boyle, P., & Leven, B. (Eds.). (2009). *World cancer report 2008* (1st edition ed.) World health organization.

Brody, W. R. (1982). Digital subtraction angiography. *Nuclear Science, IEEE Transactions on, 29*(3), 1176-1180.

Brown, M. S., McNitt-Gray, M. F., Goldin, J. G., Suh, R. D., Sayre, J. W., & Aberle, D. R. (2001). Patient-specific models for lung nodule detection and surveillance in CT images. *Medical Imaging, IEEE Transactions on, 20*(12), 1242-1250.

Brown, M. S., McNitt-Gray, M. F., Mankovich, N. J., Goldin, J. G., Hiller, J., Wilson, L. S., & Aberie, D. (1997). Method for segmenting chest CT image data using an anatomical model: preliminary results. *Medical Imaging, IEEE Transactions on, 16*(6), 828-839.

Bruce, E. N. (1996). Temporal variations in the pattern of breathing. *Journal of Applied Physiology, 80*(4), 1079.

Cao, K., Du, K., Ding, K., Reinhardt, J. M., & Christensen, G. E. (2010). Regularized nonrigid registration of lung CT images by preserving tissue volume and vesselnes measure. *Medical Image Analysis for the Clinic-A Grand Challenge, ,* 43-54.

Cervino, L. I., Chao, A. K. Y., Sandhu, A., & Jiang, S. B. (2009). The diaphragm as an anatomic surrogate for lung tumor motion. *Physics in Medicine and Biology, 54*, 3529-3541.

Chen, M., Zheng, Y., Mueller, K., Rohkohl, C., Lauritsch, G., Boese, J., . . . Comaniciu, D. (2011). Automatic extraction of 3D dynamic left ventricle model from 2D rotational angiocardiogram. *Medical Image Computing and Computer-Assisted Intervention–MICCAI 2011, ,* 471-478.

Cherkassky, B. V., & Goldberg, A. V. (1997). On Implementing the Push—Relabel Method for the Maximum Flow Problem. *Algorithmica, 19*(4), 390-410.

Condurache, A., Aach, T., Eck, K., Bredno, J., & Stehle, T. (2005). Fast and robust diaphragm detection and tracking in cardiac x-ray projection images. *Proc. SPIE, , 5747* 1766-1775.

Cormen, T. H. (2001). *Introduction to algorithms* The MIT press.

Cui, Y., Dy, J. G., Sharp, G. C., Alexander, B., & Jiang, S. B. (2007). Multiple template-based fluoroscopic tracking of lung tumor mass without implanted fiducial markers. *Physics in Medicine and Biology, 52*, 6229.

Cusma, J. T., Bell, M. R., Wondrow, M. A., Taubel, J. P., & Holmes, D. R. (1999). Real-time measurement of radiation exposure to patients during diagnostic coronary angiography and percutaneous interventional procedures. *Journal of the American College of Cardiology, 33*(2), 427-435.

Dehmeshki, J., Amin, H., Valdivieso, M., & Ye, X. (2008). Segmentation of pulmonary nodules in thoracic CT scans: a region growing approach. *Medical Imaging, IEEE Transactions on, 27*(4), 467-480.

DeLaney, T. F. (2009). Prescribing, Recording, and Reporting Proton-Beam Therapy. *Radiation Research, 171*(6), 776-776.

Diciotti, S., Picozzi, G., Falchini, M., Mascalchi, M., Villari, N., & Valli, G. (2008). 3-D segmentation algorithm of small lung nodules in spiral CT images. *Information Technology in Biomedicine, IEEE Transactions on, 12*(1), 7-19.

Dietrich, L., Jetter, S., Tücking, T., Nill, S., & Oelfke, U. (2006). Linac-integrated 4D cone beam CT: first experimental results. *Physics in Medicine and Biology, 51*, 2939-2952.

D'Souza, W. D., Nazareth, D. P., Zhang, B., Deyoung, C., Suntharalingam, M., Kwok, Y., . . . Regine, W. F. (2007). The use of gated and 4D CT imaging in planning for stereotactic body radiation therapy. *Medical Dosimetry, 32*(2), 92-101.

Evans, P., Gildersleve, J., Rawlings, C., & Swindell, W. (1993). The implementation of patient position correction using a megavoltage imaging device on a linear accelerator. *British Journal of Radiology, 66*(789), 833.

Faddegon, B. A., Aubin, M., Bani-Hashemi, A., Gangadharan, B., Gottschalk, A. R., Morin, O., . . . Yom, S. S. (2010). Comparison of patient megavoltage cone beam CT images acquired with an unflattened beam from a carbon target and a flattened treatment beam. *Medical Physics, 37*, 1737.

Faddegon, B. A., Wu, V., Pouliot, J., Gangadharan, B., & Bani-Hashemi, A. (2008). Low dose megavoltage cone beam computed tomography with an unflattened 4 MV beam from a carbon target. *Medical Physics, 35*, 5777.

Fahrig, R., Fox, A., Lownie, S., & Holdsworth, D. (1997). Use of a C-arm system to generate true three-dimensional computed rotational angiograms: preliminary in vitro and in vivo results. *American Journal of Neuroradiology, 18*(8), 1507-1514.

Feldkamp, L., Davis, L., & Kress, J. (1984). Practical cone-beam algorithm. *JOSA A, 1*(6), 612-619.

Fischler, M. A., & Bolles, R. C. (1981). Random sample consensus: a paradigm for model fitting with applications to image analysis and automated cartography. *Communications of the ACM, 24*(6), 381-395.

Flynn, R. T., Hartmann, J., Bani-Hashemi, A., Nixon, E., Alfredo, R., Siochi, R. A. C., . . . Bayouth, J. E. (2009). Dosimetric characterization and application of an imaging beam line with a carbon electron target for megavoltage cone beam computed tomography. *Medical Physics, 36*, 2181.

Ford, E., Chang, J., Mueller, K., Sidhu, K., Todor, D., Mageras, G., . . . Amols, H. (2002). Cone-beam CT with megavoltage beams and an amorphous silicon electronic portal imaging device: Potential for verification of radiotherapy of lung cancer. *Medical Physics, 29*, 2913.

Fujita, T., Chandrasekhar, R., Singh, B., & Finucane, K. E. (2006). Semi-automatic tracking of the diaphragm contour in X-ray image sequences: Preliminary results. *Digital Image Computing: Techniques and Applications, 2005. DICTA'05. Proceedings 2005*, 48.

Galigekere, R. R., Wiesent, K., & Holdsworth, D. W. (2003). Cone-beam reprojection using projection-matrices. *Medical Imaging, IEEE Transactions on, 22*(10), 1202-1214.

Garvin, M. K., Abràmoff, M. D., Kardon, R., Russell, S. R., Wu, X., & Sonka, M. (2008). Intraretinal layer segmentation of macular optical coherence tomography images using optimal 3-D graph search. *Medical Imaging, IEEE Transactions on, 27*(10), 1495-1505.

George, R., Keall, P., Kini, V., Vedam, S., Ramakrishnan, V., & Mohan, R. (2005). Is the diaphragm motion probability density function normally distributed? *Medical Physics, 32*, 396-404.

Goo, J. M., Tongdee, T., Tongdee, R., Yeo, K., Hildebolt, C. F., & Bae, K. T. (2005). Volumetric Measurement of Synthetic Lung Nodules with Multi–Detector Row CT: Effect of Various Image Reconstruction Parameters and Segmentation Thresholds on Measurement Accuracy1. *Radiology, 235*(3), 850.

Gordon, R., Bender, R., & Herman, G. T. (1970). Algebraic Reconstruction Techniques (ART) for three-dimensional electron microscopy and X-ray photography* 1. *Journal of Theoretical Biology, 29*(3), 471-481.

Hills, M., Pridmore, T., & Mills, S. (2003). Object tracking through a Hough space. *Visual Information Engineering, 2003. VIE 2003. International Conference on*, 53-56.

Hoisak, J. D. P., Sixel, K. E., Tirona, R., Cheung, P. C. F., & Pignol, J. P. (2004). Correlation of lung tumor motion with external surrogate indicators of respiration. *International Journal of Radiation Oncology* Biology* Physics, 60*(4), 1298-1306.

Iwasawa, T., Yoshiike, Y., Saito, K., Kagei, S., Gotoh, T., & Matsubara, S. (2000). Paradoxical motion of the hemidiaphragm in patients with emphysema. *Journal of Thoracic Imaging, 15*(3), 191.

Jemal, A., Siegel, R., Xu, J., & Ward, E. (2010). Cancer statistics, 2010. *CA: A Cancer Journal for Clinicians, 60*(5), 277.

Joseph, P. M., & Spital, R. D. (1982). The effects of scatter in x-ray computed tomography. *Medical Physics, 9*, 464.

Kabus, S., Müller, F., Wiemker, R., & Fischer, B. (2008). Robust lung nodule growth measurement by combining registration and segmentation. *The First International Workshop on Pulmonary Image Analysis*, 15–23.

Keall, P. J., Mageras, G. S., Balter, J. M., Emery, R. S., Forster, K. M., Jiang, S. B., . . . Murray, B. R. (2006). The management of respiratory motion in radiation oncology report of AAPM Task Group 76. *Medical Physics, 33*, 3874-3900.

Kiryati, N., Eldar, Y., & Bruckstein, A. M. (1991). A probabilistic Hough transform. *Pattern Recognition, 24*(4), 303-316.

Lappas, P., Carter, J. N., & Damper, R. I. (2002). Robust evidence-based object tracking. *Pattern Recognition Letters, 23*(1-3), 253-260.

Lappas, P., Damper, R. I., & Carter, J. N. (2006). Object tracking by energy maximization. *Soft Computing-A Fusion of Foundations, Methodologies and Applications, 10*(1), 20-26.

Leng, S., Tang, J., Zambelli, J., Nett, B., Tolakanahalli, R., & Chen, G. H. (2008). High temporal resolution and streak-free four-dimensional cone-beam computed tomography. *Physics in Medicine and Biology, 53*, 5653-5673.

Lewitt, R. M. (1990). Multidimensional digital image representations using generalized Kaiser-Bessel window functions. *JOSA A, 7*(10), 1834-1846.

Li, K., Wu, X., Chen, D. Z., & Sonka, M. (2006). Optimal surface segmentation in volumetric images-a graph-theoretic approach. *IEEE Transactions on Pattern Analysis and Machine Intelligence*, , 119-134.

Li, T., Koong, A., & Xing, L. (2007). Enhanced 4D cone-beam CT with inter-phase motion model. *Medical Physics, 34*, 3688-3695.

Li, T., Schreibmann, E., Yang, Y., & Xing, L. (2006). Motion correction for improved target localization with on-board cone-beam computed tomography. *Physics in Medicine and Biology, 51*, 253.

Li, T., & Xing, L. (2007). Optimizing 4D cone-beam CT acquisition protocol for external beam radiotherapy. *International Journal of Radiation Oncology* Biology* Physics, 67*(4), 1211-1219.

Li, T., Xing, L., Munro, P., McGuinness, C., Chao, M., Yang, Y., . . . Koong, A. (2006). Four-dimensional cone-beam computed tomography using an on-board imager. *Medical Physics, 33*, 3825-3833.

Lin, T., Cervino, L. I., Tang, X., Vasconcelos, N., & Jiang, S. B. (2009). Fluoroscopic tumor tracking for image-guided lung cancer radiotherapy. *Physics in Medicine and Biology, 54*, 981.

Lotjonen, J., Magnin, I. E., Nenonen, J., & Katila, T. (1999). Reconstruction of 3-D geometry using 2-D profiles and a geometric prior model. *Medical Imaging, IEEE Transactions on, 18*(10), 992-1002.

Lotjonen, J., Reissman, P. J., Magnin, I. E., & Katila, T. (1999). Model extraction from magnetic resonance volume data using the deformable pyramid. *Medical Image Analysis, 3*(4), 387-406.

Lujan, A. E., Larsen, E. W., Balter, J. M., & Ten Haken, R. K. (1999). A method for incorporating organ motion due to breathing into 3D dose calculations. *Medical Physics, 26*, 715.

Ma, C. M. C., & Paskalev, K. (2006). In-room CT techniques for image-guided radiation therapy. *Medical Dosimetry, 31*(1), 30-39.

Mackie, T. R., Kapatoes, J., Ruchala, K., Lu, W., Wu, C., Olivera, G., . . . Jeraj, R. (2003). Image guidance for precise conformal radiotherapy. *International Journal of Radiation Oncology* Biology* Physics, 56*(1), 89-105.

Magnusson, A. (1987). Object size determination at computed tomography. *Upsala Journal of Medical Sciences, 92*(3), 277-286.

Mills, S., Pridmore, T., & Hills, M. (2003). Tracking in a Hough space with the extended Kalman filter. *The British Machine Vision Conference, Norwich*, 173-182.

Morin, O., Chen, J., Aubin, M., Gillis, A., Aubry, J. F., Bose, S., . . . Pouliot, J. (2007). Dose calculation using megavoltage cone-beam CT. *International Journal of Radiation Oncology* Biology* Physics, 67*(4), 1201-1210.

Morin, O., Gillis, A., Chen, J., Aubin, M., Bucci, M. K., Roach III, M., & Pouliot, J. (2006). Megavoltage cone-beam CT: system description and clinical applications. *Medical Dosimetry, 31*(1), 51-61.

Moriyama, M., Sato, Y., Naito, H., Hanayama, M., Ueguchi, T., Harada, T., . . . Tamura, S. (2002). Reconstruction of time-varying 3-D left-ventricular shape from multiview X-ray cineangiocardiograms. *Medical Imaging, IEEE Transactions on, 21*(7), 773-785.

Mueller, K., Yagel, R., & Wheller, J. J. (1999a). Anti-aliased three-dimensional cone-beam reconstruction of low-contrast objects with algebraic methods. *Medical Imaging, IEEE Transactions on, 18*(6), 519-537.

Mueller, K., Yagel, R., & Wheller, J. J. (1999b). Fast implementations of algebraic methods for three-dimensional reconstruction from cone-beam data. *Medical Imaging, IEEE Transactions on, 18*(6), 538-548.

Nash, J. M., Carter, J. N., & Nixon, M. S. (1997). Dynamic feature extraction via the velocity Hough transform. *Pattern Recognition Letters, 18*(10), 1035-1047.

Neicu, T., Berbeco, R., Wolfgang, J., & Jiang, S. B. (2006). Synchronized moving aperture radiation therapy (SMART): improvement of breathing pattern reproducibility using respiratory coaching. *Physics in Medicine and Biology, 51*, 617.

Oelfke, U., Tücking, T., Nill, S., Seeber, A., Hesse, B., Huber, P., & Thilmann, C. (2006). Linac-integrated kV-cone beam CT: technical features and first applications. *Medical Dosimetry, 31*(1)

Ohnesorge, B., Flohr, T., Schwarz, K., Heiken, J., & Bae, K. (2000). Efficient correction for CT image artifacts caused by objects extending outside the scan field of view. *Medical Physics, 27*, 39.

Opfer, R., & Wiemker, R. (2007). A new general tumor segmentation framework based on radial basis function energy minimization with a validation study on LIDC lung nodules. *Proceedings of SPIE, , 6512* 651217.

Orth, R. C., Wallace, M. J., & Kuo, M. D. (2008). C-arm cone-beam CT: general principles and technical considerations for use in interventional radiology. *Journal of Vascular and Interventional Radiology, 19*(6), 814-820.

Otsu, N. (1975). A threshold selection method from gray-level histograms. *Automatica, 11*, 285-296.

Pouliot, J., Bani-Hashemi, A., Chen, J., Svatos, M., Ghelmansarai, F., Mitschke, M., . . . Bucci, K. (2005). Low-dose megavoltage cone-beam CT for radiation therapy. *International Journal of Radiation Oncology* Biology* Physics, 61*(2), 552-560.

Reitz, B., Gayou, O., Parda, D. S., & Miften, M. (2008). Monitoring tumor motion with on-line mega-voltage cone-beam computed tomography imaging in a cine mode. *Physics in Medicine and Biology, 53*, 823-836.

Rit, S., Wolthaus, J. W. H., van Herk, M., & Sonke, J. J. (2009). On-the-fly motion-compensated cone-beam CT using an a priori model of the respiratory motion. *Medical Physics, 36*, 2283-2296.

Ross, C. S., Hussey, D. H., Pennington, E. C., Stanford, W., & Fred Doornbos, J. (1990). Analysis of movement of intrathoracic neoplasms using ultrafast computerized tomography. *International Journal of Radiation Oncology* Biology* Physics, 18*(3), 671-677.

Sato, Y., Moriyama, M., Hanayama, M., Naito, H., & Tamura, S. (1997). Acquiring 3d models of non-rigid moving objects from time and viewpoint varying image sequences: A step toward left ventricle recovery. *Pattern Analysis and Machine Intelligence, IEEE Transactions on, 19*(3), 253-259.

Schafer, D., Borgert, J., Rasche, V., & Grass, M. (2006). Motion-compensated and gated cone beam filtered back-projection for 3-D rotational X-ray angiography. *Medical Imaging, IEEE Transactions on, 25*(7), 898-906.

Shimizu, S., Shirato, H., Ogura, S., Akita-Dosaka, H., Kitamura, K., Nishioka, T., . . . Miyasaka, K. (2001). Detection of lung tumor movement in real-time tumor-tracking radiotherapy. *International Journal of Radiation Oncology* Biology* Physics, 51*(2), 304-310.

Sidky, E. Y., & Pan, X. (2008). Image reconstruction in circular cone-beam computed tomography by constrained, total-variation minimization. *Physics in Medicine and Biology, 53*, 4777-4807.

Siochi, R. A. C. (2007). *Verification of 4D Radiation Therapy*

Siochi, R. A. C. (2009). Deriving motion from megavoltage localization cone beam computed tomography scans. *Physics in Medicine and Biology, 54*, 4195-4212.

Siochi, R. A. C., Kim, Y., & Bhatia, S. (2008). Tumor control probability (TCP) reduction in phase gated RT treatments of non-small cell lung cancer (NSCLC) tumors with motion in excess of planned motion. *International Journal of Radiation Oncology* Biology* Physics, 72*(1), S49-S49.

Song, Q., Wu, X., Liu, Y., Sonka, M., & Garvin, M. (2010). Simultaneous searching of globally optimal interacting surfaces with shape priors. *Computer Vision and Pattern Recognition (CVPR), 2010 IEEE Conference on*, 2879-2886.

Sonke, J. J., Zijp, L., Remeijer, P., & van Herk, M. (2005). Respiratory correlated cone beam CT. *Medical Physics, 32*, 1176-1186.

Sorensen, S. P., Chow, P. E., Kriminski, S., Medin, P. M., & Solberg, T. D. (2006). Image-guided radiotherapy using a mobile kilovoltage x-ray device. *Medical Dosimetry, 31*(1), 40-50.

Stephens, R. (1991). Probabilistic approach to the Hough transform. *Image and Vision Computing, 9*(1), 66-71.

Stevens, C. W., Munden, R. F., Forster, K. M., Kelly, J. F., Liao, Z., Starkschall, G., . . . Komaki, R. (2001). Respiratory-driven lung tumor motion is independent of tumor size, tumor location, and pulmonary function. *International Journal of Radiation Oncology* Biology* Physics, 51*(1), 62-68.

Stutzel, J., Oelfke, U., & Nill, S. (2008). A quantitative image quality comparison of four different image guided radiotherapy devices. *Radiotherapy and Oncology, 86*(1), 20-24.

Topal, U., & Ediz, B. (2003). Transthoracic needle biopsy: factors effecting risk of pneumothorax. *European Journal of Radiology, 48*(3), 263-267.

Underberg, R., Lagerwaard, F. J., Cuijpers, J. P., Slotman, B. J., van Sornsen de Koste, JR, & Senan, S. (2004). Four-dimensional CT scans for treatment planning in stereotactic radiotherapy for stage I lung cancer. *Int J Radiat Oncol Biol Phys, 60*(4), 1283-1290.

Vedam, S., Keall, P., Kini, V., & Mohan, R. (2001). Determining parameters for respiration-gated radiotherapy. *Medical Physics, 28*, 2139.

Veisterä, H., & Lötjönen, J. (2001). Reconstructing 3D boundary element heart models from 2D biplane fluoroscopy. *Functional Imaging and Modeling of the Heart, ,* 17-23.

Vora, S. A., Daly, B. D. T., Blaszkowsky, L., McGrath, J. J., Bankoff, M., Supran, S., & Dipetrillo, T. A. (2000). High dose radiation therapy and chemotherapy as induction treatment for stage III nonsmall cell lung carcinoma. *Cancer, 89*(9), 1946-1952.

Wang, Q., Song, E., Jin, R., Han, P., Wang, X., Zhou, Y., & Zeng, J. (2009). Segmentation of Lung Nodules in Computed Tomography Images Using Dynamic Programming and Multidirection Fusion Techniques1. *Academic Radiology, 16*(6), 678-688.

Wu, H., Zhao, Q., Berbeco, R. I., Nishioka, S., Shirato, H., & Jiang, S. B. (2008). Gating based on internal/external signals with dynamic correlation updates. *Physics in Medicine and Biology, 53*, 7137.

Wu, X., & Chen, D. (2002). Optimal net surface problems with applications. *Automata, Languages and Programming, ,* 775-775.

Xu, L., Oja, E., & Kultanen, P. (1990). A new curve detection method: randomized Hough transform (RHT). *Pattern Recognition Letters, 11*(5), 331-338.

Xu, Q., Hamilton, R. J., Schowengerdt, R. A., Alexander, B., & Jiang, S. B. (2008). Lung tumor tracking in fluoroscopic video based on optical flow. *Medical Physics, 35*, 5351.

Xu, Q., Hamilton, R. J., Schowengerdt, R. A., & Jiang, S. B. (2007). A deformable lung tumor tracking method in fluoroscopic video using active shape models: a feasibility study. *Physics in Medicine and Biology, 52*, 5277.

Yin, Y., Zhang, X., & Sonka, M. (2008). Optimal multi-object multi-surface graph search segmentation: Full-joint cartilage delineation in 3d. *MIUA*, 104–108.

Zhang, J., Yi, B., Lasio, G., Suntharalingam, M., & Yu, C. (2009). Tomographic image via background subtraction using an x-ray projection image and a priori computed tomography. *Medical Physics, 36*, 4433.

Zhang, Q., Hu, Y. C., Liu, F., Goodman, K., Rosenzweig, K. E., & Mageras, G. S. (2010). Correction of motion artifacts in cone-beam CT using a patient-specific respiratory motion model. *Medical Physics, 37*, 2901-2909.